Faculty of Physics and Astronomy

University of Heidelberg

Diploma thesis
in Physics
submitted by
René Faßbender
born in Diez
2003

Commissioning of the near IR camera OMEGA2000 and development of a pipeline reduction system

This diploma thesis has been carried out by
René Faßbender
at the
Max-Planck-Institute for Astronomy
under the supervision of
Priv.-Doz. Dr. Hermann-Josef Röser

Commissioning of the near IR camera OMEGA2000 and development of a pipeline reduction system

Abstract   OMEGA2000 is the new near-infrared wide field camera for the 3.5 m-telescope at the Calar Alto observatory. The instrument is based on a 2048×2048 pixel HgCdTe detector array that yields an unprecedented field of view for IR observations of $15\!\!.'4 \times 15\!\!.'4$. In this thesis, the newly developed observing and reduction software package for OMEGA2000 is presented and selected commissioning results are discussed. The automatic observing utilities handle the telescope focusing, flatfielding, and the science data acquisition. The pipeline reduction system will allow on-site real-time data processing without user interaction. The automated reduction includes detector calibration, sky subtraction, and the superposition of single frames to a final deep image. The evaluated commissioning data yield that the detector tilt is close to its optimum, the focus needs readjustment after each filter change, and that the use of an undersized warm baffle improves the signal-to-noise ratio in the K-band by about 8%. The analysis of pipeline reduced data indicates sky level variations of up to 10% within timescales of five minutes and about 3% across the detector field of view. The limiting magnitude of a 90-minute exposure in the H-band is shown to be about 20.3 mag.

Inbetriebnahme der Nah-IR-Kamera OMEGA2000 und Entwicklung eines automatischen Datenreduktionssystems

Zusammenfassung   OMEGA2000 ist die neue Nahinfrarot-Weitfeld-Kamera für das 3.5 m-Teleskop am Calar Alto Observatorium. Das Instrument basiert auf einem 2048×2048 Pixel HgCdTe Detektor-Array, das ein für Infrarot-Beobachtungen bisher beispielloses Bildfeld von $15\!\!.'4 \times 15\!\!.'4$ liefert. In dieser Arbeit wird das neu entwickelte Beobachtungs- und Reduktions-Software-Paket für OMEGA2000 vorgestellt und ausgewählte Ergebnisse der Inbetriebnahmephase werden präsentiert. Die automatischen Beobachtungsprogramme übernehmen die Teleskop-Fokussierung, die Aufnahme von Flatfields sowie die wissenschaftlichen Beobachtungen. Das Pipeline-Reduktions-System wird künftig eine Echtzeit-Datenverarbeitung vor Ort ohne Benutzereingriffe ermöglichen. Die automatisierte Reduktion beinhaltet die Detektorkalibrierung, die Himmelssubtraktion und die Überlagerung von Einzelbildern zu einer einzigen tiefen Aufnahme. Die ausgewerteten Daten aus der Testphase lassen auf eine nahezu optimale Detektorlage schließen und verlangen eine Fokuskorrektur nach jedem Filterwechsel. Des Weiteren wird durch die Platzierung eines kleinen warmen Baffles eine Verbesserung des Signal-Rausch-Verhältnisses im K-Band von ca. 8% gefunden. Die Untersuchung von Pipeline-reduzierten Daten lässt auf Himmelsvariationen von bis zu 10% auf einer Zeitskala von fünf Minuten und von ca. 3% über das Detektorbildfeld schließen. Die gemessene Grenzhelligkeit einer 90-Minuten Aufnahme im H-band beträgt 20.3 Magnituden.

"The Universe is full of magical things, patiently waiting for our wits to grow sharper"

(Eden Philpotts)

Contents

List of Figures

List of Tables

Chapter 1

Introduction

Over the last few decades, infrared (IR) astronomy has matured to a vast field in the extraterrestrial sciences with ever growing importance to astronomical research. The opening of the wavelength range beyond the optical region has permitted observations — and thus advanced our understanding — of otherwise inaccessible or undetectable astronomical systems. Only infrared astronomy allows detailed studies of cold objects, such as brown dwarfs or — in the near future — even planets, and dust obscured systems such as star forming regions. Moreover, the infrared spectral region opens the door to studying the very young and distant universe. Due to the cosmological redshift, interesting rest frame wavelength regions from the earliest cosmic epochs are shifted outside the optical region and can only be detected in the infrared.

Important scientific advances have been achieved with infrared space observatories such as the cornerstone missions IRAS in 1983 and ISO in 1995. For the scientific reasons above, the Next Generation Space Telescope (NGST), renamed the James-Webb-Space-Telescope and planned to be launched in 2010, will also be an IR observatory.

Although the effects of Earth's atmosphere impose a serious challenge for astronomical infrared studies, ground based IR observations have significantly progressed since the pioneering work with single "pixel" bolometers in the 1960s. Most advances have been driven by the availability of increasingly larger IR detector arrays. With well designed IR instruments and the proper observing and reduction strategies, the superior light collecting area of large ground based telescopes can be used to conduct high quality infrared observations within the atmospheric transmission windows. Because of the exponentially growing thermal background contribution towards higher wavelengths, the near-infrared (NIR) region between 1–2.5 μm is of special interest for ground based instruments.

The Calar Alto observatory in Southern Spain has been on the forefront of near-infrared instrumentation for more than a decade. The NIR-cameras currently in service at the 3.5 m-telescope are OMEGA-CASS, mounted to the Cassegrain focus and used for high spatial resolution studies, and the prime-focus instrument OMEGA-Prime. Both instruments incorporate a $1k \times 1k$-pixel detector array.

With the development of $2k \times 2k$-pixel detectors over the last few years, NIR-instruments with an even larger sky coverage become feasible. One of the first new generation instru-

1

ments is the near-infrared wide field camera OMEGA2000 that was designed and built at the MPIA. The $2k \times 2k$-pixel detector allows an unprecedented field of view of $15\!\!'.4 \times 15\!\!'.4$. OMEGA2000 will soon replace OMEGA-Prime as the prime-focus imaging instrument at the 3.5 m-telescope. OMEGA2000 had first light in January 2003 and is currently in the commissioning phase.

The principal tasks of commissioning are instrument performance tests of all components under real observing conditions at the telescope. During the designated commissioning observing time, the data quality can be assessed and remaining problems identified and solved. A critical and time consuming issue is the performance optimization of the new generation detector since no prior experience exists for this model. Once a final operational instrument setup is achieved, calibration frames have to be produced that allow an accurate correction of all intrinsic detector imperfections. The commissioning phase is completed with the *scientific verification* that is used for a final assessment of the full instrument capability for astronomical research. After this last test, the new instrument is fully operational and can be used by the astronomical community to address unsolved scientific questions.

The main objective of this diploma thesis was the development and testing of observing utilities and a data reduction pipeline system for OMEGA2000 during the instrument commissioning phase. The first set of routines will automatically operate OMEGA2000 and the telescope for standard observational procedures such as focusing, taking flatfields, and handling the actual scientific data acquisition. The new pipeline reduction software will allow immediate real-time data processing at the telescope. This novel feature of the OMEGA2000 package will permit an accurate on-site data assessment which can be used to adjust and optimize the current observing strategy.

Besides the above mentioned software developments, this thesis includes the analysis of selected OMEGA2000 commissioning data sets. As part of the instrument optimization process, the detector tilt and the focus offsets for the different filters are determined. In addition, the effect of the undersized movable warm baffle — a special OMEGA2000 feature — is investigated. Furthermore, two sets of pipeline reduced images are used to measure the temporal and spatial sky background variations and to determine the limiting magnitude of a deep exposure.

The thesis is structured in the following way: Chapter 2 briefly discusses the aspects of IR observations and provides a short review on infrared detectors and the main background sources of ground based observations. The facts summarized in Chap. 2 set the stage for a better understanding of the methods and results of the subsequent sections. OMEGA2000 with its main components is presented in Chap. 3. Chapter 4 discusses the observing utilities and the instrument related commissioning results. The structure and performance of the new data reduction pipeline is covered in Chap. 5. As an application of the pipeline for reducing data sets, the sky background variations as well as the limiting magnitude of a deep exposure are investigated in Chap. 6. The closing Chap. 7 gives an outlook on open tasks and future OMEGA2000 projects.

Chapter 2

Aspects of IR-Astronomy

This chapter will briefly review the physical and technological fundamentals needed for a better understanding of the applications, methods, problems, and observing/reduction strategies of ground based infrared astronomy. The next sections will focus on the following three important questions with special emphasis on wide field near-infrared observations as will be conducted with OMEGA2000.

- What are the scientific advantages of infrared astronomy?

- How do infrared detector arrays work in principle?

- What are the challenges in ground based infrared observations?

2.1 Scientific Prospects

The infrared spectral region covers the wavelengths from $1\,\mu$m to about $350\,\mu$m. This regime can be further subdivided into near-infrared (1-5 μm), mid-infrared (5-25 μm), and far-infrared (25-350 μm), which accounts for the different detector types and observing techniques required (Joyce, 1992).

The infrared spectral region is adjacent to the optical window (0.3–1 μm) at longer wavelengths. Infrared observations are thus sensitive to physical processes with lower intrinsic energies and to flux that has been redshifted outside the optical region. The most important applications and advantages of IR astronomy arise from the following three fundamental physical facts : "cold" objects emit thermal radiation mostly in the infrared, the cosmological redshift, and the high dust extinction in the visible.

2.1.1 Thermal emission of cold objects

According to Wien's displacement rule, the wavelength λ_{max} at the maximum of the Planck function $B_\lambda(T)$ for the emitted radiation of a blackbody at temperature T is given by

$$\lambda_{max} \cdot T = 2.90 \cdot 10^{-3} \mathrm{m} \cdot \mathrm{K} = 2.90 \cdot 10^{3} \mu\mathrm{m} \cdot \mathrm{K}\,. \tag{2.1}$$

From this equation it is evident that all objects with a temperature $T \leq 2900\,\mathrm{K}$ emit most of their thermal radiation at wavelengths $\lambda_{max} \geq 1\,\mu\mathrm{m}$, *i.e.*, in the infrared. This implies that astrophysical objects with temperatures $10\,\mathrm{K} \lesssim T \lesssim 2900\,\mathrm{K}$ have intrinsic spectra that can be best observed with infrared instruments.

Table 2.1 lists some typical astrophysical objects that emit radiation mainly in the infrared.

Object	Temperature [K]	λ_{max} [μm]	Reference
M-Stars	2800	1.0	Lindner (1989)
Protostars	200-3600	0.8-14.5	Unsöld (1991)
Brown Dwarfs	500-2500	1.2-5.8	Homepage MPIA[1]
Extrasolar Planets	200-1400	2.1-14.5	Bodenheimer & Lin (2002)
Interstellar Matter:			
Cold Neutral Medium	80	36	Unsöld (1991)
Dust	20	145	Cox (2000)

Table 2.1: Infrared emitting objects with their typical temperatures and wavelengths of maximum emission.

2.1.2   Cosmological redshift

The redshift z of spectral lines is defined as

$$z = \frac{\Delta\lambda}{\lambda_0} = \frac{\lambda_{obs} - \lambda_0}{\lambda_0} \; , \tag{2.2}$$

where λ_0 is the rest frame wavelength and λ_{obs} the measured wavelength of a spectral line. Equation 2.2 yields an observed wavelength λ_{obs} of spectral features for distant extragalactic objects with cosmological redshift z of

$$\lambda_{obs} = (z + 1) \cdot \lambda_0 \, . \tag{2.3}$$

Prominent and important spectral features for distant objects are the hydrogen lines H_α, Ly_α, and the Lyman- and Balmer-series limits. Table 2.2 lists the rest frame wavelengths λ_0 of these features and the redshift z_{IR} at which the observed wavelength λ_{obs} is $1\,\mu\mathrm{m}$ and thus entering the IR regime.

High redshift objects such as primordial galaxies and QSOs have almost no observed flux in the wavelength region below the Ly_α-emission line. This feature — called the *Ly_α forest* — originates from a large number of absorbtion lines due to gas clouds along the line of sight (Cox, 2000). Figure 2.1 illustrates the spectrum of a quasar at redshift $z = 6.28$. This quasar is close to the optical detection limit since the Ly_α forest absorbtion has almost completely eliminated the flux below $875\,\mathrm{nm}$.

---

[1]`http://www.mpia-hd.mpg.de/STARS/index.html`

Spectral Hydrogen Features	λ_0 [nm]	z_{IR}
H_α	656.3	0.52
Balmer Break	364.6	1.7
Ly_α	121.6	7.2
Lyman Break	91.2	10

Table 2.2: Spectral features of hydrogen. λ_0 is the rest frame wavelength of the spectral feature, z_{IR} is the redshift where $\lambda_{obs} = 1\,\mu$m.

If objects with $z \gtrsim 6.5$ are to be detected, it is inevitable to observe in the near-infrared. This goal will be pursued by the *Dark Age Z Lyman-Alpha Explorer*[2] (DAZLE), which is a NIR narrow-band imaging instrument under development for the VLT.

As will be shown in Sect. 7.2.2, galaxy surveys with photometric redshift determinations have to use near-infrared observations to accurately classify galaxies with $z \gtrsim 1$.

2.1.3 Dust extinction

The extinction of interstellar dust is a strong function of wavelength. In the near-infrared, the opacity of dust is proportional to $\lambda^{-1.9}$ due to dust particles with size much less than $1\,\mu$m (Beckwith, 1994). This implies that an extinction of 10 visual magnitudes corresponds to about an extinction of

Figure 2.1: Spectrum of a quasar with z=6.28. The relative flux is plotted against the wavelength. The Ly_α emission line is observed at 885 nm. The continuum below 875 nm is almost completely absorbed by the intergalactic medium. Source: Press release of the MPG, PRI SP3 (2001).

only 1 magnitude at $2.2\,\mu$m. The wavelength dependance of the extinction coefficient has the effect that regions with a lot of dust are totally opaque in the optical and can only be studied in the infrared.

An important example of these conditions are star forming regions, where the strong extinction of dust clouds prevent optical observations. Taking into account that protostars emit most of their luminosity in the IR (see Tab. 2.1), star formation and young stars can
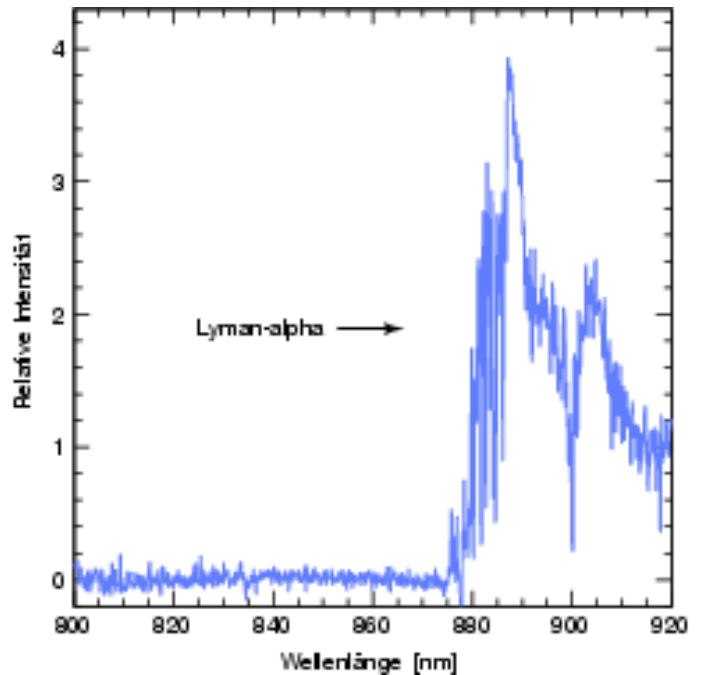
---

[2]More details can be found under: `http://www.ast.cam.ac.uk/optics/dazle/`

Instrument	Telescope	Year	Array Size [pixels]	Field Size [arcmin^2]
MAGIC[4]	CA 3.5m	1993	256×256	3.5
OMEGA-PRIME[5]	CA 3.5m	1995	1024×1024	47
ISAAC[6]	VLT	1999	1024×1024	6
OMEGA2000[7]	CA 3.5m	2003	2048×2048	237
WIRCam[8]	CFHT	2004	$4 \times 2048 \times 2048$	400
VISTA IR Camera[9]	VISTA	> 2006	$16 \times 2048 \times 2048$	936

Table 2.3: Selected past, present, and future NIR instruments. All instruments are based on HgCdTe detectors with a sensitivity range of 1–2.5 μm.

only be studied in detail with infrared instruments.

An extreme example of dust opacity is the galactic center, which shows an extinction of 15 magnitudes in the visible but only of 1.5 magnitudes in the IR (Beckwith, 1994).

2.2   Detectors

The heart of every astronomical instrument is its light sensitive detector. The advent of sensitive charge-coupled devices (CCDs) around 1980 revolutionized optical observations. However, CCDs are only sensitive in the spectral region from roughly 300 nm to 1 μm, which — at the long wavelength cut — is due to the 1.1 eV bandgap of the semiconductor material silicon[3]. The fundamental physical detection limit of pure silicon also defines the threshold from optical to infrared astronomy, since for the latter the well understood and highly advanced silicon semiconductor technology can not be used.

This section shortly summarizes the historical developments and state-of-the-art technology of near-infrared arrays.

2.2.1   Historical development

Most advances in infrared astronomy have been driven by increased detector capability (Beckwith, 1994). In Fig. 2.2, the rapid detector size development is illustrated. Over the last 30 years, the infrared array size (dashed line) has evolved from a single pixel detector to more than 4 million pixels today. The largest presently available near-infrared detector is the 2048×2048-pixel HAWAII-2 array discussed in Chap. 3.

Table 2.3 lists some selected NIR instruments of the past 10 years and the near future. OMEGA2000's field of view (FoV) is almost 70 times larger than the FoV of the best instruments 10 years ago. By using mosaics of several arrays, the sky coverage of the best instruments will continue to increase in the coming years.

---

[3]The minimum photon energy to overcome the silicon bandgap of $E_g = 1.11$ eV (Stöcker 1998) corresponds to a maximum photon wavelength of $\lambda_{max} = 1.1\,\mu$m.
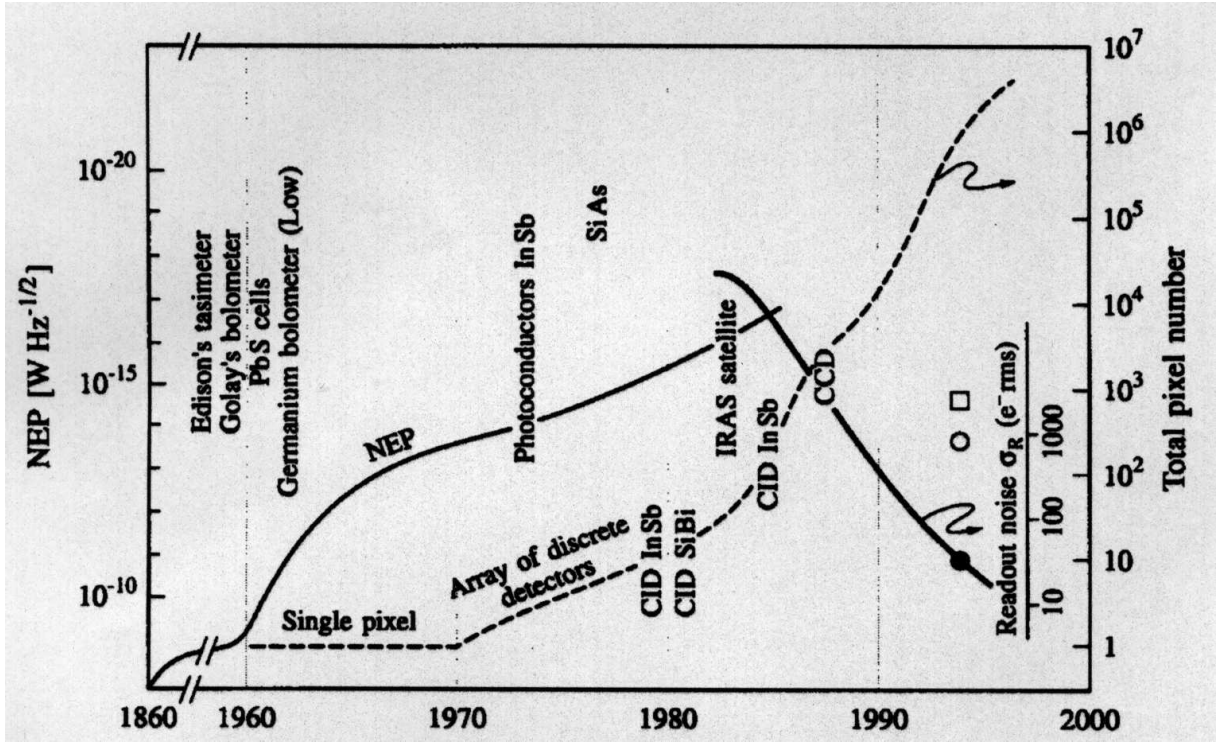
Figure 2.2: Historical array size development. The infrared array size (dashed line) has increased from a single pixel in 1970 to more than 4 million pixels today. At the same time, the readout noise (separate scale on the right) has drastically decreased. From Léna *et al.* (1998).

2.2.2 Detector technology

The photon detection process can be subdivided into three parts involving different hardware components that will be briefly discussed (Léna *et al.*, 1998):

1. actual photon detection by creation of photo charges

2. storage of charges at the site of detection

3. amplification and readout

The pre-requisite for the construction of an array detector are appropriate infrared sensitive materials with a sufficiently small bandgap. Commonly used materials for astronomical applications are (Joyce, 1992):

---

[4]For more information see: `http://www.mpia-hd.mpg.de`

[5]For more information see: `http://www.mpia-hd.mpg.de`

[6]For more information see: `http://www.eso.org/instruments/isaac/`

[7]For more information see: `http://www.mpia-hd.mpg.de`

[8]For more information see: `http://www.cfht.hawaii.edu/News/Projects/WIRCam/New/overview`

[9]For more information see: `http://www.vista.ac.uk/`

- Mercury-cadmium-telluride (HgCdTe) with a bandgap of $E_g = 0.5\,\text{eV}$ corresponding to a cutoff wavelength of $\lambda_c = 2.5\,\mu\text{m}$. HgCdTe is the most commonly used material for the construction of large near-infrared array formats. In fact, the actual energy gap is dependent on the Hg/Cd ratio and can be changed between 0.1-1 eV for different applications.

- Indium-antimonide (InSb) with $E_g = 0.23\,\text{eV}$ and $\lambda_c = 5.4\,\mu\text{m}$ is sensitive out to slightly longer wavelengths.

- Si:As with $E_g = 0.05\,\text{eV}$ and $\lambda_c = 27\,\mu\text{m}$ can be used for mid-infrared observations. By doping silicon with other materials, *e.g.*, gallium (Ga), different cutoff properties can be achieved.

Due to the small energy gap between the valence and conduction bands, thermal excitation can produce many electron-hole-pairs inside the IR sensitive semiconductor material. Since the dark current — the charges produced by pure thermal excitation — has the proportionality $i_{dark} \propto e^{-E_g/kT}$, it is inevitable to operate IR detectors at very low temperatures. Near-infrared detectors require a typical operation temperature of 77 K, whereas devices for longer wavelengths are cooled to a few degrees Kelvin (Joyce, 1992).

Many different IR detector designs have been proposed and tested. In principle, a CCD detector architecture, where a single material absorbs photons, stores the charges, and the signal is read from, would also be possible for narrow-bandgap materials. This effort, however, has long been abandoned due to technological difficulties with the IR detector materials (Hodapp, 2000).

The general design that has prevailed and is used for modern NIR devices is the hybrid array, where the function of radiation detection and the multiplexing of the signal are separated (McLean, 1997). The resulting sandwich structure has the advantage that the signal processing can be handled by a multiplexer based on the highly advanced silicon technology. This silicon multiplexer is electrically connected to the infrared sensor through an indium "bump" for each pixel.

Figure 2.3 illustrates the general hybrid layout of a near-infrared detector array. The left panel shows the cross section of an individual pixel. Going from pixel top to bottom, an infrared transparent substrate serves as footing for the backside illuminated photodiode which has the mentioned indium connection to the silicon multiplexer.

The actual photon detection takes place in the infrared sensitive photodiode with its pn-junction. By applying an initial reverse-bias voltage V to the photodiode, the depletion region of the pn-junction acts like a capacitor C. Incoming infrared photons can generate electron-hole pairs via the internal photoelectric effect in the depletion zone. The pair is immediately separated by the external electric field which results in a discharge of the initial reverse-bias voltage V (Murdin, 2001). In contrast to a CCD where electrons are accumulated, the local "storage" of photo charges in infrared arrays is accomplished by a gradual photon-induced discharge of the capacitor C with initial voltage V. The full well capacity is reached, *i.e.*, the pixel is saturated, when the capacitor is completely discharged.
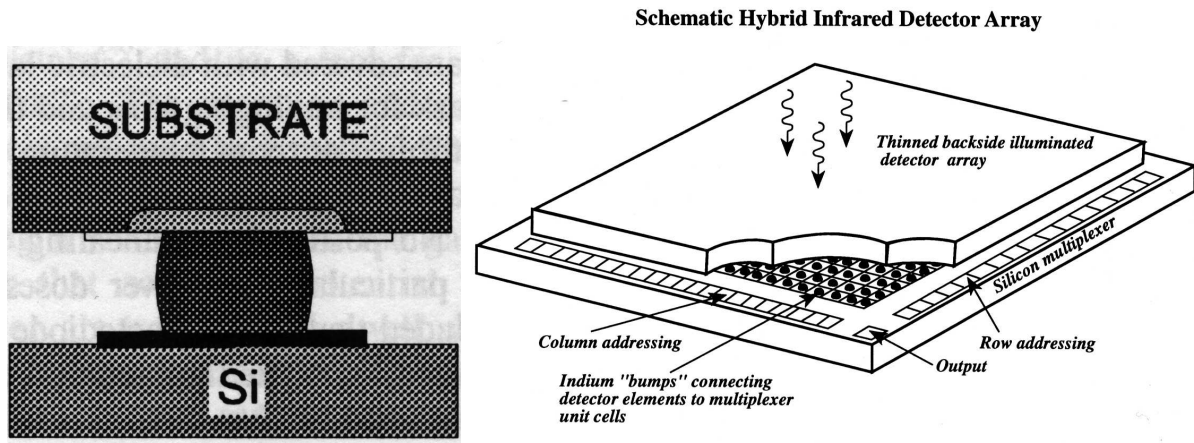
Figure 2.3: Schematic IR detector design. *Left panel:* Cross section of an individual pixel. The infrared sensitive photodiode is electrically connected to the silicon multiplexer through an indium "bump". From Rogalski (1995). *Right panel:* "Sandwich-structure" of the hybrid array. The pixel signals are multiplexed into few output channels from where the voltages are amplified and converted to digital count units. From Beckwith (1994).

The signal is read out by measuring the residual voltage. Since the pixel charge is not moved, non-destructive readout modes are possible, *i.e.*, the signal can be measured without resetting the pixel. When the whole array is read out, the individual measured voltages of the pixels are multiplexed, *i.e.*, many signals are combined into only a few outlet channels. The output line signals are subsequently amplified and converted to digital count units. The right panel of Fig. 2.3 illustrates the "sandwich-structure" of the hybrid array design and the different registers for the multiplexed readout process.

The hybrid design of near-infrared detector arrays offers advantages but also has a few drawbacks. IR arrays are not based on the charge-coupling principle which is an important distinction of CCDs and has practical implications. The advantage is an effective isolation of the pixels from the neighbors, thus preventing "blooming-effects" of saturated pixels. On the other hand, CCD features such as on-chip charge binning or charge-shifting are not possible (Murdin, 2001). Non-destructive pixel readouts are an additional advantage that allow effective multiple-read algorithms which reduce the unwanted electronic noise. Large area arrays are also prone to mechanical stress fractures, since the infrared sensitive material and the silicon based multiplexer usually have different thermal expansion coefficients.

Critical for the performance of hybrid arrays are the properties of the substrate material and the thickness of the infrared-sensitive layer. The thickness has to be optimized to allow full absorption of the incoming infrared radiation and prevent recombination losses of the photon-generated minority carriers (Hodapp, 2000). Non-uniformity in the thickness will result in significant variations of the quantum efficiency.

As was briefly summarized above, the hybrid design for near-infrared detectors has proven to be very successful for the construction of high quality large-size NIR arrays.

2.3   Limitations of Ground Based Observations

The following section takes a closer look at the problems and challenges that ground based infrared astronomy is facing.

In the first part, the effects of Earth's atmosphere are discussed. The atmosphere shows prominent absorption of molecular transition bands as well as line and continuum emission in the infrared. In order to minimize these atmospheric effects, a high altitude observation site with a dry climate is preferable. The remaining atmospheric contributions require appropriate observing strategies and an elaborate data reduction (see Chap. 4–6).

The second challenge is the handling of the thermal background, which is emitted by the instrument, surrounding structures, and the atmosphere. This is a particularly crucial issue for instruments without a cold pupil such as OMEGA2000. The thermal background may be reduced by cooling critical instrument components and placing baffles, as will be discussed in Chap. 3 & 4.

2.3.1   Atmosphere

Molecular transitions

The following summary of molecular IR transitions will point out the principles that give rise to the atmospheric absorption bands and the high density of emission lines.

Broad band absorbtion features and most emission lines in the infrared are caused by rotational and vibrational transitions of molecules. The spectra of molecules can be calculated in the quantum mechanical description using the Born-Oppenheimer-approximation, which separates the Hamiltonian into electronic, vibrational, and rotational energy terms (Vogel and Gerthsen, 1997). Whereas electronic transitions usually occur at photon energies in the optical and ultraviolet region, vibrational transitions are typically located in the infrared. A first order approximation, where the vibrational potential between two nuclei is assumed to be harmonic, yields the following expression for the quantized energy levels:

$$E_{vib} = (n + \frac{1}{2}) \cdot h\nu \ , \tag{2.4}$$

where $n = 1, 2, 3 \ldots$ is the vibrational quantum number and ν the eigenfrequency of the harmonic potential. Superimposed on vibrational transitions are rotational lines with typical energies of $10^{-2} \cdot E_{vib}$. The first order approximation for the rotational energy levels yields:

$$E_{rot} = \frac{J(J+1) \cdot \hbar^2}{2MR_e^2} \ . \tag{2.5}$$

Here, $J = 1, 2, 3 \cdots$ is the rotational quantum number, M the reduced mass of the nuclei, and R_e the equilibrium distance between the nuclei. The energy difference between the levels increases with J:

$$\Delta E_{rot} = \frac{(J+1) \cdot \hbar^2}{2MR_e^2} \ . \tag{2.6}$$

The selection rules for dipole transitions between energy levels are $\Delta\nu = \pm 1$ and $\Delta J = \pm 1$. This implies that the infrared spectrum, *i.e.*, the transitions in between rotational and vibrational levels, consists of bands of many lines due to the large number of allowed rotational transitions for each vibrational energy difference.

Very important for the infrared activity of the atmosphere is the fact that homo-nuclear molecules have no allowed rotational and vibrational dipole transitions due to their vanishing electric dipole moment. As a consequence, the main constituents of the atmosphere, namely N_2 (78%) and O_2 (21%), are inactive in the infrared region (Glass, 1999). The most important infrared active molecules in the atmosphere are (Cox, 2000): H_2O, O_3, CO_2, N_2O, CH_4 in absorption, and OH in emission.
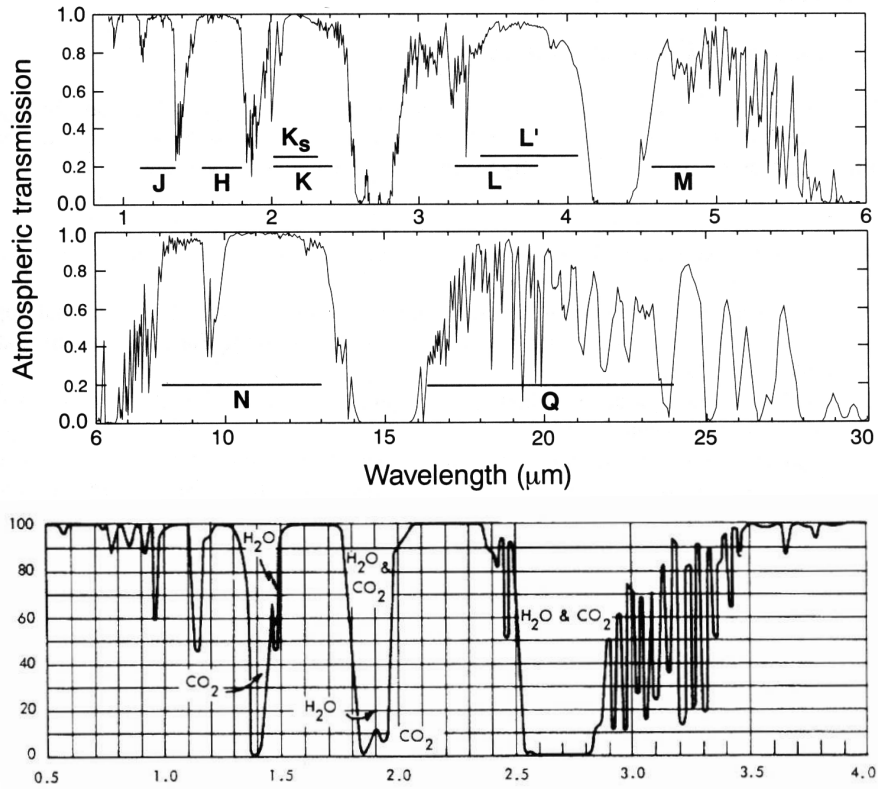

Figure 2.4: *Top panel:* Atmospheric transmission windows in the near- and mid-infrared region with corresponding broad-band filter names. From Cox (2000). *Bottom panel:* Absorbing molecules in the near-infrared. The molecule names are placed at the position of the concerning absorption bands. From Glass (1999)

Absorption

The rotational and vibrational transitions of hetero-nuclear atmospheric molecules described in the last section have the effect that incoming infrared radiation from astronomical objects is almost totally absorbed in many broad bands. Ground based IR observations are only possible in the spectral region between the absorption bands.

Figure 2.4 shows the atmospheric transmission windows in the near- and mid-infrared spectral region. The transmission bands are labelled according to the broad-band spectral filters of the corresponding region. The bottom panel of Fig. 2.4 identifies the molecules causing the absorbtion bands in the near-infrared region.

As shown in Sect. 2.3.2, ground based infrared observations beyond the near-IR bands J, H, and K centered around 1.26, 1.62, and 2.21 μm are extremely difficult.

Emission

Near-infrared observations in the J, H, and K transmission bands are strongly affected by atmospheric emission known as airglow. The airglow is the dominant background source in the near-infrared region and originates from hydroxyl radical (OH^-) emission at an altitude of 85–100 km (Glass, 1999). The radicals are produced during the day in the excitation reaction

$$H + O_3 \longrightarrow OH^* + O_2 \,. \tag{2.7}$$

During the night, the excited OH radicals radiate away their excess energy and produce the so called *Meinel-bands*. OH emission lines appear between 0.61 μm and 2.62 μm and correspond to transitions with $\Delta\nu = 2-5$ (Rousselot *et al.*, 2000). In Fig. 2.5, the OH emission lines for the J, H, and K-band are shown.

Glass (1999) states the averaged integrated line flux in the H-band to be roughly 3×10^4 photons $\cdot$ s^{-1}m^{-2}arcsec$^{-2}\mu$m^{-1}. The airglow background imposes a big challenge for the data reduction process because it exhibits significant temporal variations on timescales $\mathcal{O}(10\,\text{min})$ as well as spatial variations on scales $\mathcal{O}(10\,\text{km})$ (Glass, 1999). These variations in the H-band will be investigated in Sect. 6.1.

2.3.2   Thermal background

In addition to atmospheric line absorption and emission, the thermal background imposes additional limitations on ground based infrared observations.

According to Planck's radiation formula, a blackbody with temperature T emits the following thermal spectrum (Unsöld *et al.*, 1991):

$$B_\lambda(T) = I_\lambda(T) = \frac{2hc^2}{\lambda^5} \cdot \frac{1}{e^{\frac{hc}{k\lambda T}} - 1} \quad \left[\frac{\text{W}}{\text{m}^2\,\text{sr}\,\mu\text{m}}\right] \tag{2.8}$$

Approximate blackbody spectra are emitted by all ambient structure elements such as the primary mirror, the telescope support structure, the dome, the dome floor, and by the
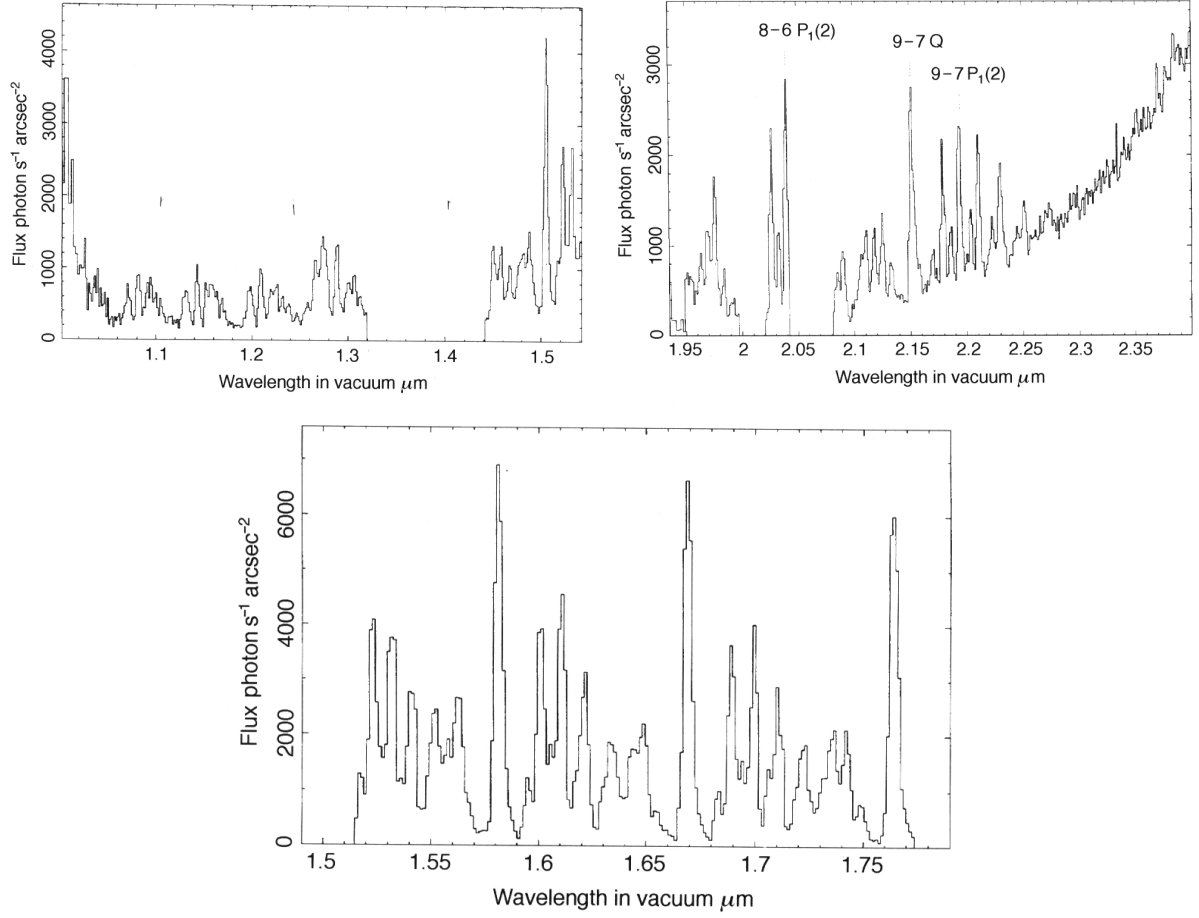
Figure 2.5:   OH emission lines in the J-band (*top left*), *K-band (*top right), and in the H-band (*bottom*). The region around 1.4 μm was not measured. The emission variations in the H-band and the narrow-band filter centered around 1.71 μm are investigated in Sect. 6.1. From Glass (1999).

atmosphere. To minimize the thermal background flux as much as possible, all instrument parts have to be cooled and the optical path baffled (see Chap. 3 & 4).

To illustrate the rapid increase of thermal background flux with increasing wavelength in the IR, Fig. 2.6 displays a blackbody spectrum of a typical ambient temperature of $T = 280\,\mathrm{K} = 7\,°\mathrm{C}$. The near-infrared region is at the short wavelength end of the Planck spectrum of typical ambient temperatures ($\lambda_{max} \approx 10\,\mu\mathrm{m}$), thus the spectral intensity is increasing exponentially (Wien approximation). The thermal background is the dominant flux source for wavelengths $\lambda \gtrsim 2.2\,\mu\mathrm{m}$ making broad-band ground based observations in the K-band time consuming and beyond $2.5\,\mu\mathrm{m}$ extremely difficult.

To get a better quantitative idea of the thermal background flux effects, it is instructive to take a closer look at the relative ratios of background photons in different filters. Assuming perfect filter transmission curves, *i.e.*, a rectangular profile is used, the background photon ratio $R_{filter/J}(T)$ for a given filter — normalized to the background in the J or K filter — is given by:
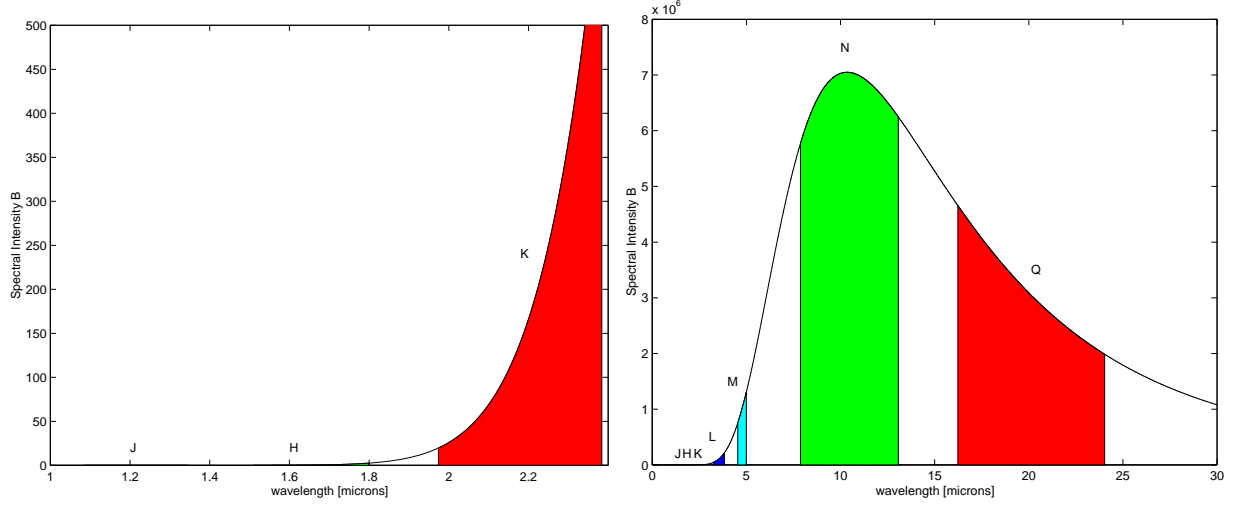
Figure 2.6: Blackbody spectrum of $T = 280$ K. *Left panel:* Spectral intensity for the near-infrared region. The shaded areas depict the integrated flux for the different filters. The filter names are placed at the central transmission wavelength. *Right panel:* Same spectrum for the whole near and mid-infrared region. The maximum of the curve is at $\lambda_{max} = 10.4\,\mu$m.

$$R_{filter/J}(T) = \frac{n_{filter}(T)}{n_J(T)} = \frac{\int\limits_{\lambda_{min}}^{\lambda_{max}} \frac{d\lambda}{E_\lambda}\, B_\lambda(T)}{n_J(T)} = \frac{\int\limits_{\lambda_{min}}^{\lambda_{max}} d\lambda\, \frac{2c}{\lambda^4}\, \frac{1}{e^{\frac{hc}{k\lambda T}} - 1}}{n_J(T)}\ . \tag{2.9}$$

In Tab. 2.4, this ratio is calculated for a number of broad-band filters and a blackbody temperature of $T = 280$ K. Considering that background count rates in the K-band are about as much as a detector can handle — the pixel wells of OMEGA2000 are saturated within a few seconds — the following conclusions can be drawn from Tab. 2.4:

- Compared to K, the thermal background count rates in the H-filter are already suppressed by about a factor of 600.

- For the J-filter and all shorter wavelengths filters, the thermal background count rates are negligible.

- Ground based broad-band observations in the L-band or all longer wavelengths filters are extremely difficult since the thermal background causes detector saturation on timescales $t_{saturation} \approx 10$ ms.

- By using slightly modified K-filters such as K_s and K', the background count rates can be suppressed by 40–60%.

Filter	$\lambda_{central}$ [μm]	$\Delta\lambda_{FWHM}$ [μm]	$\frac{n_{Photons}(filter)}{n_{Photons}(J)}$	$\frac{n_{Photons}(filter)}{n_{Photons}(K)}$
Z	**0.90**	**0.15**	$\mathbf{1.2 \times 10^{-6}}$	$\mathbf{2.2 \times 10^{-13}}$
J	**1.215**	**0.26**	**1**	$\mathbf{1.8 \times 10^{-7}}$
H	**1.654**	**0.29**	$\mathbf{8.7 \times 10^{3}}$	$\mathbf{1.6 \times 10^{-3}}$
K	**2.179**	**0.41**	$\mathbf{5.6 \times 10^{6}}$	**1**
K$_s$	**2.157**	**0.32**	$\mathbf{3.1 \times 10^{6}}$	**0.56**
K$'$	**2.08**	**0.34**	$\mathbf{2.2 \times 10^{6}}$	**0.40**
L	3.55	0.57	6.9×10^{9}	1.3×10^{3}
M	4.77	0.45	6.3×10^{10}	1.1×10^{4}
N	10.47	5.19	1.1×10^{13}	1.9×10^{6}
Q	20.13	7.80	1.4×10^{13}	2.5×10^{6}

Table 2.4:   IR filters and thermal background ratios for $T = 280$K. The filters are specified by their central transmission wavelength $\lambda_{central}$ and the full width at half the transmission maximum $\Delta\lambda_{FWHM}$ (from Cox (2000)). OMEGA2000 filters are indicated by boldface letters. The ratio $n(filter)/n(J)$ of the number of thermal background photons normalized to the J-filter gives a telescope and instrument independent measure of expected background count rate ratios. The last column shows the ratio normalized to the K-filter.

Chapter 3

OMEGA2000 Instrument

3.1 Introduction

The OMEGA2000 project started in 1999 after the announcement that a new generation of $2k\times2k$ near-infrared detectors would be available. With a field of view roughly four times larger than OMEGA-Prime, OMEGA2000 will be the new near-infrared wide-field camera at the prime focus of the Calar Alto Observatory's 3.5m-telescope. With its large $15\rlap{.}'4 \times 15\rlap{.}'4$ field of view combined with excellent optical quality, OMEGA2000 is particularly designed as a survey instrument for near-infrared (NIR) imaging. A single OMEGA2000 pointing covers the sky area corresponding to one quarter of the full moon.

Figure 3.1 shows OMEGA2000 mounted to the frontring of the 3.5m-telescope. Table 3.1 lists general properties of the OMEGA2000 instrument.
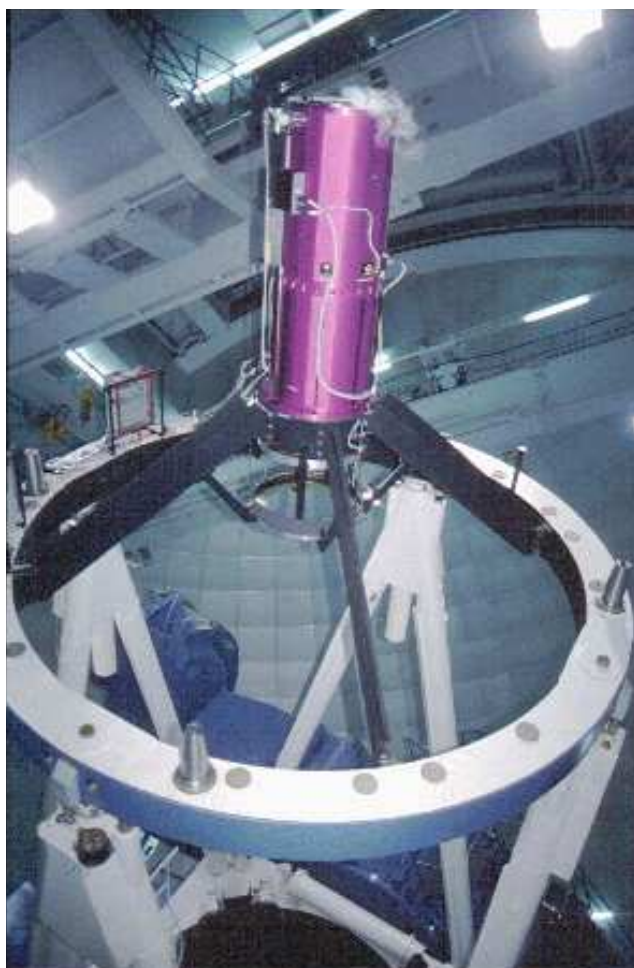
Figure 3.1: Image of OMEGA2000 mounted to the frontring of the 3.5m-telescope.

17
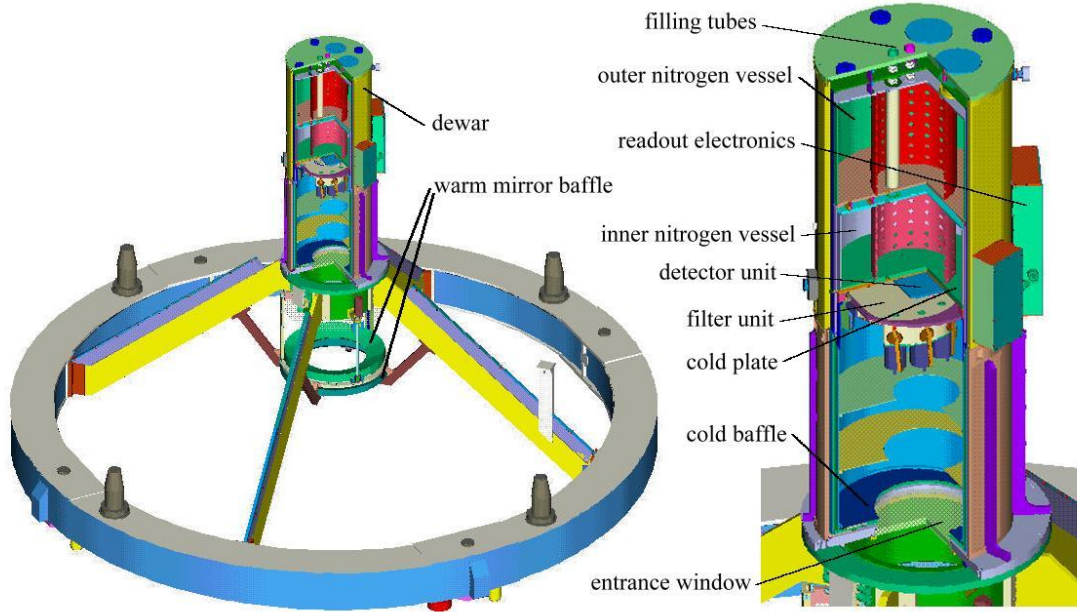
Figure 3.2: OMEGA2000 general design. *Left panel:* Dewar and baffles mounted to the telescope frontring. *Right panel:* Closeup of the dewar with its inner components. From Baumeister *et al.* (2003)

3.2   Design

Figure 3.2 shows the general design of OMEGA2000 as it is mounted to the frontring and of the dewar itself.

With a height of 168 cm and a diameter of 60 cm, the OMEGA2000 dewar contains the detector unit, the filter unit, the optics, and cold baffles. The dewar with all of its inner components is cooled down with liquid nitrogen to the detector operation temperature of 77 Kelvin, which also minimizes the thermal background. The liquid nitrogen for the cooling is stored in an inner and an outer nitrogen vessel with capacities of 47 liters and 72 liters, respectively. With the vessels filled to half capacity — to allow high tilt angles of the telescope — the operation temperature can be retained for about 34 hours. The total cooling time, from room temperature to 77 K, is about 24 hours for all cold parts to reach their minimum temperature. The collection of useful data can already be started after about 13 hours (Baumeister *et al.*, 2003).

The cold plate with the detector unit on top is connected to the inner nitrogen vessel to ensure that it always has the lowest temperature. Going from top to bottom in the right panel of Fig. 3.2, the next unit after the cold plate consists of the three filter wheels, with a total of 17 filter slots. Below the filters is the optics mount with four correction lenses. The cold baffles inside the dewar suppress any stray light. The light enters the

dewar through the entrance window with a diameter of 35 cm. In the left panel of Fig. 3.2, the warm baffles can be seen, one of them being movable.

Due to the considerable size of the dewar and a mounting point to the telescope frontring opposite of the nitrogen tanks (see Fig. 3.2), a thorough deformation analysis of the dewar is required. Finite element simulations show that the dewar deflection at its upper end is at most $45 \,\mu$m for an extreme telescope position looking at the horizon. This deformation corresponds to about a $18 \,\mu$m shift at the detector position and to about $15 \,\mu$m at airmass 2, which is less than the size of one pixel (Baumeister *et al.*, 2003).

All critical instrument components will be discussed separately in the following sections.

Instrument	
field of view	$15.'4 \times 15.'4 = 237$ sq. arcmin
pixel scale	0.45 arcsecs/pixel
focal station	prime focus
dewar dimensions	height 168 cm ; diameter 60 cm
total weight	≈ 300 kg
Detector	
array size	2048×2048 pixels
pixel size	$18 \,\mu$m
wavelength range	0.85-2.5 μm
Telescope	
primary mirror diameter	3.5 m
primary mirror focal ratio	f/3.5
final OMEGA2000 focal ratio	f/2.35

Table 3.1: General OMEGA2000 instrument properties. From Bailer-Jones *et al.* (2000).

3.3   Detector and Readout

At the heart of OMEGA2000 is a HAWAII-2 detector developed and built by *Rockwell Scientific* (see Fig. 3.3). The 2048×2048 pixel array with a pixel size of $18 \,\mu$m and a wavelength range from $0.85 \,\mu$m to $2.5 \,\mu$m is the largest NIR array available at this time. The infrared sensitive material is HgCdTe and the principal detector design is based on the hybrid layout described in Sect. 2.2.2. Table 3.2 lists some important detector properties of the HAWAII-2 array.

With the detector noise as specified in Tab. 3.2, the total noise is — for all practical purposes — always background limited even for narrow-band filters. Under these observing conditions, the most conservative non-destructive readout mode is the *double correlated read* (DCR). In this mode, the whole array is passed three times to achieve a single image. First, the whole array is reset; then, the array is read to determine the pixel bias (offset); and in the final third pass, the light exposed integrated pixel values are measured.
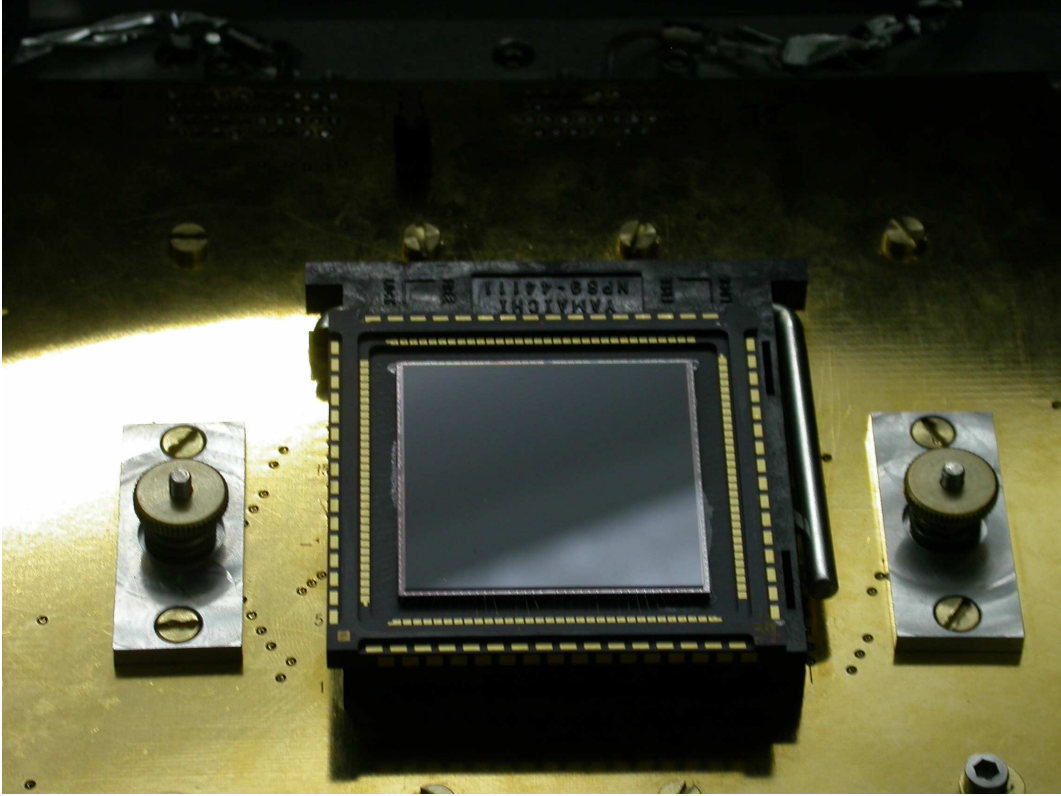
Figure 3.3:   HAWAII-2 detector

The signal is then extracted as the difference between the integrated and the bias values. Because of its better efficiency — which is the ratio of the integration time and the total cycle time for one image — the standard readout mode is the *double correlated read with fast reset*. In this mode the whole array has to be clocked only twice for a single image. This is achieved by a line-oriented approach, where the whole array is clocked line by line. Each line is reset, followed by an immediate read to determine the pixel bias. The second read for the integrated values is then performed at the same clocking speed. OMEGA2000 supports additional readout modes, *e.g.*, the *single correlated read* , but the most common ones are the modes described above (Bailer-Jones *et al.*, 2000).

The detector consists of four electronically independent quadrants each with 8 readout channels. By using these 32 parallel channels for the readout, a maximum data rate of two reads per second is possible. In double correlated read mode, this results in approximately one image per second. In order to reduce the data storage requirement, up to 46 single frames can be kept in memory and only the sum of a specified number of images is saved to disk. With typical integration times of about 30 seconds and a size of 16 MByte per co-added image, the data rate is about 1 GByte per hour.

Parameter	Performance
full well capacity	$\simeq 100{,}000\,\mathrm{e}^-$
quantum efficiency (at 2.3 μm)	55%
good pixels	$> 95\%$
fill factor	90%
read noise	$< 15\,\mathrm{e}^-$
dark current (at 78K)	$< 0.03\,\mathrm{e}^-/\mathrm{sec}$
power dissipation	< 2 mW
number of outputs	32
maximum frame rate	$2\,\mathrm{Hz}$

Table 3.2: Selected HAWAII-2 detector properties. From Haas (2002).

3.4 Optics

The optical system of OMEGA2000 was designed to provide excellent image quality over the entire field of view. Four corrector lenses provide an achromatic image over the whole wavelength range and reduce the telescope focal ratio to $f = 2.35$. The final pixel scale of 0.45 arcsec / pixel is optimized for typical seeing conditions of about $1''$ at Calar Alto to provide sufficient sampling for accurate photometry. The field distortion is specified as $< 0.06\%$, which corresponds to less than one pixel from center-to-corner (Bailer-Jones *et al.*, 2000). This very low distortion permits summation of different images by simple x,y-shifting, which is important for the reduction pipeline discussed in Chap. 5. The actual measurements of the optical quality are summarized in Tab. 4.1.

OMEGA2000 is a non-reimaging camera, which means that no cold Lyot stop can be used to reimage the entrance pupil for minimization of thermal background radiation from structures around the mirror surfaces. This optical design of the OMEGA2000 is at the expense of an increased thermal background in the K-band (see Sect. 2.3.2). To compensate the decreased K-band sensitivity, an innovative baffling scheme was developed, which will be discussed in Sect. 3.6 & 4.3.3.

Figure 3.4 displays the focal reducer and the filter unit mounted on the cold plate of the dewar.

3.5 Filters

OMEGA2000 contains three filter wheels that are independently controlled by cryogenic stepper motors (see Fig. 3.4). Each wheel has seven openings for 3-inch diameter filters. Leaving an open position per wheel and inserting a closed blank, the instrument can hold 17 filters at one time. In Fig. 3.5 the transmission curves for the available filters are shown. A total of 24 filters are provided, including the standard NIR broad-band filters as well as a set of narrow band filters.
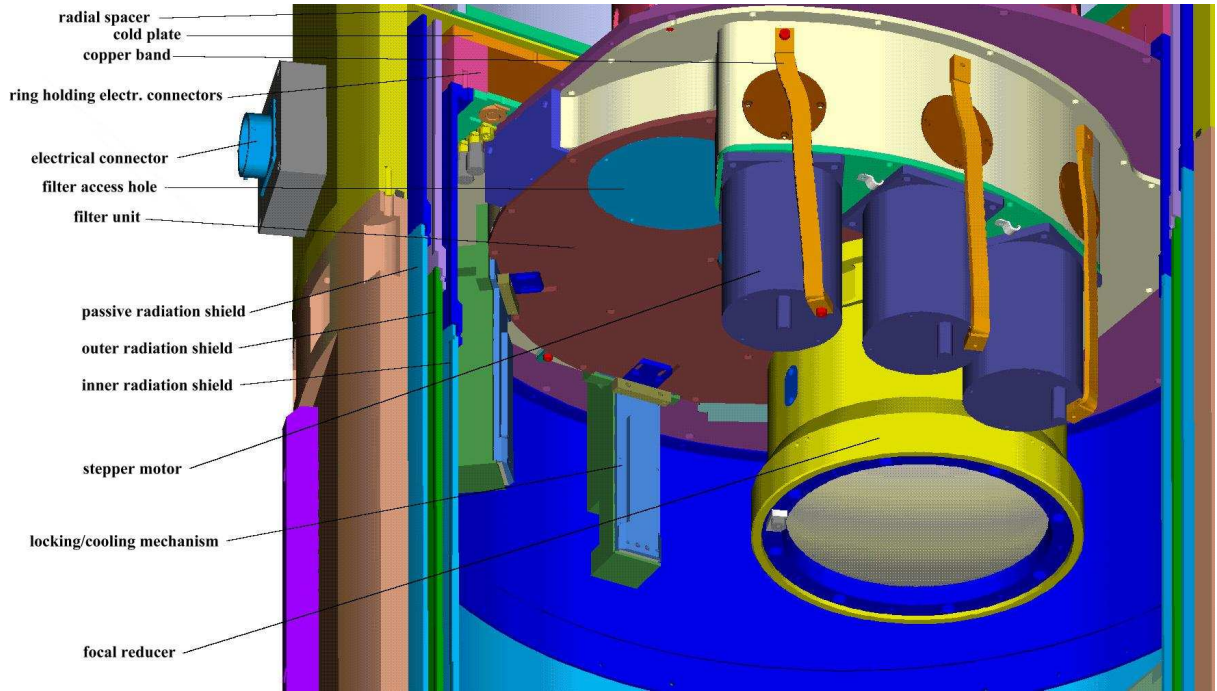
Figure 3.4:   Filter unit and focal reducer. From Baumeister *et al.* (2003).

The narrow band filters for low resolution spectroscopy are selected to cover prominent spectral features of a number of important elements and molecules. As can be seen from the legend of the bottom panel of Fig. 3.5, several IR atomic and molecular hydrogen transitions and individual transitions of helium, oxygen, iron, and carbon monoxide are sampled. With the help of continuum filters that are located between possible emission lines, the level of the continuum flux can be determined.

3.6   Baffles

As mentioned in Sect. 3.4, OMEGA2000 is a non-reimaging camera. With no cold Lyot stop in use, the detector receives additional light from the warm dome floor around the primary mirror. At longer wavelengths, the thermal background becomes dominant and thus reduces K-band sensitivity. With an additional movable warm baffle, the background can be reduced, as explained later in this section.

The detector pixels are sensitive to all light coming from the hemisphere in the direction of the dewar window. Most of this 2π solid angle is blocked by the cold dewar with its cold interior baffles, contributing negligible thermal radiation. An additional highly reflective warm baffle under the dewar entrance window with an ellipsoidal annulus redirects stray light coming from warm surfaces away from the entrance window and light from the cold dewar back into the cold, as can be seen in Fig. 3.6.
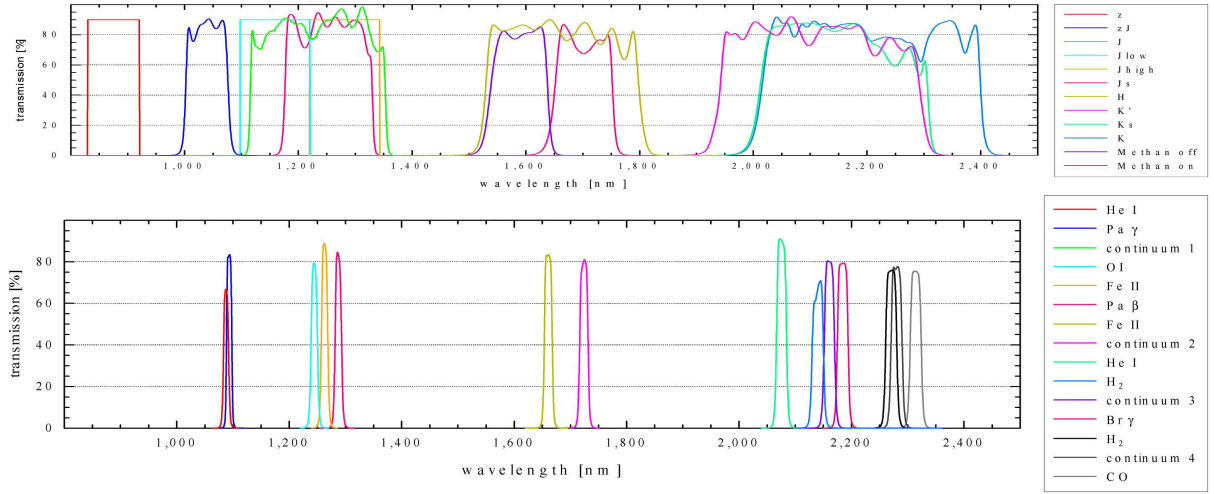
Figure 3.5: OMEGA2000 filter transmission curves. *Top panel:* Transmission of NIR broad-band filters. *Bottom panel:* Transmission of NIR narrow-band filters.

The cold baffles inside the dewar and the fixed warm baffle outside are designed to confine the detector field of view in a way that every pixel receives light from the entire primary mirror. This scheme of baffling without vignetting yields the maximum stellar flux. However, parts of the warm dome floor can be seen by the detector, as depicted in the left panel of Fig. 3.7. While this is the best baffling scheme for all short wavelengths filters, the thermal background becomes critical in the K-band region and is thus reducing K-band sensitivity.

To increase the K-band sensitivity, OMEGA2000 is equipped with an additional under-sized and movable warm baffle to reduce the thermal background from the warm floor. By placing this small baffle in a specified location about 80 cm away from the entrance window, the detector field of view is confined to a vignetting condition, where no pixel can see the warm floor at the expense of an obscuration of parts of the primary mirror, as can be seen in the right panel of Fig. 3.7. Compared to the no-vignetting condition described above, the stellar flux with the undersized baffle in place is decreased, but the signal-to-noise ratio can in principle be improved if the total background is sufficiently reduced by eliminating the contribution from the dome floor (Bailer-Jones *et al.*, 2000).

The effects of the movable warm baffle on the K-band sensitivities have to be tested at the telescope and will be discussed in detail in Sect. 4.3.3.
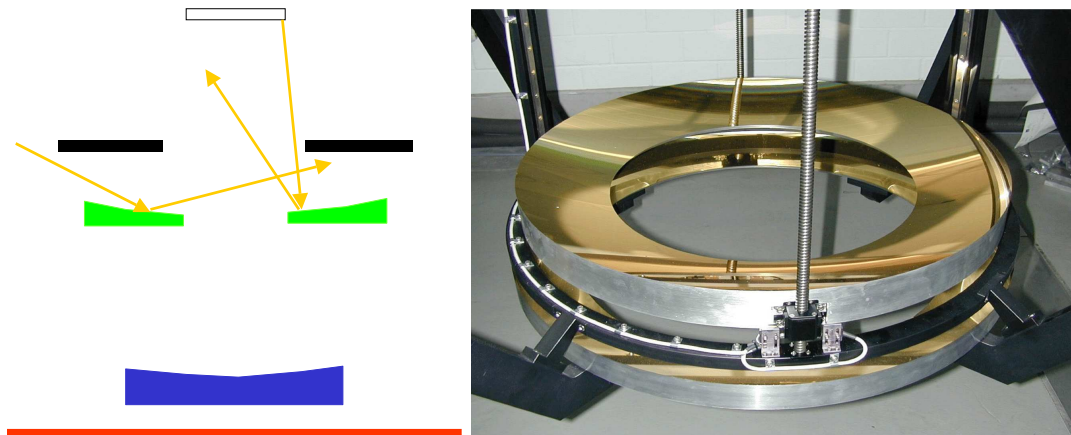
Figure 3.6:   Warm baffle closeup. *Left panel:* Reflection scheme of the warm baffle (green). Light from inside the dewar is reflected back into the cold, infrared radiation coming from surrounding warm parts are reflected away from the entrance window. *Right panel:* Image of the warm baffles. The undersized movable baffle is on top of the fixed baffle.
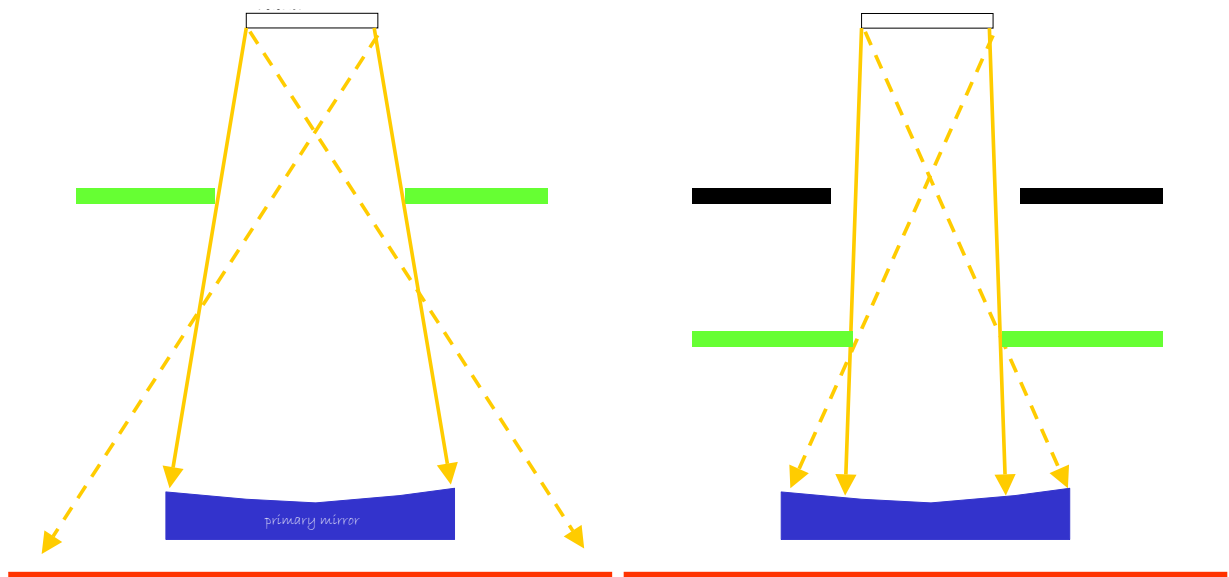
Figure 3.7:   OMEGA 2000 baffling scheme. *Left panel:* Detector view without movable baffle. Radiation from parts of the warm floor can reach the detector. *Right panel:* Detector view with additional warm vignetting baffle (green). No pixel receives thermal radiation from the dome floor at the expense of some mirror vignetting.

Chapter 4

OMEGA2000 Commissioning

4.1 Introduction

The first OMEGA2000 commissioning phase took place between January and April 2003. Two commissioning runs with four observing nights each were scheduled for January 9th – 20th and March 11th – 18th, 2003. A third campaign for the scientific verification of the instrument with additional four observing nights was carried out from April 8th – 14th.

With 2.5 nights of very good observing conditions during the first commissioning run, detailed tests on the image quality and the general characteristics of OMEGA2000 were performed. The second campaign with only about one hour of observations focussed on the optimization of the detector/readout performance and the understanding and solutions of instrument troubleshooting. The third commissioning run, planned as the scientific verification of the instrument, was postponed due to serious detector/readout malfunctioning after one half night of observations. To fully eliminate all problems concerning the detector/readout, OMEGA2000 was shipped back to the MPIA for a final overhaul in early May.

Due to technical problems and bad weather, the commissioning phase of OMEGA2000 could not be completed by May 2003. Tests at the telescope are scheduled to be resumed in July. The instrument is foreseen to be available to the community in August 2003.

Table 4.1 lists some of the most important tasks of the instrument commissioning phase, their results as of May 2003, and the sections with detailed discussion.

4.2 Software Utilities

The basic demands for every NIR observing campaign are focusing the telescope, taking dithered[1] images at a specific pointing position, and taking flatfield images. For the study

---

[1] Dithering in astronomy means taking multiple images of an object with slight telescope offsets from one image to the next. This observing technique allows an accurate determination of the sky background without wasting any observation time. The data reduction of dithered images will be explained in detail in Chap. 5.

Task	Run	Weather Cond.	Results / Section
image quality check	1	good seeing	excellent
distortion measurement	1	good seeing	< 1 pixel (center to corner)
internal reflection check	1,2,3	always	more tests necessary
tip-tilt correction	1,2	good seeing	almost perfect
image mosaic		good seeing	not yet done
integration time test		always	not yet done
observing efficiency check		always	not yet done
Flatfields:			
fixed pattern noise	1,2,3	always	done for some filters
global QE variations		photometric	to be determined
focusing	1,2,3	always	4.2.1
observing macros	1,2,3	always	4.2.2
dome flat macro	2,3	always	4.2.3
tip-tilt measurement	1,2,3	good seeing	4.2.1 & 4.3.2
filter focus offsets	1,3	good seeing	4.3.1
movable baffle influence	1,3	photometric	4.3.3
reduction pipeline	1,2,3	always	5

Table 4.1:   OMEGA2000 commissioning tasks and their status as of May 2003. *Run* indicates the commissioning campaign and *weather cond.* states the necessary observing conditions for the task. The results are either summarized or the section is indicated, where the emphasized tasks are discussed in detail.

of extended objects with sizes comparable to the field of view of the instrument, object observations must be alternated with designated images of the sky that are taken in the vicinity of the object. For all of these basic tasks, automatic observing utilities were developed and tested during the commissioning phase to allow a fast, efficient, and user friendly operation of the OMEGA2000 instrument at the 3.5m-telescope.

All software utilities were developed within ESO's MIDAS (Munich Image Data Analysis System) software package, which provides a high level programming language. The telescope as well as OMEGA2000 can be operated by the software utilities with the use of instrument commands. All routines are called together with user specified parameters — to allow high flexibility — with no further user interaction required during normal operation. The programs can be paused or aborted during the data acquisition process by pushing the appropriate control button in the instrument's graphical user interface (GUI).

4.2.1   Focus applications

One of the first actions of every observation night is determining the proper focus position of the telescope, which is by definition the setting where point-like objects have their minimum seeing-limited full-width half maximum (FWHM). Since the focus position depends on

temperature, telescope inclination, and the filter in use, it is often necessary to refocus the telescope several times in a single night.

For this basic and important procedure — the image quality is highly degraded when the telescope is out of focus — an automatic focus routine was developed that handles everything from taking test images to the final setting of the best telescope focus. The goal was to provide a fast and secure routine that yields an accurate measurement of the best focus. The tedious standard method so far, where the FWHM of a selected star is interactively measured and the focus adjusted to minimize the size of the stellar image, can now be replaced by an automated, fast, and more accurate procedure described below.

Automatic focus routine

Due to the architecture of infrared arrays (see Sect. 2.2.2), where individual pixels are independent and electric charges cannot be shifted across the array, the focusing procedure for OMEGA2000 differs from similar routines[2] for CCD-cameras, where the whole focus analysis is accomplished in a single image.

Figure 4.1 illustrates schematically the layout of the OMEGA2000 focus routine. In Tab. 4.2, the command line parameters for the routine with default values are listed. The procedure can be divided into three parts which can be executed independently or in combination: acquiring test images, object analysis, and setting the telescope to the best focus position.

In the first step, the OMEGA2000 focus routine takes a specified number of images, usually seven or nine, centered around the estimated focus at the current telescope position. An approximate focus can be obtained by knowing the thermal expansion properties of the telescope and the filter influence, which will be discussed in Sect. 4.3.1. The images are taken with focus position offsets of typically $200\,\mu$m, which is achieved by moving the frontring up or down. Focusing can take place essentially anywhere in the sky since the only requirement is a fair number of moderately bright stellar objects within OMEGA2000's field of view. The total exposure time per image should be set to a minimum of 10 seconds in order to achieve well-defined and seeing-limited point spread functions (PSF). The PSFs are thus time-averaged over several atmospheric turbulence time scales and resemble two-dimensional Gaussian distributions (Glass, 1999).

The second and main part of the focus routine carries out an automated object analysis. The image which was taken with the estimated focus value is declared as the master frame. In this image, the specified number of objects is searched by calling an external search routine[3]. The routine returns the central coordinates of the objects found and performs a rough classification into stellar and non-stellar objects. The MIDAS function CENTER/GAUSS[4] is then applied to all returned objects in an area specified by the parameter *box size*. The function performs a Gaussian fit to the intensity distribution

---

[2]Fried, J.W. & Röser, H.J., focus.prg, 1996, private communication. MIDAS focus routine for the MOSCA instrument.

[3]Hippelein, H., findobj.prg & findobj.f, 1992, private communication

[4]For more information consult the MIDAS Manual: *ESO-MIDAS User Guide* (1998), Vol. A

inside the box of interest and returns values for the FWHM in the x- and y-direction and for the central intensity above the background level. Figure 4.2 *top left* shows a histogram of the measured FWHM in the x- and y-direction of about 100 found object candidates in the master frame.

Since the actual focus position is defined as the setting, where point-like sources have their smallest FWHM — which is the *seeing* — only stellar objects should be used for the focus analysis. The selection of appropriate point-like objects is done in a four step selection process, as indicated in Fig. 4.1:

1. Select only objects that were classified as stellar by the search routine.

2. Remove all objects that are very close to the frame edge.

3. Remove all objects with central intensities beyond the linear detector range.

4. Reject remaining galaxies and cosmic ray events by setting appropriate cuts in an intensity plot.

In step 3, all saturated and non-linear range objects were removed, which implies that the remaining stellar objects in the linear detector range all have the same seeing-limited FWHM. Any remaining extended objects, such as galaxies, that passed selection step 1 will be located in a central-intensity vs. FWHM plot well above the virtual horizontal line around which all point-like light sources are statistically distributed. Cosmic-ray events can be identified as objects with a FWHM significantly lower than the seeing. For this reason, in the last selection process the central intensity is plotted against the averaged FWHM in the x-
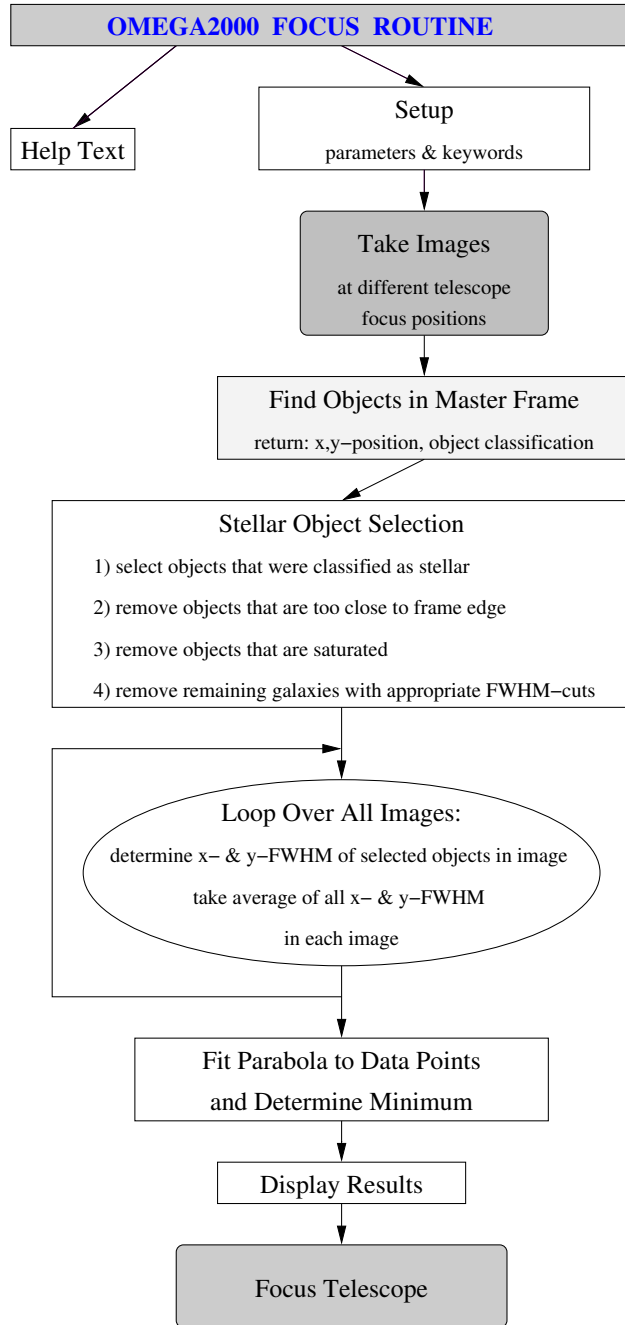

Figure 4.1: Schematic outline of the automatic focus routine.

and y-direction. Since the number of non-stellar objects should be small compared to the stellar sources after the first three selection steps, all remaining outliers can be removed by setting appropriate FWHM-cuts around the average. By using empirically optimized cut values, the whole selection process is automated with no user interaction required. In Fig. 4.2 *top right*, the intensity plot with the minimal and maximal FWHM-cuts is shown. The histogram in Fig. 4.2 *bottom left*, displays the FWHM-distribution of the remaining objects after the complete selection process.

Now that the positions of a sample of point-like light sources are identified, the object analysis with CENTER/GAUSS, as described above, is applied to all images. For each individual image, the average of all x- and y-FWHM values is determined separately, which reduces the error of a single measurement by a factor of $\sqrt{N}$, where N is the number of objects. The determined averaged FWHM values are plotted against the focus position with which the corresponding image was taken. If the minimum is found within the interval of the tested focus positions, the analysis can proceed; otherwise a new focus series with an improved focus estimate is undertaken for better accuracy.

Since all functions with a local minimum can be approximated to first order by a parabola in the vicinity of the extremum, a second-order polynomial fit to the data points is computed using the MIDAS function REGRESSION/POLY. From the returned parabola coefficients of the best fits to the data points, the location of the minimum for each of the two parabolas can be calculated analytically. The best focus position is determined as the mean of the locations of the two minima. The seeing is given by the average of the FWHMs at the position of the minima. Figure 4.2 *bottom right* displays the results of the focus analysis with seeing conditions of 1.1 arcsecs.

The separate parabola fits for the x- and y-direction can be used as a check of the optical image quality. Ideally, the fits in the different directions should be identical, whereas optical aberrations can cause asymmetry of the stellar images which subsequently introduce systematic deviations of the two parabolas.

Finally, the telescope focus is adjusted to the determined best focus position. The telescope and the instrument are now ready for scientific observations.

Local focus determination

The focus at every point on the detector is a fundamental requirement in achieving excellent optical quality over the whole field of view. This implies that the focal plane of the telescope, which is perpendicular to the optical axis, must be identical with the detector plane. A non-uniform focus on the detector can be caused by optical aberrations, a curved detector surface, or tip-tilt of the detector. Since the tolerances for an optimal detector placement are at the limit of technically feasible precision, the orientation of the detector has to be measured empirically and optimized, if necessary. In order to check the local focus positions across the detector and allow possible tip-tilt corrections, an automatic routine was developed that determines the local focus positions and displays the variations across the detector.

The local focus routine is a modification of the above described program, which averages

Parameter	Default	Description
name & index	automatic	names of the images to be analyzed ; can be set to automatic, *i.e.*, names in GUI will be used
focus & step	24000,200 μm	approximate focus position around which images are taken with focus offsets of *step* μm
Nºimages	7	total number of focus images to be taken and analyzed
integration time	20,2 s	integration time in seconds for the integrated image to be saved and the single exposure
action flag	all	specifies whether new focus images are taken, analysis is done, and focus is adjusted
Nºobjects	40	number of objects to be found and analyzed
box size	18″	area around object that is used for the object analysis

Table 4.2: Focus routine command line parameters. Default values are used, if parameters are not specified by the user.

the FWHM measurements to determine the best global focus. In a first pass, the code of the normal focus routine (Fig. 4.1) is executed yielding the global, averaged focus, which is taken as the reference value. In addition, the individual stellar object measurements of the x- and y-FWHM are now stored together with the position on the detector. In a second pass, the focus analysis as above is carried out for each individual star in a loop over all selected objects. As result of the parabola fits to the individual data point sets, the best local focus positions are now known. Since only the variations of the focus value across the detector field of view are of main interest, the difference of the local focus value and the global focus is computed and the results written in an image frame at the position of the measurement. If an appropriate test field in the sky with many stellar objects was chosen, more than 100 local focus positions can be determined and plotted from a single focus series.

The results of this analysis for OMEGA2000 will be discussed in Sect. 4.3.2.

4.2.2   Observing utilities

The basic observing strategy for NIR imaging is taking multiple exposures at the same principal position with slight telescope offsets in between the images. This technique of *dithering* allows the extraction of the local background from the science frames (see Sect. 5.3.1).

The developed observing utilities described below handle the interplay of the telescope and OMEGA2000 to allow easy and efficient observations with the instrument. In addition, the routines prepare the pipeline data reduction (Chap. 5) by creating image catalogs and storing information necessary for the further online data processing. The command line parameters of the observing utilities are listed in Tab. 4.3.
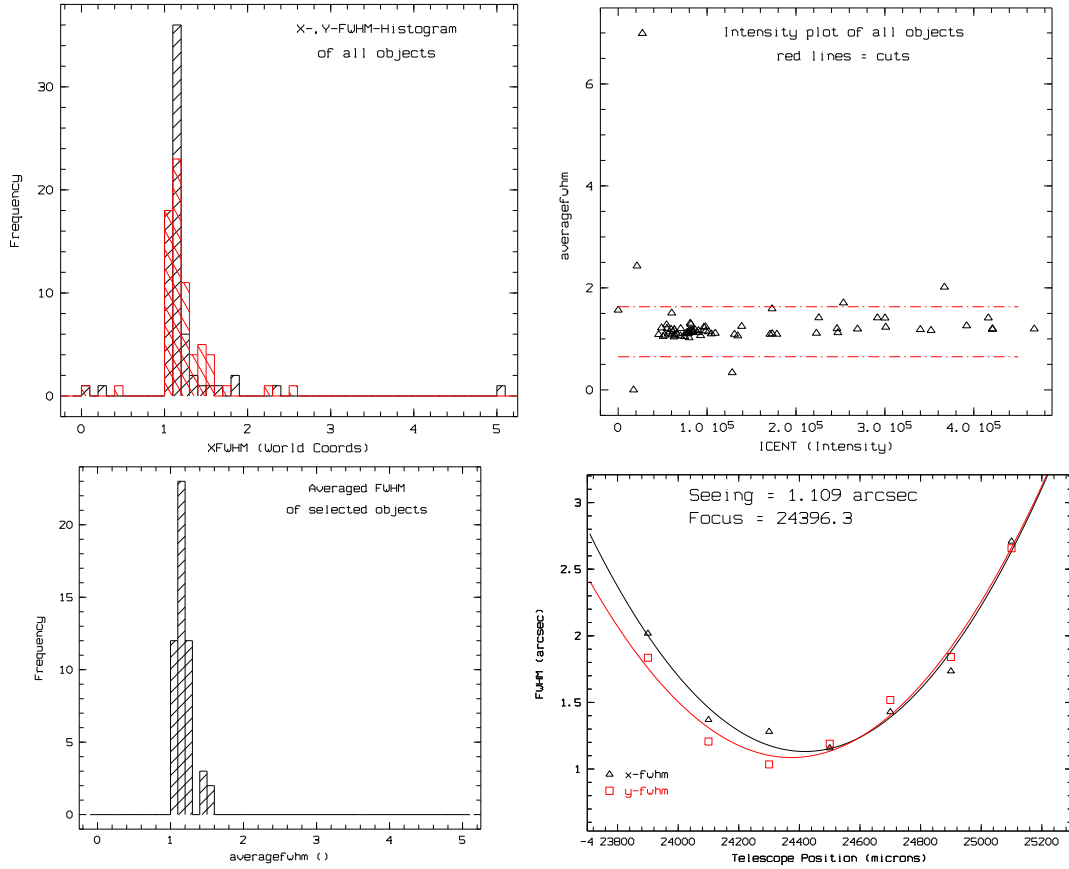
Figure 4.2: Selection process and results of the automatic focus routine. *Top left panel:* Histogram of the x- and y-FWHM-distribution of all object candidates. The unit of the abscissa is arc seconds. *Top right panel:* Intensity plot of the object candidates. The horizontal lines indicate the cut values for the final object selection. *Bottom left panel:* FWHM-histogram of the selected stellar objects. *Bottom right panel:* Data points, fit parabolas and results of the focus analysis.

Normal observations

The term *normal observations* in the context of this thesis denotes observations of sky areas with sparse object coverage. This means that most detector pixels receive only background and no object flux. In particular, no objects with sizes comparable to the field of view of the instrument should be in the image. If these conditions are fulfilled, the local background flux can be determined accurately from the science frames and no time consuming designated sky observations are necessary.

Typical *normal observations* are most astronomical surveys, where a large area is to be covered. Distant galaxy surveys, for example, are usually conducted in selected sparse sky areas with no large extended foreground objects (see Sect. 7.2).

The routine for this observation mode takes dithered images at the current telescope position. Three different integration times have to be specified by user input:

Parameter	Default	Description
integration time		exposure times for the pointing, an integrated
		exposure, and a single image in seconds
offset flag	integer	telescope offsets can be multiples of the
		pixel scale or non-integer offsets
start position	1	dither position from which to start
object		text for the image identification descriptor
pointing		pointing number for the image descriptor
image catalog		name of image catalog to be passed
		to the pipeline reduction
sky distance	30$'$	telescope offset for the designated sky area
sky direction	all	direction from the object to the designated sky area;
		can be set to N,S,E,W or to ALL

Table 4.3:   Command line parameters for the observing utilities. Default values are used, if parameters are not specified by the user. Top: Parameters used for both routines. Bottom: Additional parameters for the observation of extended objects.

- The integration time for a single exposure. This time is filter dependent and must be set in a way that the count levels for the objects of interest are still within the linear detector regime and the image is background limited.

- The time for the integrated image saving. Several single exposures can be added up in memory and only the sum is written to disk. This is also the total integration time at one dither position after which the telescope is moved. The parameter is filter dependent, but a typical setting is 30 s to keep track of the sky background variations.

- The total integration time for the pointing. This parameter specifies the exposure time of the combined sum image and thus determines the signal-to-noise ratio and the limiting magnitude.

After each image that has been saved to disk, *i.e.*, after the second time parameter, the telescope is moved by an offset of typically 20 arcsecs. The offsets have to be large enough to ensure that the images of the same object do not overlap when two consecutive exposures are overlaid. This condition is critical for an accurate local background determination which uses a median process over a stack of images to remove the objects (see Chap. 5.3.1). On the other hand, the offsets should be small compared to the field of view to ensure maximal overlap of all images after the summation process in world coordinates. All offsets relative to the origin position will result in areas, where not all images overlap. The on-overlapping areas should be minimized. To account for these considerations, the dither pattern as shown in Fig. 4.3 *left* is implemented in the routine. The solid lines depict the telescope movements for 20 dither positions. This is the fundamental dither pattern, with positions
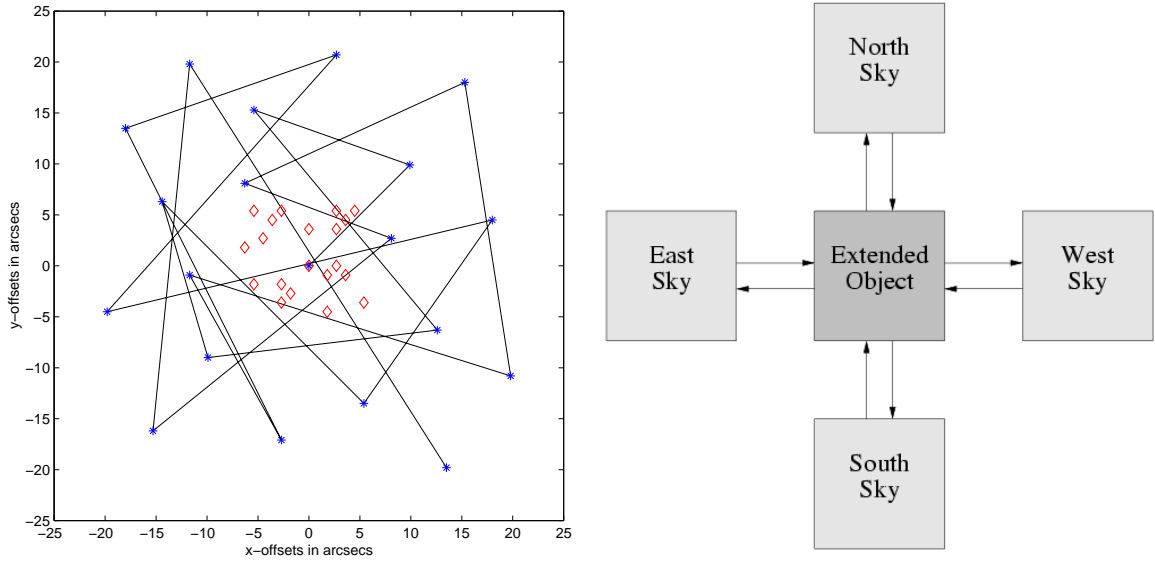
Figure 4.3: Telescope offsets for the observing macros. *Left panel:* Dither sequence for one pointing. The blue asterisks depict the central telescope positions relative to the origin. After 20 positions, the dither sequence is repeated with a shifted origin (red diamonds). *Right panel:* Large extended objects are observed by taking alternate images of the object and the sky at a specified position.

within a distance of 20 arcsecs in each direction from the origin. After 20 images, the origin is shifted by typically 5 arcsecs, depicted by the red diamonds in Fig. 4.3 *left*. By using this strategy, up to 400 images with different offsets can be taken. The non-overlapping area is at most 25 arcsecs at a side. After 400 images, the sequence starts back at the beginning.

To allow a better alignment of the images during the summation process, described in Chap. 5, the offsets are by default multiples of the OMEGA2000 pixel scale of $0.45''$/pixel. Under very good seeing conditions, where sampling is critical, the offsets can be set to non-integer values, which allows the use of elaborate algorithms[5] for an improved PSF reconstruction. The observations can also be re-started at an arbitrary position of the dither pattern by specifying the appropriate parameter.

Observations of extended objects

For the study of extended astronomical objects with angular sizes larger than the dither offsets described above and for dense fields with stars covering a fair fraction of the total field of view, a different observing technique is employed. In this case, the local sky background cannot be extracted accurately from the science images, since the objects overlap when overlaying the frames. In order to determine the background levels in the object image, a designated sky area must be observed alternately in the vicinity of the

---

[5]Such algorithms were developed for the HST and are known as DRIZZLE. Further information can be found in Mutchler, M. & Fruchter, A. (1997) and Fruchter, A.S. & Hook, R.N. (2002).

object. The sky field should fulfill the requirements described above for normal observations to allow accurate background modelling. In addition, the field should be close to the object and observed in short succession to determine the *local* and *current* background (see Sect. 2.3.1 & 6.1).

To account for the considerations above, a second observing utility for OMEGA2000 is provided. The utility is called with two additional parameters for the sky specification, as can be seen in Tab. 4.3. The designated sky field is defined by providing the angular distance and the direction from the object. If no direction is specified, eight different sky positions around the object at the given angular distance will be used.

The object of interest is observed with the same dither pattern as discussed above. In between the different dither positions, *i.e.*, after each integrated image, the telescope is moved to the designated sky area, where a frame is taken at the current dither position. After the sky image is obtained, the telescope is returned to the object position and the pattern continues. Figure 4.3 *right* illustrates the alternate observations of object and sky. The dither pattern in Fig. 4.3 *left* is applied simultaneously to the sky and object positions.

With this observing strategy, the current local background can be constructed from temporally correlated sky frames, which can then be used for the reduction of the science image.

4.2.3   Flatfielding

The so-called *fixed pattern noise* (FPN) — the pixel-to-pixel sensitivity variations on the detector — is corrected by dividing the science image by a normalized flatfield. The flatfields are obtained by taking images of uniformly illuminated areas, usually the sky during twilight (sky flats) or the interior of the telescope dome (dome flats).

Dome flatfields can be taken by illuminating the interior of the dome with special flatfield-lamps that provide a well defined and steady continuum spectrum without any emission lines. Since the detector sensitivity variations are wavelength dependent, flatfields are needed for all filters used for the observations, thus requiring flatfield-lamps of different spectral power. In order to obtain good flatfield images, the integration time for a single exposure should be set in a way that count levels are well within the linear regime of the detector. The total exposure time or the total number of images is chosen to achieve a specified signal-to-noise-ratio (SNR). Given the conditions for the linear range and the total count level for a certain SNR, an appropriate flatfield-lamp has to be selected for efficient data taking. This interactive process for the acquisition of good flatfield data can now be handled by an automated procedure.

The automatic OMEGA2000 flatfield routine takes as an input parameter the total count level necessary to achieve the desired signal-to-noise ratio. Presumably the most appropriate flatfield lamp can be optionally given. The routine takes a short test exposure with the current filter and does a fast statistical analysis to determine the average level of the image. If the count level is not within a given interval, which is defined according to the linear range and the minimal integration time of the detector, a new test exposure is begun with a more appropriate flatfield-lamp. When the best and most efficient lamp is found, the

flatfield data acquisition starts with the optimized integration time. Flatfields are taken until the specified total count level is reached. The images can be saved individually, or only the integrated flatfield is written to disk.

4.3 Commissioning Results

4.3.1 Determination of filter offsets

General considerations

Positioning the detector in the focal plane of the telescope is a critical requirement in order to achieve the best possible image quality. The automatic focus routine, as presented in Sect. 4.2.1, is able to find and adjust the focus position within a few minutes. While the absolute focus determination is inevitable at the beginning of each observing night, refocusing with the above method during the night should be kept to a minimum for time efficiency reasons. Since the absolute position of the focal plane is affected by several parameters that can change over the course of the night, the resulting focus offsets have to be adjusted automatically to allow continuous observations. The following parameters account for the largest fraction of the focal plane shift:

Temperature: Due to the thermal expansion of the structural elements of the telescope, the distance from the primary mirror to the instrument will increase with temperature. With a linear thermal expansion coefficient of steel of $\alpha = 16.0 \times 10^{-6}\,\mathrm{K}^{-1}$ (Stöcker, 1998) and a distance from the primary mirror to the frontring of about $10\,\mathrm{m}$, the total expansion of the telescope structure can be approximated to be $\mathcal{O}(-160\,\mu\mathrm{m}\,\mathrm{K}^{-1})$. The exact value implemented in the telescope software is $-165\,\mu\mathrm{m}\,\mathrm{K}^{-1}$. To compensate for this expansion effect, the focus position must be set back by the above value for every degree rise in temperature.

Telescope Inclination: The mechanical flexure of the structural elements is a function of the telescope position and has to be corrected. This flexure also depends on the weight and dimensions of the prime focus instrument (or the secondary mirror) mounted to the frontring.

Filter: As an additional optical element, a filter can introduce a systematic shift of the focus position. Since the filters lie in the converging light beam between the optics and the detector, variations in thickness and refractive index can cause focal plane offsets. The relevant quantity is the optical path length τ, which is the product of the refractive index n and the geometrical thickness of the filter d.

The first two items are telescope properties that are well understood and are automatically corrected by the telescope control software. The systematic offsets introduced by the filters have to be measured individually to allow an automatic adjustment of the focus with each filter change.

Measurement and results

During the first commissioning run in January, the relative offsets of 10 filters were determined. The temperature at the time of measurement was almost constant at $(-1.6 \pm 0.1)\,°C$. The seeing varied between 1.1 and 1.6 arcsecs.

The measurements were carried out with the automatic focus routine described in Sect. 4.2.1. For each focus series, 7 images were taken with focus steps of $200\,\mu m$ in between. The integration time per image was set to 10 or 16 seconds depending on the filter and 40 objects were selected for the analysis.

The K'-filter with a central wavelength of λ_c=2.1 μm was chosen as the reference filter. All offsets are determined relative to this filter. To correct for systematic drift with time, the measurement of the reference filter was repeated after every second focus series. The absolute focus position of the reference filter drifted within the two hours of measurement from $24284\,\mu m$ to $24232\,\mu m$, which corresponds roughly to the expected shift due to the slight temperature increase from -1.7 to $-1.5\,°C$ (see above). When averaging the enclosing measurements, the reference value at the time of the filter offset determination can be given to within an error of $10\,\mu m$. Assuming an additional uncertainty of $10\,\mu m$ of the individual focus measurement, the total error of the filter offset determination can be specified as $\pm 15\,\mu m$.

The results of the filter offset measurements are summarized in Tab. 4.4. Although all OMEGA2000 filters were specified to have identical focus properties, significant offsets of up to $300\,\mu m$ between the filters were measured. As can be seen in the typical focus curve in Fig. 4.2, a deviation from the best focus position of $300\,\mu m$ results in a frame-FWHM of about 0.3 arcsecs above the seeing. A deviation of $200\,\mu m$ still adds about 0.1 arcsecs to the FWHM of the point-spread function. This implies that the telescope focus needs to be automatically adjusted by the measured offsets after each filter change in order to avoid a loss of image quality.

4.3.2   Detector tip-tilt measurement

The focus variations across the detector were determined at the beginning of the first commissioning run in January. The measurements presented here yield the detector orientation as used throughout the first campaign. Essentially all images used in this thesis were taken with the detector setup described below.

Measurement

The local focus positions were determined using the routine presented in Sect. 4.2.1. Focus test images of the open star cluster M67 allowed the measurement of about 120 local foci across the whole detector. Figure 4.4 depicts the results of this analysis. The colored squares indicate the positions on the detector where appropriate stellar objects were located and the local focus was determined. The local focus difference compared to the best averaged focus is indicated by the color of the square. The cuts for the color encoding are set from $-200\,\mu m$ (pink) to $+200\,\mu m$ (black). The averaged focus is the reference value and is set to 0 (yellow). Green squares depict deviations of about $+50\,\mu m$, orange ones of about $-50\,\mu m$.

Filter	Central Wavelength [μm]	Filter Offsets [μm]
K'	2.08	0
Z (d)	0.90	+80
ZJ (d)	1.08	+190
H (d)	1.65	+150
Ks	2.16	+95
K	2.18	−5
NB1094 (d)	1.09	+110
NB1207 (d)	1.21	+335
NB1237 (d)	1.24	+240
NB1282 (d)	1.28	+70

Table 4.4: Measured filter focus offsets for broad-band (*top*) and narrow-band filters (*bottom*). The offsets are determined relative to the reference filter K' with an absolute focus position of about 24260 μm. The temperature at the time of measurement was $(-1.6\pm0.1)\,°$C and the measured seeing was between 1.1 and 1.6 arcsecs. All determined offsets have an absolute error of $\pm15\,\mu$m. The filters marked with *(d)* showed signs of defective properties that require further investigations.

Discussion

The distribution of the focus positions across the detector — as depicted by the different colors in Fig. 4.4 — indicates a systematic tip-tilt of the detector plane. As can be seen by the green and blue squares, the lower right corner of the detector shows a steady drift towards higher than average focus positions, whereas the upper left corner has offsets towards lower focus values (orange and red squares). This implies that the detector plane is slightly tilted against the true focal plane. The tilt axis is approximately given by the diagonal from the lower left to the upper right corner, where mostly focus positions close to the best averaged focus are located (yellow squares). About 80% of all measurements are found within the interval $[-50\,\mu$m, $+50\,\mu$m] and more than 90% lie in the range $[-100\,\mu$m, $+100\,\mu$m]. The systematic maximal deviation from the true focal plane can thus be estimated to be $+100\,\mu$m in the lower right and $-100\,\mu$m in the upper left corner of the detector, with an error of about $\pm20\,\mu$m.

As can be seen in Fig. 4.2, an offset of $\pm100\,\mu$m from the best focus will result in an increased FWHM of the PSF of less than 0.05 arcsecs. An offset of $\pm50\,\mu$m has almost no effect on the FWHM, since the derivative of the FWHM-focus-parabola is 0 at the minimum. Even though a systematic tip-tilt of the detector plane was found, the deviations from the FWHM minimum of less than 0.05 arcsecs across the detector are already tolerable.

A correction and optimization of the detector tip-tilt can in principle be achieved by adjusting the detector mounting on the cold plate (see Sect. 3.2). This is a rather crude measure and for corrections of $\mathcal{O}(100\,\mu$m) beyond the mechanical precision. In order to determine the actual tilt of the detector with respect to the focal plane, the effect of the
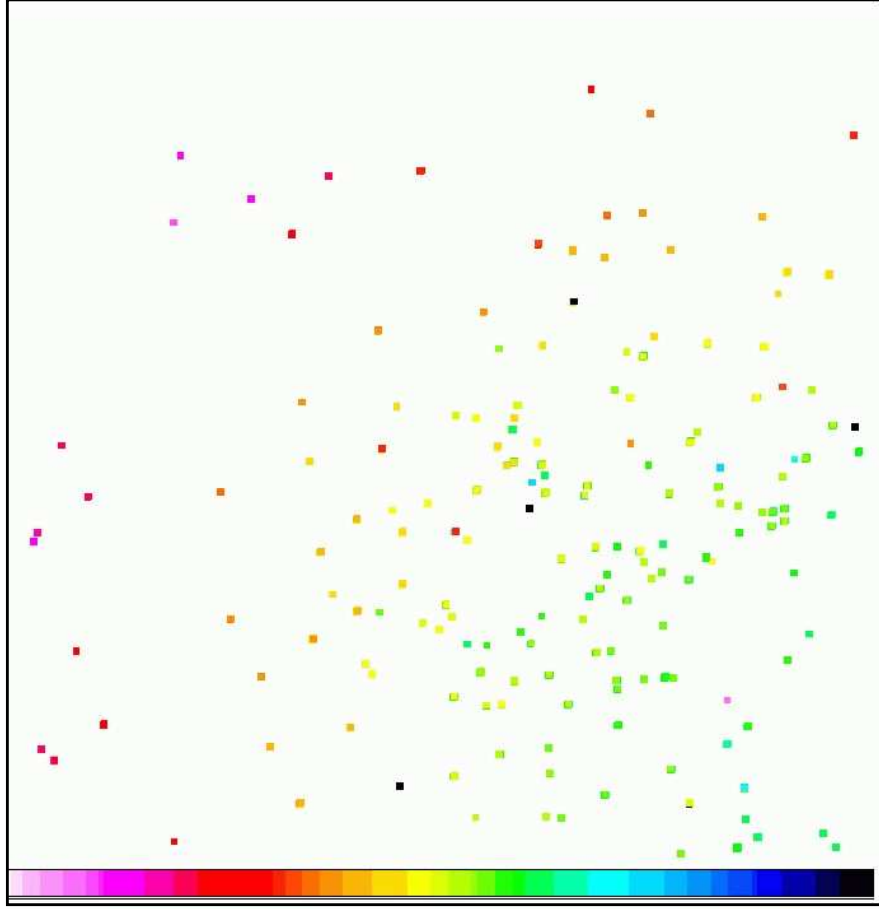
Figure 4.4:   Detector tip-tilt measurement. The colored squares indicate the local focus at this position on the detector. Plotted is the difference of the local focus to the averaged best focus. The cuts for the color bar are set from $-200\,\mu$m (pink) to $+200\,\mu$m (black), with the averaged focus as reference at 0 (yellow).

optical system has to be included in the calculation. Numerical simulations have shown that a focus deviation of $100\,\mu$m in the detector corner corresponds to a physical misalignment of only $44\,\mu$m. This implies that the current detector tilt of less than $50\,\mu$m is at the limit of mechanical feasibility and cannot be further improved.

OMEGA2000's detector tip-tilt will have to be redetermined during the final commissioning phase. Considering the results discussed above, a constant focus position across the full detector field of view should be achievable for all future observations.

4.3.3   Movable baffle

In this section the effects of the movable warm baffle on the OMEGA2000 K-band sensitivity will be discussed. The baffling scheme was described in detail in Sect. 3.6. Before the results are presented, the relevant quantities are introduced and the predictions discussed.

Signal-to-noise considerations and specifications

The signal-to-noise ratio (SNR) of a star measurement in the background limited case — which is always true for K-band observations with OMEGA2000 — is simply given by

$$SNR = \frac{\text{total measured star flux}}{\sqrt{\text{total measured background}}} = \frac{Z(r) \cdot t}{\sqrt{n \cdot z_{sky} \cdot t}} \propto \sqrt{t}. \tag{4.1}$$

Here, t is the observation time in seconds, $Z(r)$ the total measured stellar intensity (e^-/sec) within an aperture of radius r, z_{sky} the local sky background intensity (e^-/sec/pixel), and $n \approx \pi r^2$ the number of pixels within the aperture (Harris, 1990). The quantity of interest for the analysis below is SNR_{Ratio}, which is the ratio of the signal-to-noise ratios measured with and without the movable baffle:

$$SNR_{Ratio} = \frac{SNR_{with}}{SNR_{without}} = \frac{\sqrt{\frac{(n \cdot z_{sky})_{with}}{(n \cdot z_{sky})_{without}}}}{\frac{Z_{with}}{Z_{without}}} = \frac{\sqrt{\frac{(z_{sky})_{with}}{(z_{sky})_{without}}}}{VT}. \tag{4.2}$$

The quantity SNR_{Ratio} is a measure for the change in the SNR due to the effect of the additional baffle if images with the same integration time t are compared. All quantities that are referring to images taken with the movable warm baffle in use, *i.e.*, the vignetting condition, are denoted with the subscript "with" and with the baffle removed, *i.e.*, without vignetting, with the subscript "without". Note that SNR_{Ratio} does not depend on the seeing since the number of pixels n cancel. As long as all count levels are within the linear detector range, the quantity is also independent of the star flux. Moreover, the ratio of the star intensities with and without baffle is given by the *vignetting transmission* in the obscured case, denoted as VT, which is the fraction of source light from the primary mirror that reaches the detector (Bailer-Jones *et al.*, 2000). Since no vignetting occurs without the additional baffle and the decreased effective primary mirror area is the same for all pixels with baffle, SNR_{Ratio} is constant over the whole detector field of view (see Sect. 3.6).

For many observations, the total integration time t is predetermined to reach a certain limiting magnitude, *i.e.*, the SNR of the faintest object to be visible is given. From Equ. 4.1 & 4.2 it can be inferred that the observation times to reach a particular SNR for an object with and without baffle scale as

$$t_{without} = t_{with} \cdot (SNR_{Ratio})^2. \tag{4.3}$$

Extensive calculations on the OMEGA2000 baffling scheme were carried out by Bailer-Jones *et al.* (2000). The vignetting transmission with the movable warm baffle in place is specified as $VT = 0.90$. This implies that a positive effect on the SNR with baffle is only expected if the sky background is reduced by more than 19%, as can be seen from Equ. 4.2.

The predicted SNR-improving effect of the additional warm baffle in summer conditions was calculated to be about 5%, *i.e.*, $SNR_{Ratio} \approx 1.05$. This would result in about a 10% shorter integration time to reach a given SNR, as can be seen from Equ. 4.3. For this theoretical quantification of the baffle influence, various assumptions and simplifications
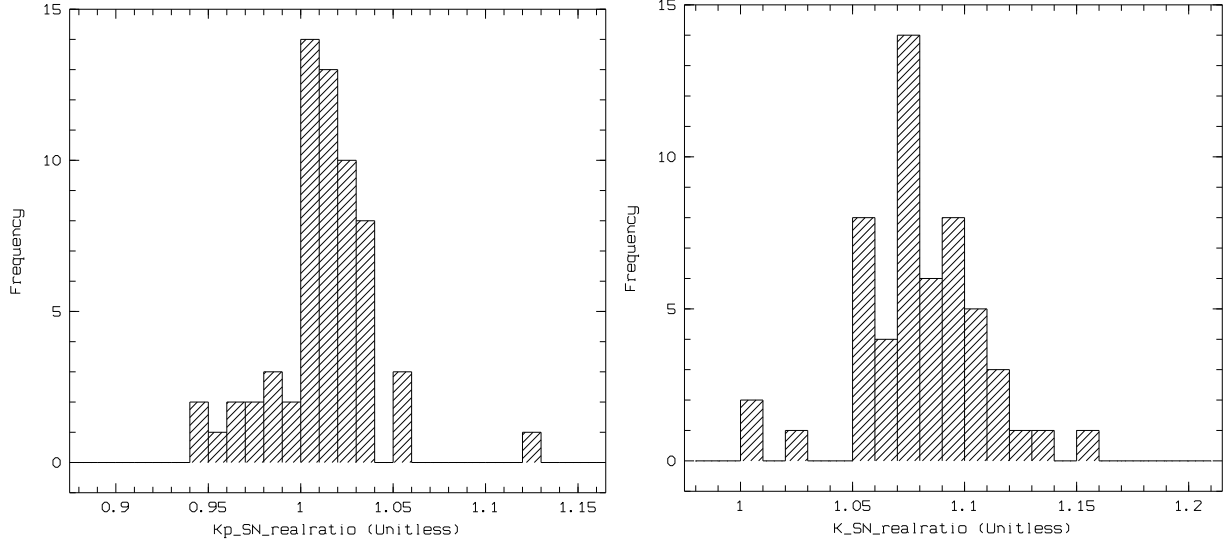
Figure 4.5:   Movable baffle measurement. Histogram of the SNR-ratios with and without the movable baffle. *Left panel:* K'-filter. *Right panel:* K-filter.

on surface emissivities, thermal background sources, and especially the contribution of OH-sky-emissions to the total background are made. For these reasons, the simulated values above should only be a rough estimate of the actual influence of the movable baffle on the SNR.

Measurements and results

In order to empirically determine the effect of the additional undersized warm baffle, images of M67 were taken with and without baffle in the K- and K'-filter with a total exposure time per setup of 100 seconds. The data was acquired during the January campaign under excellent observing conditions with an outside temperature of $0\,^{\circ}$C.

The raw data frames were flatfield corrected to allow a more accurate measurement of the local sky background. 61 objects distributed over the whole field of view were selected and analyzed for the four different conditions: K-filter with and without, and K'-filter with and without baffle. For the object analysis the MIDAS function INTEGRATE/STAR was used which determines the local sky background z_{sky} and the integrated stellar flux Z in a given aperture. With z_{sky} and Z measured with and without baffle, SNR_{Ratio} for a given filter and object can be determined using Equ. 4.2.

Figure 4.5 displays the histograms of the SNR_{Ratio} distributions of the individual object measurements in K' (left panel) and K (right panel). To avoid a systematic bias towards higher values, saturated objects — occurring only in K without baffle — were excluded leaving 54 objects for the analysis in the K-filter. The results with errors for the different filters are given in Tab. 4.5.

The analysis showed that the movable warm baffle in place improves the signal-to-noise
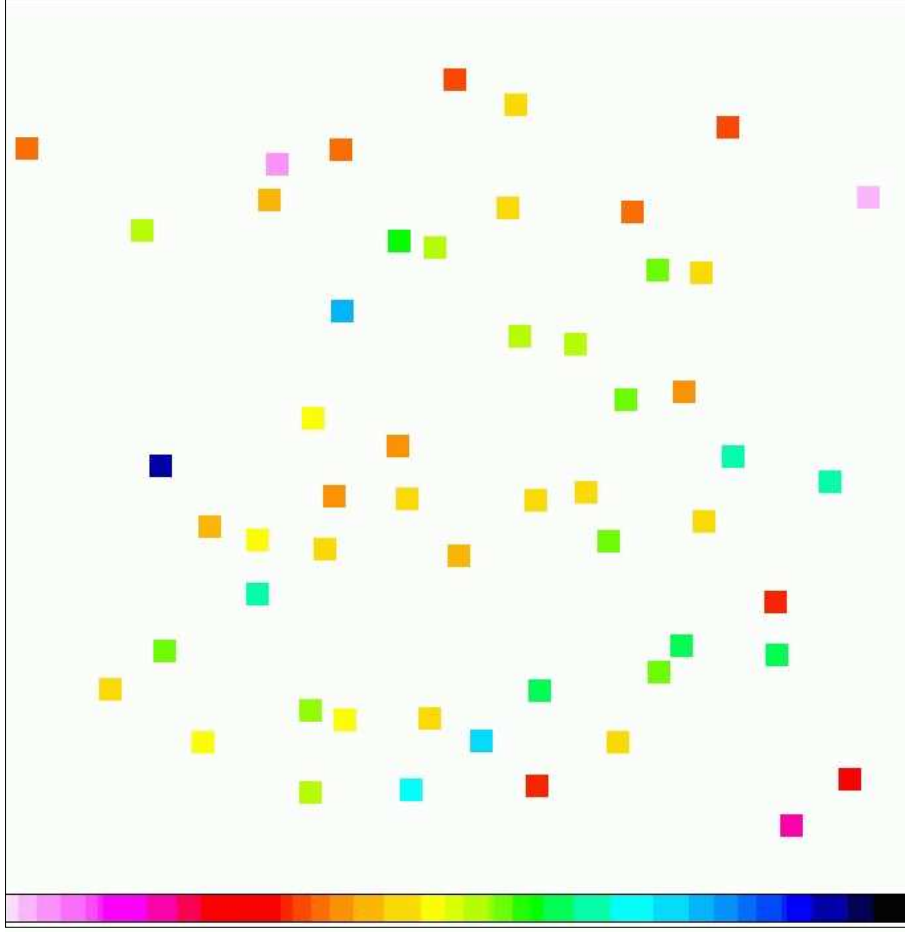
Figure 4.6: Local SNR-ratio (with baffle / without baffle) determination for the K-filter across the field of view of the detector . The colors indicate the measured local value. The cuts for the color-bar are set from 1.00 (pink) to 1.17 (black).

ratio in the K-filter by about 8%. This will result in approximately 14% less observation time needed to reach a given limiting magnitude, as can be seen in the last column of Tab. 4.5.

The SNR improvement with a K'-filter in use is only about 1% with an integration time saving of roughly 2%. The reduced thermal background in K' is almost compensated by the stellar flux loss due to the vignetting.

The empirically measured vignetting transmission VT, which is just given by the stellar flux ratio with and without vignetting baffle, can be determined from Tab. 4.5 to be $VT = 0.895 \pm 0.015$. This implies that the movable warm baffle has a positive effect on the signal to noise ratio if it reduces the total background reaching the detector by more than 20%, which agrees with the prediction.

Filter	Flux Ratio	Background Ratio	SNR Ratio	$t_{with}/t_{without}$
K'	0.896 ± 0.023	0.786 ± 0.0083	1.012 ± 0.027	0.977 ± 0.053
K	0.893 ± 0.021	0.684 ± 0.011	1.080 ± 0.27	0.857 ± 0.043

Table 4.5: Effects of the movable warm baffle on the SNR and the observation time. The temperature at the time of measurement was $0\,^{\circ}$C. The values are the averaged ratios of the listed quantities, where always the measurement with baffle is divided by the one without. SNR_{Ratio} is determined as stated in Equ. 4.2, $t_{with}/t_{without}$ according to Equ. 4.3.

In order to rule out a possible variation of the SNR-improving effect across the field of view of the detector, the local SNR_{Ratio} in the K-band was plotted as is displayed in Fig. 4.6. The colored squares again indicate the local measurement of SNR_{Ratio}, with the cuts for the color-bar set from 1.00 (pink) to 1.17 (black), and the average effect of 1.08 being yellow. The 54 local SNR_{Ratio} seem to have statistically scattered values with no observed systematic tendency. This confirms that the movable baffle has a uniform effect across the whole detector as specified.

The predicted SNR-improving effect of about 5% is roughly the average of the two determined values of 8% in K and 1% in K'. The measurement, however, was conducted during winter season at a temperature near $0\,^{\circ}$C. The improvement should be better for summer time observations, where the fraction of thermal background to the total background is significantly higher.

Chapter 5

Data Reduction Pipeline

In this chapter the structure and performance of the newly developed OMEGA2000 data reduction pipeline will be presented. The pipeline will allow "online" reduction at the telescope, which means that reduced images will be available to the observer shortly after the data have been taken.

5.1 Motivation

Why is it important to have immediate access to reduced images during infrared observations? The answer is evident when taking a close look at a raw image as shown in Fig. 5.1. The displayed data frame is a typical example of an unprocessed OMEGA2000 image as it is written to disk. Imaged is a sparse field with an extragalactic object in the center and no bright stars in the field of view, as will be visible in the processed data shown in Sect. 5.4. In fact, not a single astronomical object is recognizable in Fig. 5.1. The science content of the image is well hidden in the background and the detector imperfections. Some of the most important and obvious OMEGA2000 detector characteristics are labelled in Fig. 5.1:

Inhomogeneous Quantum Efficiency: The detector suffers from a severe drop in quantum efficiency (QE) in the right part, especially in the upper right corner. The sensitivity in these areas is up to a factor 2 lower than in the center.

Bad Pixels: There are $\mathcal{O}(1000)$ pixels that are defect showing either no signal at all (dead pixels) or experiencing count rates that are not linear to the actual flux (hot pixels). Most bad pixels are clustered in groups.

Areas of Increased Dark Current: Some areas on the detector show an increased dark current (warm pixels), which is most evident in the encircled region in Fig. 5.1. The difference to the above hot pixels is a linear behavior with integration time.

These three items are true detector properties which cannot be changed in any way. They can be effectively corrected and do not pose a principal problem for the detector calibration.
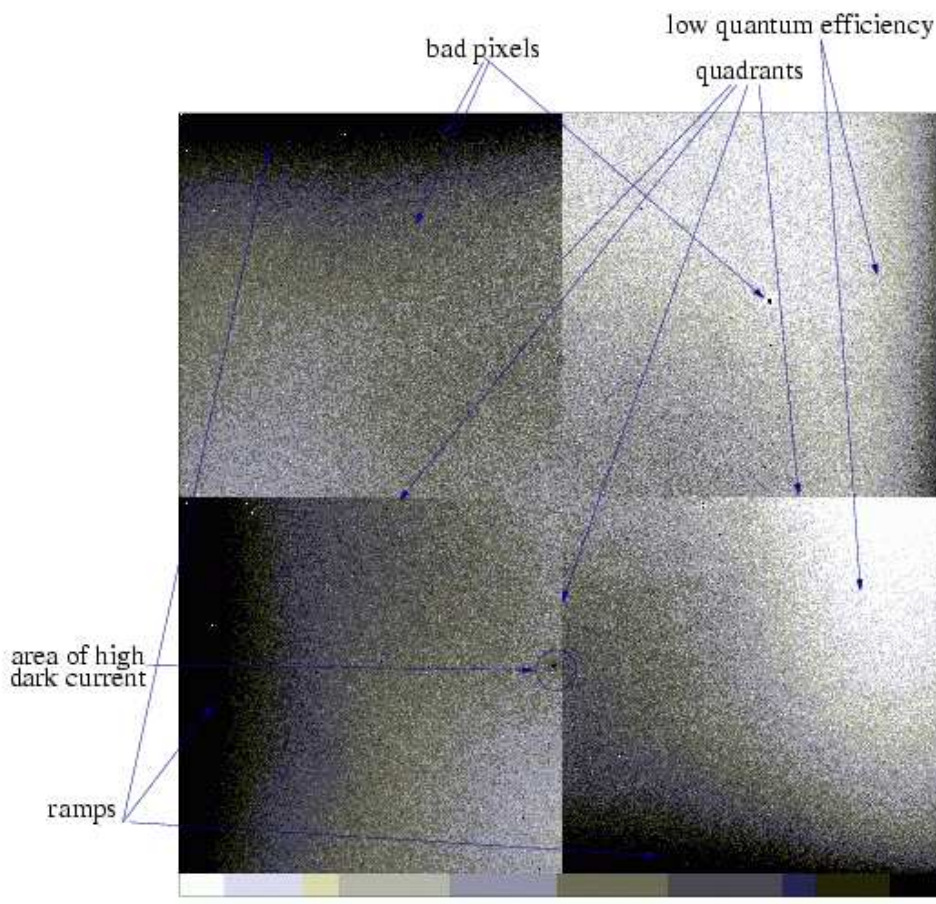
Figure 5.1:   Raw OMEGA2000 image. The detector imperfections are labelled.

The next three items, however, are not inherent to the detector. The features are probably caused by the readout process (quadrants & ramps) or by external noise sources (stripes) and occurred — with modifications — throughout the commissioning time . These unwanted features are not to correct since they may be varying in time and in different readout modes. Therefore, the elimination, or at least minimization, of these effects has the highest priority for the next commissioning in order to avoid a loss in sensitivity due to additional noise sources. The pipeline reduction system presented in this chapter cannot account for these anomalous imperfections.

Quadrant structure: The four electronically independent quadrants are clearly distinguishable. The count levels show systematic offsets where the quadrants meet.

Ramps: Each quadrant exhibits a gradient ramp of increased counts on one side.

Stripes: Different stripe patterns are visible at high count resolutions, which are not evident in the representation of Fig. 5.1.

Due to the detector imperfections listed above, the high noise level of the total background, and the short integration times in NIR observations, most astronomical objects are not visible in the raw images. Unless IR-bright sources are in the field of view, it is already difficult to tell which patch of the sky is being observed. With just raw images available, the observer is basically "blind" without a means of quality assessment of the data. The availability of processed images in almost real-time thus offers important advantages: the pointing position can be verified accurately, the image quality and instrument performance can be assessed, and the intended limiting magnitude can be checked. With this information at hand, the observer can quickly react to the given conditions and make immediate adjustments to the observation program.

The large data volumes acquired with infrared observations — typically several hundred images per night — are another important reason for the development of an automated data reduction software that can process these loads efficiently.

For the reasons mentioned above, a pipeline — meaning an automated data reduction software with minimal user interaction required — is an important and convenient tool for infrared observations. To be of optimal use for ongoing observations, the OMEGA2000 pipeline has to fulfill certain specifications that result from the considerations above. Thus, the pipeline should:

- contain all standard IR reduction steps, namely calibration, sky modelling, and summation of dithered images.

- run without any user interaction once started.

- fully reduce an image within the typical data frame rate of one new image every 30 seconds.

- allow online-reduction, which means data processing in the background, as soon as a new frame was written to disk.

- be informed about the latest images and their belonging to a specific pointing.

- yield about 80–90% of the best possible reduction with a standard non-customized call.

- allow different sky modelling schemes for various applications.

- allow user specification of important parameters for a customized application after the observing run.

With these specifications, the pipeline can be used as a standard online reduction tool at the telescope and as a fast and efficient way to do customized offline data reprocessing at a later stage with optimized parameters and selected input images.

5.2   Overview

This section will provide a general view on the standard infrared reduction procedure, the overall pipeline structure as it is implemented, and the online reduction scheme.

5.2.1   General reduction scheme

The standard IR image reduction process involves several steps from the raw frame to the reduced image, which contains the calibrated astronomical signals. A more detailed discussion of IR data reduction can be found in Joyce (1992).

The reduction process can be subdivided into three parts: detector calibration, sky modelling and subtraction, and summation of dithered images to a final frame. The different steps will be discussed briefly:

Calibration

The purpose of the calibration steps is the correction of the main detector imperfections presented in Sect. 5.1. After the following three reduction processes the image should be flat and devoid of defective areas.

Dark Current Subtraction: Due to the low detector operation temperature of $77\,K$, thermal excitation of electrons should be negligible (see Tab. 3.2). Some regions, however, show an increased dark current as was depicted in Fig. 5.1. These regions can be identified from images taken with a blank cover at different integration time settings. Pixels with count rates well above the average value but with a linear temporal behavior are saved in a designated *dark current frame*, which stores the thermal electrons per second for each warm pixel. This frame can then be scaled to the real integration time and be subtracted from the science image.

Flatfielding: By dividing the science image through a normalized flatfield image, the sensitivity variations across the detector are corrected. The flatfield contains two components: the fixed pattern noise (FPN), caused by pixel voltage variations and measured as discussed in Sect. 4.2.3, and the global quantum efficiency variations, determined most accurately by differential measurement of a designated star at many detector positions.

Bad Pixel Correction: Bad pixels contain count levels that are by definition not well related to the incident signal. Therefore, the bad pixel values have to be replaced by a representative count level determined from good pixels in the local neighborhood. The defect pixels are marked in a *bad pixel mask* by a value 1, whereas the position of good pixels is indicated by 0.

The corrections above require appropriate calibration frames for the detector in use. The dark current frame and the bad pixel mask are valid for all observations, the flatfields, however, need to be determined for all relevant filters individually.

A bias subtraction, as necessary for the CCD calibration, is in general not needed for IR images taken with a double-correlated readout mode. Any constant offset voltages are automatically eliminated in the double-frame-correlation process as was discussed in Sect. 3.3.

After the detector imperfections have been corrected, all pixel count levels are now, in the ideal case, proportional to the incident total flux.

Sky modelling

The high background from the environment and the sky, with an additional temporal and spatial variability of the latter, give rise to the main differences of near-infrared observing and reduction techniques compared to optical observations. The uncertainties of the IR sky can in fact be a lot larger than the actual astronomical signal. An accurate modelling of the local and current sky contribution to the total signal is therefore the essential task in the IR reduction process. The quality of the modelled sky will — in most cases — determine the sensitivity limit of the observations.

As was shortly discussed in Sect. 4.2.2 on observing utilities, there are basically two approaches for obtaining the sky signal that can then be subtracted from the science images.

The most straightforward way to obtain the background signal is the observation of a designated sky area in the neighborhood of the astronomical object to be studied. These images[1] can be subtracted from the object frame to obtain a clean image. This technique is still the best method for the observation of very extended objects. The drawbacks, however, are the increased observing time and a poor spatial correlation to the local sky in the science frame.

For sparse fields with mostly sky signal reaching the detector (see Sect. 4.2.2), the background contribution can be extracted directly from the science frames. Thus, no observational time is lost and the sky contribution can be determined with the best spatial and temporal correlation possible.

The principle of the sky extraction is the following: Several dithered images are stacked in the pixel coordinate system, *i.e.*, the values in the third dimension of the image cube all result from the same detector pixel. Due to the small telescope offsets in between the image sequence (Sect. 4.2.2), the astronomical objects are slightly shifted from image to image. Thus, the pixel columns — the values for the same pixel in the different images — contain mostly sky signals even at the position of a stellar object in one image. A suitable value for the actual sky level in such a pixel column is the median. The median is a less sensitive function concerning outliers than the average and is thus less influenced by a high star signal. An accurate sky frame is obtained by determining the median for each pixel column of the image.

Besides a real median process, other techniques can be applied to extract the best local sky value for a pixel, as will be discussed in Sect. 5.3.1. However, the principle of stacking several dithered frames and determining the sky from the pixel columns is the same for all methods.

---

[1]For high quality images, the sky images themselves need to be processed, *e.g.*, for the removal of all stars.

Shift and align

After the background contribution has been removed and the individual image is fully reduced, all frames belonging to the same pointing have to be added up in order to create a master image with an improved signal-to-noise ratio. When summing N images with a given SNR of an object, the signal-to-noise ratio of the superimposed frame will be improved by a factor $\sqrt{N}$, as can be seen from Equ. 4.1. For the detection of very faint objects, a large number of images has to be co-added in order to reach a sufficiently high SNR.

Since the images were taken at slightly different positions, shifted by the dithering offsets, they have to be aligned prior to the summation. The alignment takes place in the world coordinate system, which means that the individual objects are placed at the same position in the summed frame. The approximate offsets can be calculated from the observing position stored in the image header or directly from the known dither pattern used. For high quality images, the alignment precision should be on a sub-pixel scale, which is beyond the pointing accuracy of the telescope. The exact shifts of the images can be obtained by matching the positions of corresponding point sources in the frames. Once the offsets are known, the frames can be superimposed to the master sum frame in different ways. Well sampled images can just be summed with integer pixel shifts, whereas in the under-sampled case a more elaborate summation process, *e.g.*, the DRIZZLE[2] algorithm for the PSF reconstruction, might be more appropriate. The latter method is not part of the pipeline system and will not be described here.

The summation process also offers the possibility to effectively eliminate cosmic ray events in the data. Since cosmics usually affect individual pixels and are statistically distributed in the different images, they can be removed by filtering high pixel count levels that are detected in a single frame only.

5.2.2   Pipeline at a glance

Framework

The OMEGA2000 reduction pipeline was developed as a C-application program within the MIDAS environment. Application program in this context means that MIDAS interface functions are used to connect to and manipulate the different data objects such as images, descriptors, and catalogs. A C-application program offers the advantages of greater flexibility and — even more important — faster computation than the predefined high level MIDAS functions.

The pipeline was mainly developed and optimized for survey applications in the normal observation mode (see Sect. 4.2.2). Thus, the sky modelling from the science frames is an integral and central part of the pipeline reduction process. However, observations of extended objects with intermediate designated sky pointings can also be handled by the pipeline with a somewhat decreased reduction quality. The general conditions for a versatile and useful data reduction pipeline were already discussed in Sect. 5.1.

---

[2]For details see Mutchler, M. & Fruchter, A. (1997) and Fruchter, A.S. & Hook, R.N. (2002)

Parameter	Default	Description
image catalog	current observ.	contains all images to be reduced
sky mode	median mode	median, minimum, or $\kappa\sigma$-clipping mode
		used for the sky modelling process
sky frames	7	total number of frames for the sky modelling
cosmics filtering	5 , 5	Nºframes from which reference frame is
		constructed, cosmics cutoff in units of
		standard deviations above median level
action flag	all	single image reduction, summation, or both
sum save flag	every n^{th}	write out sum image after every n summations,
		save only final sum, save also direct sum
		including cosmics
calibration flag	at beginning	do flatfield correction at beginning, end,
		or do not use any calibration frames at all
calibration frames	standard frames	names of flatfield frame, bad pixel mask,
		and dark current frame
sky save flag	no saving	save modelled sky or not
screen output	yes	display current pipeline status on screen or not
cuts	-3 , 10	low and high cuts for images in units of
		standard deviations above median level

Table 5.1: Pipeline command line parameters.

Structure

The OMEGA2000 image reduction pipeline was designed in a modular structure in order to facilitate a later refinement and extension of the software. Table 5.2 lists the different modules with a brief description of their function. The total pipeline consists of 27 parts that can be grouped into the calling function, header files, and the actual C-modules.

The reduction software is started by calling the MIDAS procedure *OMEGA_pipeline.prg*. Once the pipeline is activated, no further user interaction is required until the reduction is finished. The task of the top-level procedure is mainly the handling of input parameters and invoking the actual C-application program. Some of the most important command line parameters are listed in Tab. 5.1. The key information for the pipeline is the name of the image catalog containing all frames to be reduced. The majority of the input specifications govern the sky determination and summation processes. The meaning of these parameters will become clearer in Sect. 5.3, where a more detailed discussion of these parts is given. The third main parameter set for the pipeline is the specification of the calibration frames.

Besides the external command line input options that define the current reduction mode, the pipeline requires an additional set of about 30 internal parameters. These symbolic constants are stored in two header files and group into detector characteristics

and pipeline operation parameters. Detector related constants are, *e.g.*, the number of pixels per axis and the pixel scale. Pipeline operation parameters include the size and location of a sub frame for the statistics determination, normalization levels, and the allowed ranges of the command line inputs. About a dozen symbolic constants govern the detection and analysis of objects for the frame offset determination in the summation process. These internal parameters are to be optimized for the general operation and are not intended to be tunable by normal pipeline users. A well adjusted and predetermined set of internal constants will allow an easier and more secure use of the pipeline for general users and should yield optimized reduction results for most applications.

The overall structure and operation scheme of the OMEGA2000 reduction pipeline is illustrated in Fig. 5.2. The diagram visualizes the main pipeline components and their interactions for a standard reduction in a simplified way. All pipeline input is indicated by yellow boxes, all output by green ones. The input parameters are passed on to the MIDAS procedure *OMEGA_pipeline.prg*, which in turn calls the main C-module. The main function handles all pipeline input and output and organizes the specified reduction mode. Once all input parameters have been imported and the calibration frames have been opened, the actual reduction starts with the image loop. After this point, the pipeline is an interplay of the main function, the modules which perform the individual reduction steps, and the image stacks where the data and intermediate results are stored and manipulated.

Image loop

The image loop successively processes all raw data input frames specified in the input image catalog. It can be subdivided into the single image reduction and the summation process part, which are independent units that can be run separately. Once the next entry from the image catalog is read in, an output frame for the reduced data is created. This frame is initialized with the raw input data that is dark current subtracted and flatfield divided in the same process to minimize the computational effort. The next reduction step is the bad pixel correction, which replaces defective pixel values by an appropriate count level determined in the local neighborhood. The bad pixel mask contains the information which detector areas have to be corrected, as was discussed in Sect. 5.2.1. Once a defective pixel is found, the function looks for the nearest good values in all four directions. By using linear interpolation between the good pixels to the left and right, and between the up and down values, appropriate intermediate count levels at the position of the defective element are found. The original bad pixel value is then replaced by the average of the two interpolations in between the four closest good pixels. The data has now been corrected for the detector imperfections and is ready for further processing.

The next and most important block for the single image reduction is dedicated to the sky modelling process. A more detailed discussion of this component will be given in Sect. 5.3.1. Before the sky contribution can be extracted, basic statistical properties of the current data have to be determined. The statistics module uses a predefined sub frame of a typical size of 200×200 pixels to compute the mean, standard deviation, and median of the data values. The so determined median value is an accurate measure of the typical

background contribution — always assuming a sparse object coverage in the field — which will be a conserved quantity for the outcome of all subsequent data manipulations. This approach retains the global statistical properties of the original data as much as possible, *i.e.*, the flux-to-background ratios and the validity of the Poisson statistics are preserved in first order. The task of the sky modelling process is thus a smoothing and flattening of the sky background variations in order to reduce the background uncertainties as much as possible, while conserving the overall detected count level properties of the original raw image. Once the sky for a certain input frame has been modelled from a set of science images that are temporally correlated — the details will be discussed in the next main section — the background can be subtracted and replaced by a constant representing the original median sky level. The single image reduction for the sky corrected frame is now finished and the cleaned data is saved on disk.

In a typical pipeline application, the reduced single frames will be further processed by the second unit, the image summation. The details of this part will also be given in the next main section. The task of this last pipeline component is the alignment and summation of the dithered images and the removal of cosmic ray events in the data. An incoming reduced single frame is first analyzed by several preparation modules. This preparation includes the determination of the accurate frame offsets compared to a designated master image by object detection and the data storage in an auxiliary image stack for subsequent cosmics removal. The actual summation and cosmic ray cleaning takes place every time the image stack is fully loaded. The final result of the summation process will be the aligned and cosmics cleaned superposition of all images specified in the input catalog. Intermediate summation results can be optionally saved on disk which will be a useful tool for the assessment of real-time reduced data.

After an image has been fully processed and passed through the whole image loop, the pipeline continues at the beginning of the loop with the opening of the next raw input image. The image loop will be repeated until the last data frame of the input catalog has been reduced. At the end, the pipeline will save the specified final summation frames and return to the calling MIDAS session. All images of the input catalog have now been reduced and summed up automatically without any user interaction required.

5.2.3 Online reduction scheme

To be able to process data in almost real-time during ongoing observations, the reduction pipeline needs to stay updated on the latest images. The general online reduction scheme for OMEGA2000 data and the interactions of the different components are schematically illustrated in Fig. 5.3.

The fastest data quality control can be achieved by running three different MIDAS sessions simultaneously. The first session handles the data acquisition, the second the image reduction, and the third one can be used for an interactive analysis of the reduced images. The conclusions from this analysis can in turn be used to feedback and optimize the acquisition process (see Fig. 5.3).

In the first MIDAS session, an observing macro, as presented in Sect. 4.2.2, coordinates the telescope movements and the instrument commands. The integrated OMEGA2000 images are saved on disk in a raw data directory. In addition, the observing utility creates an image catalog for all frames taken with the current macro call. This image catalog is updated with the name and directory path of the latest image once it is saved on disk. The name of the active image catalog and the integration time of the current observations are written to a file, which can be accessed by the pipeline.

When starting the reduction pipeline in online-mode in the second MIDAS session, these auxiliary files are opened and read. This way, the pipeline is informed about the currently active image catalog and the reduction can start. The data files are read in from the raw data directory, where they remain unchanged. To facilitate the file organization, the reduced output images are stored in a different data directory from which the pipeline was called. With the appropriate summation parameter set, the updated master sum is written to disk every time after a specified number of frames. This way, the observer has immediate access to the sum of all images currently available and can assess the depth and limiting magnitude of the pointing. Once all newly available frames are processed, the pipeline waits for the next image to come in. The online reduction is closed down if no new input frame is received within a given waiting period.

The reduced individual frames and the summed images can be accessed from the third MIDAS session. Interactive measurements can then be conducted and the image quality assessed. If a change in the observing strategy proves to be necessary after the analysis, the observer can react to the given conditions within a few minutes after the data was taken.

Mod.	Name	CP	Short Description
I	OMEGA_pipeline.prg	6	MIDAS calling function; parameter handling
i	O2000_para.h	1	detector related parameters
ii	pipe_para.h	2	pipeline related parameters
iii	struct_def.h	3	C-structure definitions
1	OMEGA_pipeline.c	28	main module; setup, image i/o, function calling
2	flat_correction.c	4	flatfield correction & dark current subtraction
3	copy_frame.c	2	do frame copying if flatfield correction is omitted
4	badpixel_correction.c	4	bad pixel correction by interpolation
5	subframe_statistics.c	5	computes fundamental statistics in sub-frame
6	extract_name.c	2	makes up new output names
7	normalize_frame.c	2	frame normalization before sky determination
8	load_stack	3	puts new frame on image stack
9	get_sky.c	4	sky determination by taking a fast median
10	minimum_sky.c	5	sky determination by taking mean of smallest values
11	sky_clipping.c	4	sky determination by using $\kappa\sigma$-clipping
12	save_sky.c	2	writes out sky image
13	subtract_sky.c	3	subtract modelled sky from image
14	original_level.c	2	sets image back to original count level
15	frame_info.c	2	get relevant information on frame for summation
16	sum_preparation.c	3	prepare summation process and cosmics filtering
17	find_object.c	14	find objects and determine x-, y-move for summation
18	make_cleansum.c	4	compute median reference frame for cosmics filtering
19	elaborate_sum.c	6	elaborate summation with cosmics removal
20	dirty_sum.c	3	straight summation without cosmics filtering
21	put_tosum.c	3	sum up several cosmics-filtered images
22	save_dirty.c	2	write out straight sum
23	cut_frame.c	3	cut out summed image
27		122	

Table 5.2: Pipeline components. *Mod.* is the module number, *CP* (Code Pages) gives the number of source code pages. The values in the last line indicate the total number of modules and the number of code pages.
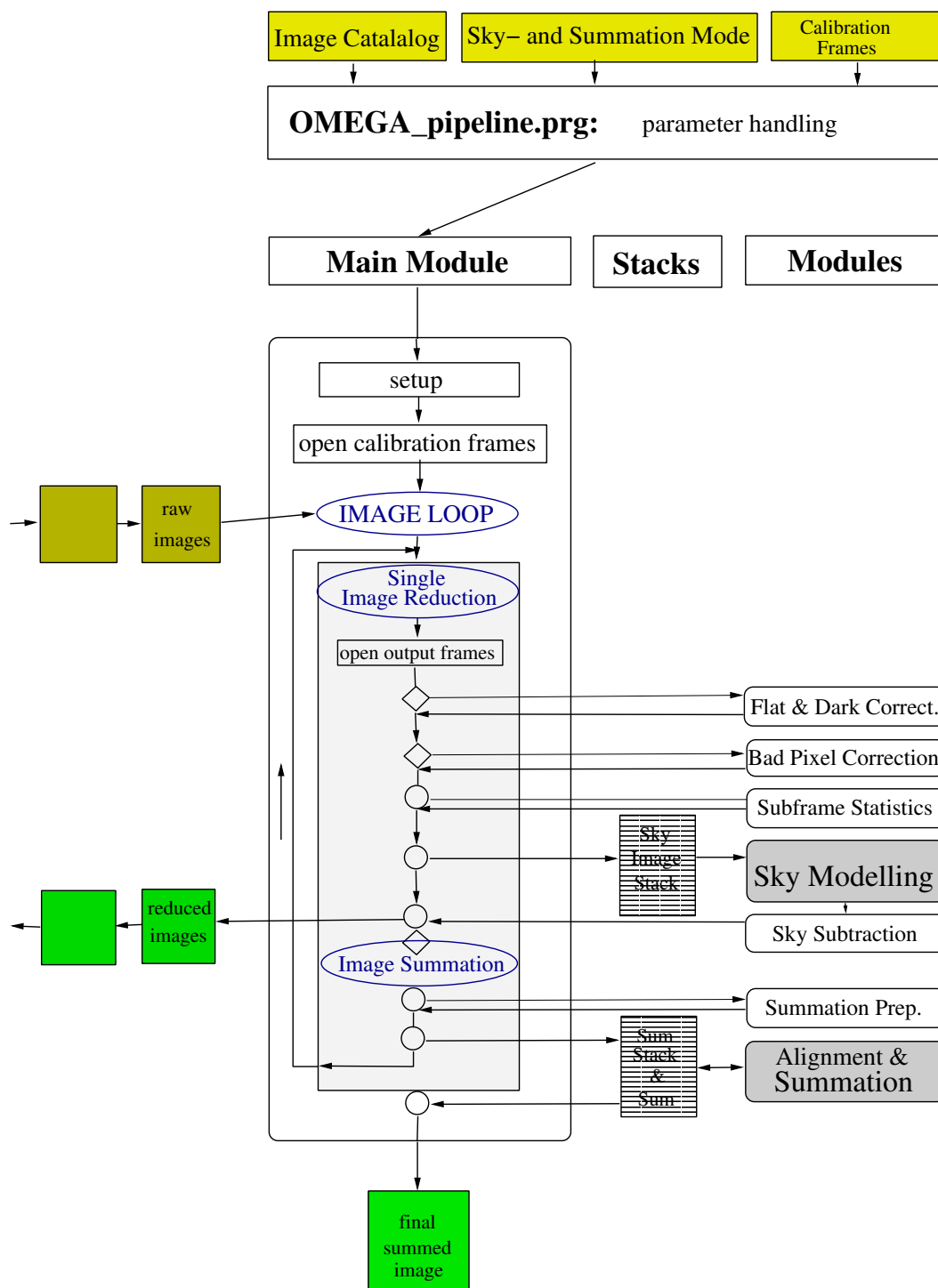
Figure 5.2: Overall pipeline structure. The pipeline input is indicated by yellow symbols, the output by green symbols. Module calls that can be suppressed by input parameters are indicated by squares, calls that are an integral part in every pipeline reduction by a circle. The column *stacks* contains some of the auxiliary image storage arrays, in which most of the pixel manipulations take place.
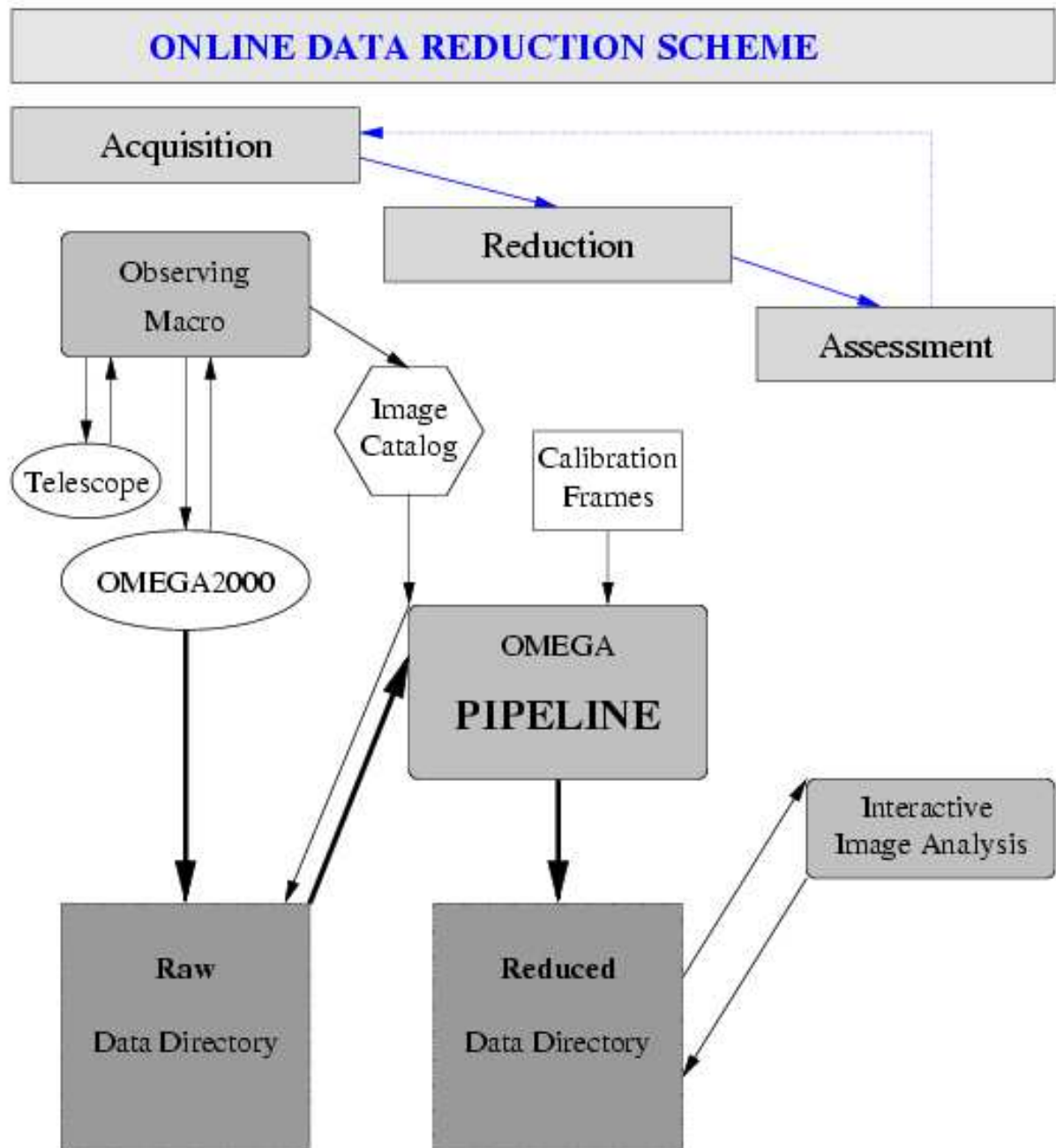
Figure 5.3: Online reduction scheme.

5.3   Main Components

After the general overview over the reduction schemes and the pipeline structure, this section will focus on a closeup look on the two main components concerning the sky modelling and the summation process.

The detector calibration steps, as the first part of the reduction process, are straightforward and need no further remarks beyond the discussion in Sect. 5.2.1 & 5.2.2. In contrast to the following components, the results of the detector corrections are mainly dependent on the quality of the input calibration frames for the dark current subtraction, the flatfield division, and the bad pixel correction. A high quality removal of detector imperfections is thus only possible with carefully measured and optimized calibration frames and is fairly independent on the actual implemented algorithms.

5.3.1   Sky modelling

The principal procedure for the sky determination was already discussed in Sect. 5.2.1. In this section, the actual pipeline implementation for the whole process and the different sky modes with their applications will be discussed.

General

Two important command line input parameters have to be specified for the modelling process (see Tab. 5.1): the sky mode and the number of frames used for the background extraction. The sky mode can be chosen from the three implemented options discussed below and depends on the pipeline application. The number of sky frames defines how many images are used for the modelling process and can be put on the sky stack at a time. Since the corresponding science image is always the chronologically intermediate image on the stack, the parameter has to be optimized for good temporal correlation, meaning few images before and after, and small variance in the median determination, favoring many frames.

The implemented sky modelling process for the pipeline is illustrated in Fig. 5.4. The data frames entering the sky modelling block are already corrected for the detector imperfections and have a descriptor containing the fundamental statistical properties of the image (see Fig. 5.2). To account for systematic changes in the median background level over time, the input data has to be normalized to a given constant median level. For this reason, all pixel values are multiplied by a constant frame factor that scales the median frame value to the normalization level. The normalized data is copied into the image stack replacing the oldest frame there. When the sky image stack is fully loaded, it contains the specified number — in the illustrated example 7 — of dithered and normalized images. The dithering offsets are depicted by the "stellar object" in the images that is located at different positions in the frames. The master image for which the sky is modelled is emphasized by darker color in the intermediate position. The background is extracted from the master frame and the three exposures taken prior to and after the reference image.
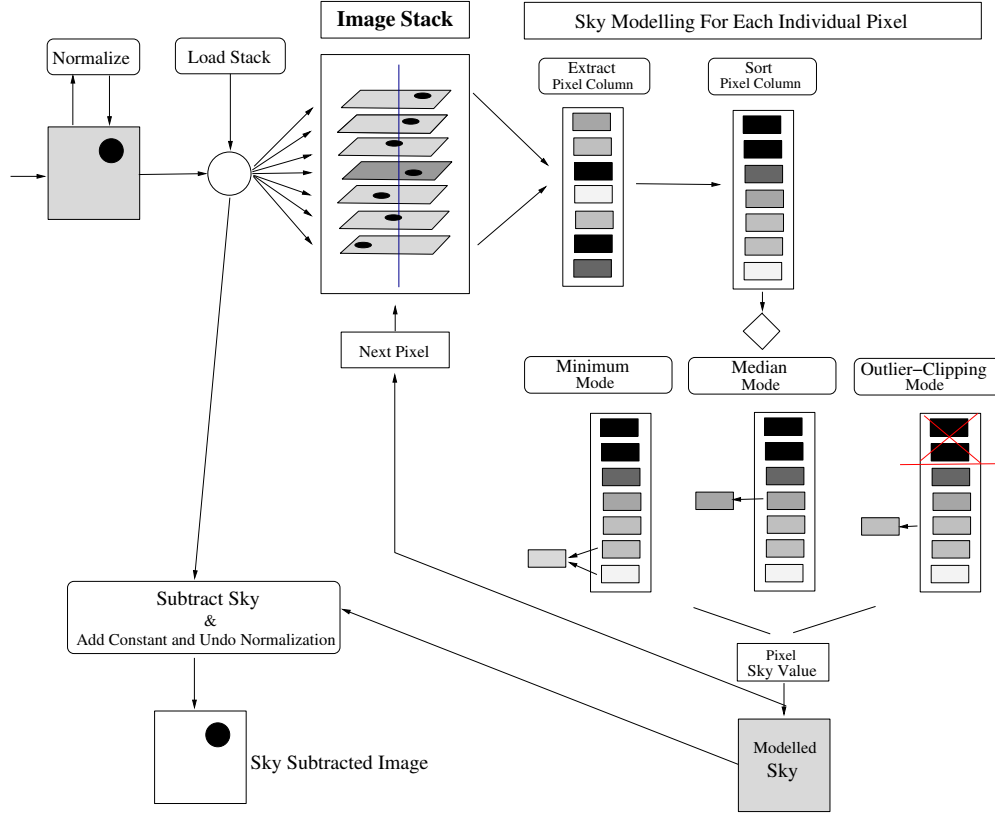
Figure 5.4: Sky modelling process. Incoming images are normalized and loaded onto the image stack. The sky value for a sorted pixel column is determined according to the specified mode and saved in an auxiliary sky array. This sky frame is subtracted from the science image, an appropriate constant added, and the normalization undone. The sky selection process of the different modes is schematically illustrated for a single pixel. The filled black circle on the different images represents the same stellar object that is shifted due to the dithering. Different grey scales in the pixel columns stand for different count levels, with black being the highest.

The actual sky modelling is done for each pixel individually. First, a pixel column is extracted. This auxiliary vector contains the values for the concerning pixel taken from all frames on the stack. Different count levels in the pixel column are symbolized by different grey scales in Fig. 5.4, where black stands for stellar flux values and grey for a true background measurement. The pixel column is then — in principle — sorted and rearranged to be in ascending order. Sorting is not always necessary as will be discussed below, but it better illustrates the difference of the sky modes depicted in Fig. 5.4. According to the mode in use, a dedicated sky value is determined from the pixel value and stored in an auxiliary sky array. This whole process is repeated for all pixels resulting in the modelled sky for the master frame. If specified by the appropriate input parameter, the sky model can be saved on disk.

The so determined total background can now be subtracted from the science frame. In order to preserve the original count level ratios, as was discussed in Sect. 5.2.2, a constant representing the median sky level is added to all pixels and the original frame level is restored by dividing through the former normalization factor. The final outcome is a sky subtracted master frame.

After the sky determination and subtraction is finished for the master image, the next normalized frame is loaded onto the stack in the position of the oldest data array. The modelling process can then start for the next designated master frame.

The first and last images of the input catalog require a slightly different treatment, since they are not embraced by enough frames taken prior to or after the actual exposure. In this case, the unavailable images are substituted by frames taken with opposite temporal offsets, *e.g.*, the sky for the first four exposures in the catalog are all determined from the first seven images.

The sky modelling with the above described procedure takes by far the most computational effort in the whole pipeline reduction. For a single background determination of an OMEGA2000 image, more than 4 million medians or minima have to be calculated. In order to minimize the total pipeline reduction time, the algorithms for the sky modelling have to be very efficient and speed optimized. This has been accounted for in the design of the different sky modes that are now discussed.

Fast median method

The implemented median method for the background determination is the fastest of the three available sky modes. It extracts the sky in roughly half the time of the other two modes and is thus mainly foreseen as the standard online reduction mode for normal observations.

The fast median method is extracting the real median, *i.e.*, the intermediate value of the sorted pixel column, as the sky level (see Fig. 5.4). The algorithm for this mode differs from the other methods in two essential ways. Firstly, the median is extracted from the pixel column without sorting it. This can be achieved with a fast algorithm[3] that selects the nth largest element from an array while leaving the remaining elements in arbitrary order. It can be shown that the operation count for this method scales only linear with the number of elements in the vector (Press *et al.*, 1992). The second difference concerns the number of median recalculations. Since from one sky determination to the next only one old value of each pixel column is replaced by a new one, the number of median calculations can be substantially reduced by comparing the new value with the replaced count level that was saved in a designated array. If the new and old value are both either larger or smaller than the last determined sky level, the median of the new pixel column remains unchanged and the old sky value is still valid. If the new value is smaller and the old one larger than the last sky value (or vice versa), the median level has changed and needs to be recalculated. Simple considerations show that the median has to be redetermined, on average, for only

---

[3]The implemented algorithm is called *SELECT()* and can be found in Press *et al.* (1992).

the fraction $(N+1)/2N$ of all pixels, with N being the number of images on the stack. For $N=7$ as in the example, this amounts to an average recalculation percentage of 57%. This implies that in more than 40% of all pixels the median determination can be omitted, with the effect of saving a substantial amount of computational effort.

The fast median method does not yield the qualitatively best sky possible, since it treats star flux just the same as the background, which results in a small bias toward systematic higher sky values at the position of stellar objects in any of the images on the stack. Because of its superior speed, the median mode can be useful for all quick-look applications, in particular the real-time data reduction.

The performance of the different sky modes will be discussed in Sect. 5.4.

Minimum Method

The minimum sky mode is designed for the background determination in crowded fields and for large extended objects. If most pixels contain object flux on top of the background, the median of the pixel column is not an appropriate sky value any more. The minimum method requires an additional input parameter that specifies how many of the smallest values of the sorted pixel column should be averaged for the sky level. In Fig. 5.4 this parameter is set to two, *i.e.*, to the mean of the two smallest count levels.

If the true minimum is to be taken, *i.e.*, the average parameter is one, an efficient and fast algorithm similar to the one described above is implemented. For larger average parameters, each pixel column has to be sorted[4] first before the mean of the smallest values is determined.

The minimum mode can also be used for the online reduction of data taken with the extended object observing utility (see Sect. 4.2.2). Since sky and object observations alternate, there will always be at least three dedicated sky observations loaded in the image stack, if the total number of stack images is again seven, as in Fig. 5.4. By averaging the smallest three values in each pixel column, a fairly well determined sky value should be obtained for the majority of the pixels.

Outlier-clipping method

The most elaborate implemented sky modelling method for normal observations is the outlier-clipping mode, also known as $\kappa\sigma$-clipping. This method makes use of the fact that outliers, *i.e.*, count levels that differ significantly from the average sky background value, are always biased toward higher levels since the flux of astronomical objects is always added to the background. The outlier-clipping mode identifies stellar flux contributions and excludes them from the sky determination process. This way, the sky is only determined from designated background values. Particularly at the position of astronomical objects in any of the stacked images, the modelled sky will show a significant improvement compared to the median method.

---

[4]The used sorting function is called *SHELL()* and can also be found in Press *et al.* (1992). This algorithm is very efficient for small vectors to be sorted.

The outlier-clipping mode requires an additional user specified input parameter κ defining the cutoff above which count levels are classified as object flux. The κ-parameter is to be given in units of the standard deviation σ above a typical background level.

Two questions arise immediately from this consideration: What is the typical background level and what is its standard deviation σ? As starting point for the algorithm, the extracted pixel column of N values is sorted[5] in ascending order, as is schematically illustrated in Fig. 5.4 for $N = 7$. Under the assumption of a sparse field without large extended objects, only few values per pixel column should contain flux contributions from astronomical objects. This implies that the mathematical median of a pixel column is in general a good first order approximation for the sky level, that may be slightly biased toward higher values if outliers are present. In other words, the sky determination with the above median mode serves as first order reference for the outlier mode. With the determined typical background level n_{sky} for a pixel column, the standard deviation σ_{sky} can be calculated using Poisson statistics. The pure statistical uncertainty for an average background of n_e detected electrons in a pixel is given by $\sigma_e = \pm\sqrt{n_e}$ electrons. In order to determine the statistical error σ_{sky} of the normalized reference sky level in the pixel column, the counts have to be converted back to the number of physical electrons detected. This conversion depends on the used normalization factor f_{norm} and the gain g [electrons/count], which is the proportionality constant between counts and detected electrons. Because of the inhomogeneous quantum efficiency (QE) across the detector, an additional local correction factor QE_{ij} has to be applied to account for unsensitive detector regions. Since the detector quantum efficiency variations are measured in the global flatfield, this input frame can also serve as a local sensitivity map. Putting all conversion factors together yields a local statistical uncertainty $(\sigma_{sky})_{ij}$ at the pixel coordinates ij in normalized count units of

$$(\sigma_{sky})_{ij} = \sqrt{\frac{n_{sky} \cdot f_{norm}}{g \cdot QE_{ij}}} \,. \tag{5.1}$$

With this standard deviation, the local cutoff level CUT_{ij} can be determined as

$$CUT_{ij} = n_{sky} + \kappa \cdot (\sigma_{sky})_{ij} \,. \tag{5.2}$$

With the local cutoff level CUT_{ij} calculated, the sorted pixel column can be checked for pixels with a significant object flux contribution. Count levels above the cutoff are excluded from the background determination. The refined sky level for the specific pixel is given by the median value of the background levels that passed the outlier clipping (see Fig. 5.4).

The outlier-clipping mode yields the best sky model for normal sparse field observations, at the expense of an increased computing time. This sky mode is thus the appropriate modelling method for a high quality reduction. However, the implemented $\kappa\sigma$-clipping algorithm only allows the exclusion of values above the median, i.e., only maximal $(N-1)/2$ values may be clipped. For the example with $N = 7$, at most 3 outliers can be excluded. This implies that for objects larger than the typical dithering offsets (see Sect. 4.2.2) the

---

[5]The sorting function is again *SHELL()* found in Press *et al.* (1992)

reference median represents already a level with an object flux contribution. The modelled sky around these objects will thus be biased towards higher values, which will result in an overcorrection. For data containing large extended objects and reduced with the outlier-clipping mode, it can be expected that the local neighborhood of these objects exhibits a systematic bias to lower count levels.

Standard reductions

Since the sky modelling method used in the reduction has the major influence on the quality of the results and the total processing time required, it primarily defines the input parameter choice for the different applications. Table 5.3 lists four standard pipeline applications with an appropriate set of sky modelling parameters.

RM	Application	Sky Mode	Frames	Comment
1	**online reduction for normal observations**	fast median	5	fast but reduced quality
2	**online reduction for extended objects**	minimum with $n_{ave}=1$	5	fast but reduced quality
3	**high quality reduction for normal observations**	$\kappa\,\sigma$-clipping with $\kappa=3$	7 or 9	slower but best quality
4	**improved reduction for extended objects**	minimum with $n_{ave}=3$	7 or 9	slower but better quality

Table 5.3: Standard reduction modes (RM) for different pipeline applications. The different sky modes were described in the last section, where κ specifies the outlier-clipping cutoff and n_{ave} the number of the smallest values that are averaged. *Frames* defines the total number of images used for the sky modelling.

5.3.2 Summation process

The principal steps of the summation process were described in Sect. 5.2.1. This section will focus on the implemented algorithms used for the pixel offset determination, the cosmics removal, and the summation process.

General procedure and cosmics filtering

The OMEGA2000 pipeline summation process is designed to superimpose reduced single images with the best possible integer pixel shift. An alignment with integer pixel offsets will allow a fast summation and requires the least data manipulation. The simple superposition of whole frames is only possible because of OMEGA2000's excellent image quality with a distortion of less than one pixel from center to corner. Besides an optimized alignment, the
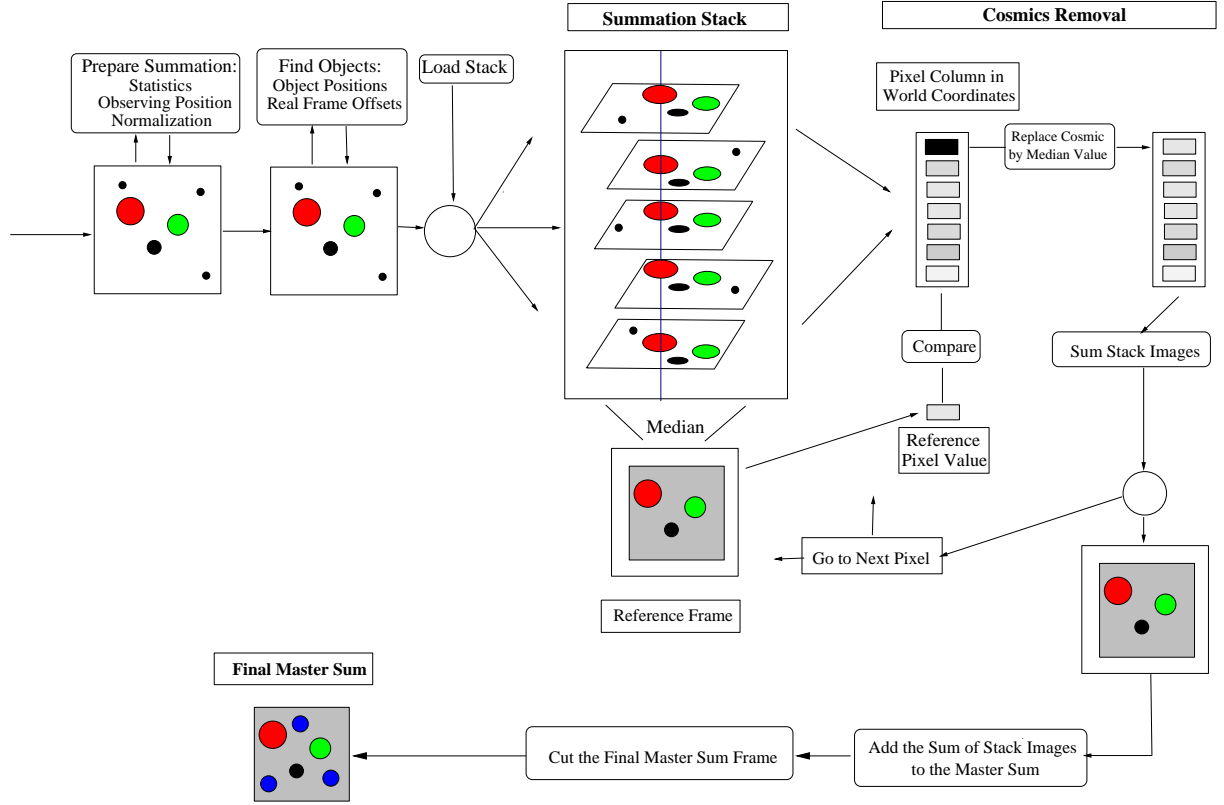
Figure 5.5:   Summation process. An incoming reduced frame (upper left) is prepared for the summation and loaded onto the image stack. The objects — symbolized by large circles — are aligned, whereas cosmics (small black dots) are statistically distributed. The median of all stack images yields the reference frame, which is in turn used to identify and remove cosmic ray events from the data. The cleaned values are added and saved in an auxiliary array. When this process is finished for all pixels, the result is added to the master sum which is cut out and saved to disk after all input images have been superimposed.

second objective of the summation process is the complete removal of cosmic ray events while leaving the flux of astronomical objects untouched.

As can be seen in Tab. 5.1, the summation process is basically governed by three user specified input parameters: the number of images N_{sum} for the summation stack, the cutoff parameter κ_{sum} for the cosmics filtering process, and the number and content of the resulting summation frames written to disk. The meaning of the first two parameters will become clearer in the discussion below. The third parameter defines the determination of additional summation frames besides the cosmics cleaned superposition of all images. For real-time online reductions, intermediate summation results can be saved on disk to allow direct assessment of the data quality. For pipeline quality checks and other applications, the real sum — including all cosmic ray events — and the difference of the real and cleaned sum is optionally determined.

The principal steps for achieving the cosmics cleaned superposition of all images in the input catalog is illustrated in Fig. 5.5. A reduced image containing astronomical objects and cosmic ray events is entering the summation block in the upper left corner of Fig. 5.5. Cosmics are depicted by small black circles in the image, while real objects are symbolized by the group of larger circles. In a first preparation step, the statistical properties and the observing position of the incoming frame are read in from the concerning image descriptors. If the observing position belongs to the same dither pattern as the master frame — which is the first image of the catalog — the expected pixel offsets for the alignment are determined; otherwise, the observing position is not in the vicinity of the master frame and the image is rejected from the summation process. Next, the non-rejected frame has to be normalized to scale the median count level to a given constant. This again accounts for possible background variations, as was already discussed in the last section. The following module searches for all objects of a reference list at the approximated frame position. The object detection and analysis will be discussed below in more detail. From the positions of the found and matched stellar objects, the actual frame offsets in the x- and y-direction compared to the master frame can be determined. The image is loaded to the summation stack which can hold the specified number of frames. The images on the stack are aligned in a world coordinate system, *i.e.*, corresponding astronomical objects are stacked on top of each other. Cosmic ray events, on the other hand, are statistically distributed in the individual frames, *i.e.*, an alignment of several cosmics in the stack is very unlikely. When the stack is fully loaded, in the example with 5 levels, a median image of the shifted frames is extracted in an analogous way as for the sky modelling process. Since the images were shifted with different offsets, only the central area will overlap for all frames. The outer regions, where individual images do not contribute, are marked and left blank (see Fig. 5.5).

The median image is already free of cosmic ray events, since it is improbable that an extracted pixel column contains more than one cosmic. This frame is a first order approximation of the sum — neglecting any scaling factors — and is again used as reference image, in analogy to the median value in the above discussed outlier-clipping mode. However, the photometry, *i.e.*, the total integrated flux of individual objects, in the pure median image is systematically decreased by up to 20% compared to the real superposition without cosmics removal. This introduced error is caused by object size variations due to a changing seeing and by the alignment uncertainty of up to one pixel. If corresponding objects in the different frames differ slightly in position and size, the median process will truncate flux, especially in the intensity maximum and the outbound wings.

Since the object photometry in the pipeline summation image should be as good as possible, a more elaborate algorithm is implemented for the cosmics removal and summation process, as is schematically illustrated in Fig. 5.5 for an individual pixel. The principle is similar to the outlier-clipping sky modelling method with the difference that corresponding objects are now aligned and that their flux should be conserved while removing only cosmic ray events. The first step is again the extraction of a pixel column, now in world coordinates. The reference value for the cosmics detection is taken from the predetermined median frame. The Poisson standard deviation σ_{sum} of the reference level n_{sum} is calculated according to Equ. 5.1. With the specified cosmics cutoff parameter κ_{sum}, the cutoff level CUT_{sum} can be calculated in analogy to Equ. 5.2.

Whenever a count level exceeds CUT_{sum} in the pixel column, a candidate for a cosmic ray event is detected. However, outliers are also expected to be found close to the center of stars, where a misaligned intensity maximum can trigger a false alarm. In order to rule out a possible removal of stellar flux, the pixel neighborhood of the candidate is checked for an astronomical object in the median reference frame. If a star is present, the outlier will remain untouched; if no object is found, the candidate is classified as cosmic ray event. The count level of a cosmics pixel is in this case replaced by the median reference value. Once all outliers have been checked and replaced, if necessary, the values of the pixel column can be added and the cosmics cleaned sum saved in an auxiliary array. By looping over all pixels, the full cosmics cleaned sum image of all frames on the stack is obtained.

This intermediate result is scaled back to the original sum of the count levels of the input data and added to the master sum, which is the superposition of all images up to the current frame. In online-mode the intermediate sums are saved on disk for immediate availability. The final result is the cleaned master sum of all images in the input catalog that is cut in order to remove the non-overlapping edge areas. Due to the built in object check, the photometry of stars is now conserved and — within normalization errors — identical to the real sum without cosmics removal.

Object detection and offset determination

The module for the object detection and frame offset determination is the most involved secondary function and is only briefly summarized here. About a dozen internal parameters are required for the object detection and analysis process. Examples include the number of stars searched for, the tolerable deviation from the expected object position, background thresholds, and stellar object selection parameters.

The first image of the input catalog is the designated reference frame for the whole summation process. In this master frame, a given number of reference objects is searched for by dynamically adjusting a test threshold level until the desired number of object candidates remain. At a given test threshold, all pixels values are compared to the reference level. Whenever a value above the threshold is found, the pixel-neighborhood is inspected for additional high count levels. If a cosmic ray signature is found, *i.e.*, only an individual pixel exhibits a high value, the object search will continue. On the other hand, a grouping of high level pixels indicates a possible stellar object candidate and is further investigated. The candidates are analyzed by a subfunction that determines the center of mass[6] co-ordinates, the total flux, and the approximate FWHM of the object. If the candidate is classified as star by the function, *i.e.*, the determined FWHM is comparable to the smallest values, the coordinates and object properties are stored in a reference list. If the number of found objects is not in agreement with the object parameter, the test threshold level is adjusted accordingly.

This final set of reference objects is searched for in all subsequent frames. The expected frame offsets from the telescope position were determined in the preparation steps and are

---

[6]Meant is the center of mass of the 2-dimensional intensity distribution which is equivalent to the first moment of the distribution.

now used to calculate the start position for the object search. The function looks for pixel values above a threshold with an increasing search radius from the start position. For each detected candidate, the object properties as listed above are determined by the subfunction. If the candidate characteristics and the reference object properties are comparable, they are classified as match and the newly measured position is saved. Once the object reference list is worked off, the determined true offsets of all found objects are averaged and saved. The refined frame offsets to the reference frame can now be used for an accurate shift and alignment on the summation image stack.

5.4 Pipeline Performance

In this section, the pipeline results and the performance of its main components will be investigated.

The data used for most following performance test were acquired on January 16th, 2003 under good observing conditions. A second data set of H-band observations is presented in Chap. 6. The images were taken using the standard observing utility presented in Sect. 4.2.2, *i.e.*, the field contains few objects. The observations were conducted in the narrow band continuum filter centered at $1710\,\mathrm{nm}$ and are made up of 79 images with an exposure time of 30 seconds each. The central object of interest is a quasar at redshift $z = 1.5$ and its surroundings. The quasar with the above redshift was chosen because its observed H_α emission line (see Tab. 2.2) is shifted into the transmission window of the narrow band filter, which can be seen from Equ. 2.3. The contrast to the background and objects at different redshifts is thus expected to be enhanced.

The currently available calibration frames are only provisional and are far from being optimized. The dark current frame contains corrections for the three most obvious warm pixel areas. The bad pixel mask has $\mathcal{O}(1000)$ entries but the criteria for the selection are not optimized yet and need further refinement. The flatfield was constructed from dome flats only, *i.e.*, the global quantum efficiency variations are not accurately mapped because of the inhomogeneous dome illumination. The mentioned readout problems causing varying features contributed to an additional degradation of the flatfield quality.

At the time the test data was taken, the detector showed extraordinary features, *e.g.* stripes and ramps as were mentioned in Sect. 5.1, that are (currently) not correctable and need further intensive investigation.

Due to the lack of optimized calibration frames and the additional detector characteristics discussed, it has to be expected that the pipeline reduced and superimposed images still exhibit undesired features.
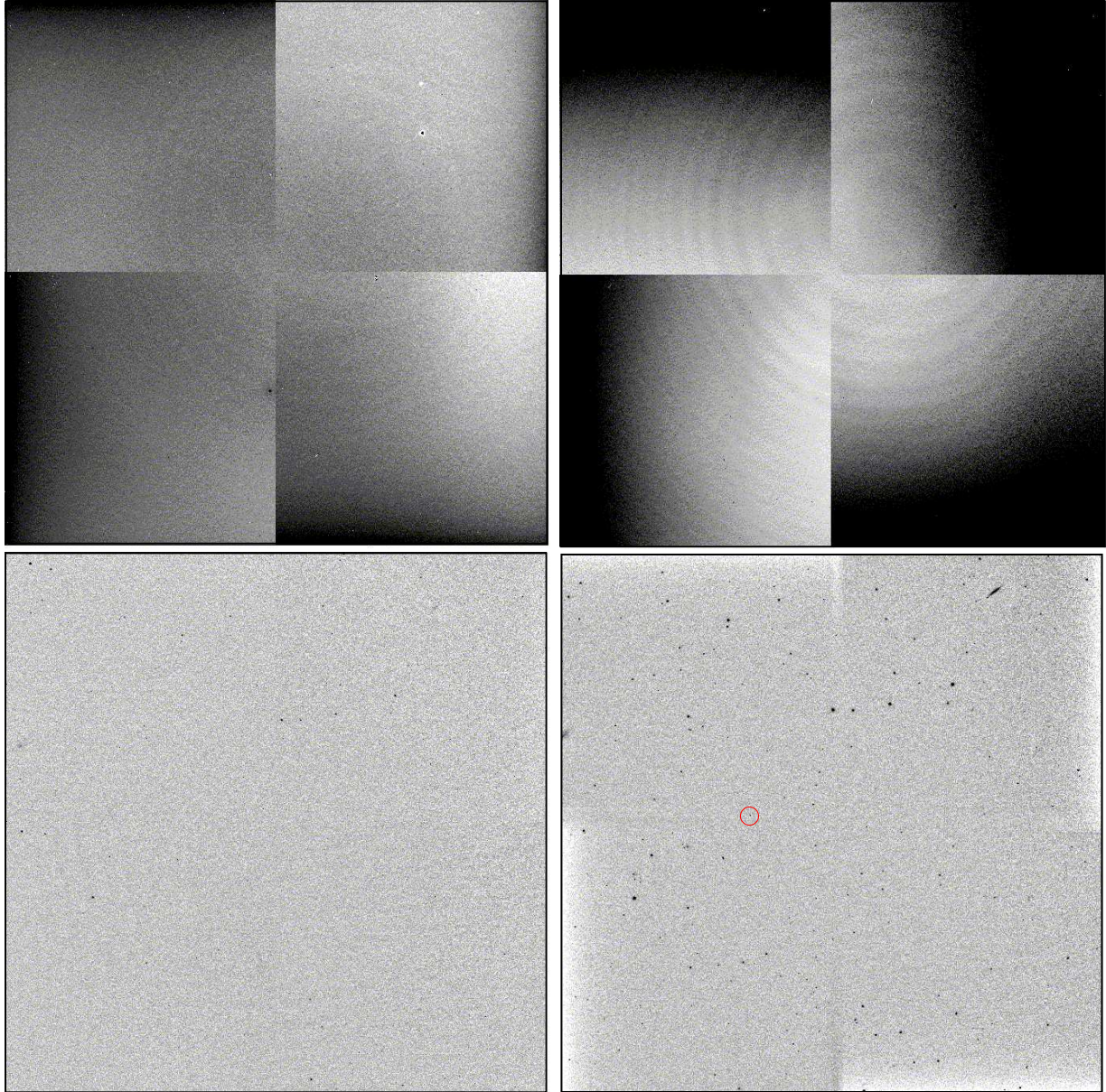
Figure 5.6:   Overall pipeline performance. *Top left panel:* Raw input data frame. *Top right panel:* Modelled sky. The ramps that were not corrected by the flatfield division are clearly visible. *Bottom left panel:* Reduced single frame. *Bottom right panel:* Superposition of 79 images. The central quasar is now visible and is marked by the red circle.

5.4.1 Overall performance

Figure 5.6 shows a representative set of pipeline input and output images. The pipeline was run in the high quality standard reduction mode (see Tab. 5.3), with outlier-clipping from 7 stack frames for the sky determination.

In the top left panel, a raw data input frame is displayed which exhibits the detector features discussed in Sect. 5.1. The modelled sky is shown in the top right panel. All detector features that could not be removed by the calibration process are visible here. Most obvious are the ramps that are now revealed — depicted with higher contrast — to extend over about half a quadrant each. The fact that they are also visible in the final sum image indicates that these features are neither additive nor multiplicative. The second peculiar feature is the set of off-centered concentric rings that extend over the whole detector. Their origin is not yet fully understood and needs further investigation[7]. In addition, individual bad pixels that are not yet contained in the bad pixel mask are also visible.

The reduced single frame in the lower left panel of Fig. 5.6 already shows some of the astronomical content of the data. The brightest objects in the field of view are now distinguishable from the flattened background. The superposition of all 79 images in the lower right panel finally reveals the full content of the field, including the quasar of interest indicated by the red circle. Due to the fairly large pixel scale of the detector in combination with the image representation, not all detected objects are visible at this scale.

5.4.2 Sky modelling

Since the final sensitivity and signal-to-noise ratio of the reduced data are primarily defined by the quality of the modelled sky, the pipeline performance of this important component is of special interest and will be presented in detail.

Flatness

In Fig. 5.7, the variance of the sky background in a raw data frame and a reduced image is compared. The count levels are plotted against the pixel number of the central half of a row without any bright objects. The black line represents the original raw data count levels of the frame in the top left panel of Fig. 5.6. The high noise level is due to the pixel-to-pixel sensitivity variations, *i.e.*, the fixed-pattern-noise. The red line depicts the background value distribution of the same detector row but now taken from the reduced single image (bottom left panel of Fig. 5.6).

The plot illustrates that the flatfielding and sky modelling process successfully eliminated the systematic sky count level variations across the detector and significantly reduced

---

[7]The most probable cause of the concentric rings is an interference effect introduced by the filter with its plane parallel surfaces. As can be seen in Fig. 2.5, the transmission window of the NB1710-filter contains two strong OH emission lines. These sharp lines could act as a monochromatic light source, which is a precondition for the observation of interference patterns.

the noise. The result is a very constant background level with only small fluctuations remaining. The count level offsets of the two lines are due to the different location of the statistics window, where the preserved median level is determined.

The noise improvements of the reduction and summation processes are listed in Tab. 5.4. Shown are the median count levels, the standard deviation, the noise uncertainty in per cent of the median level, and the noise improvement factor for the images displayed in Fig. 5.6. The last column of Tab. 5.4 indicates that the total noise plotted in Fig. 5.7 is suppressed by more than a factor 10 for the reduced image. The additional noise reduction due to the superposition of 79 images is in good accordance to the expected improvement factor of $\sqrt{79} \approx 9$ (see Sect. 5.2.1).

Image	Median Level	Std.Deviation	Noise [%]	Improv. Factor
raw image	6632	508.5	7.67	-
reduced single	6340	36.98	0.58	13.2
reduced sum	5.618×10^5	360.6	0.064	120

Table 5.4: Background statistics determined from a 500×300 pixel sub-frame with no bright objects. The background properties are calculated for a raw input image, the reduced single frame, and the superposition of 79 images. The first column lists the median count level of the sub-frame, the second the standard deviation σ. The noise in the third column is given in per cent and is the quotient of σ and the count level. The noise improvement factor is determined from the noise ratios in the third column. The used sub-frame is different from the pipeline statistics window, which accounts for the different count levels of raw and reduced image.
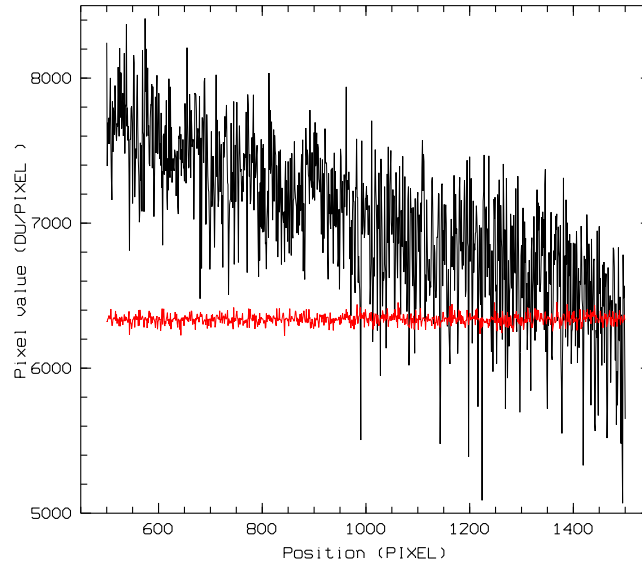

Figure 5.7: Sky flatness. The central part of a detector row without any objects is plotted against the pixel values. The black line represents the sky of the raw data including the fixed-pattern-noise, the red line the background of the reduced image. The count levels differ because the plotted row is located outside the statistics window, where the median sky value is defined.

Figure 5.8: Comparison of sky modes. *Central panel:* Representative sub frame of a single image reduced with the fast median sky mode. The count level is roughly 6300. *Left panel:* Image obtained by subtracting the minimum sky mode from the median mode frame in the central panel. The cuts are set to [0,20] counts. The black areas had a lower determined sky value in the minimum mode compared to the median mode. *Right panel:* Median mode subtracted from outlier-clipping mode. The cuts are also set to [0,20] counts. The position of the objects in the used image for the sky modelling process are clearly visible. This implies that the median mode takes off some star flux during the sky subtraction.

Comparison of sky modes

The performance of the three different pipeline sky mode is illustrated in Fig. 5.8. The central panel shows a sub frame taken from a single image that was reduced in the fast median mode. The number of frames for the sky modelling was set to 7 for all compared images. In order to enhance the difference, two images obtained with unequal sky modes were subtracted in the left and right panel.

The right frame in Fig. 5.8 results from the subtraction of the median mode image (central panel) from the frame reduced with the outlier-clipping mode using a cutoff parameter $\kappa = 3$. The cuts of the difference frame are set to [0,20], whereas the original count level in the central panel is about 6300. This implies that all pixel values differing by more than 0.3% from one mode to the other will be black in this representation. The star sized dark areas scattered around the actual star positions (see central panel) indicate the location of these objects in any of the 7 stack images and point out the dither pattern used for the observations. At these regions the outlier algorithm properly removed the stellar flux contribution before the sky determination. Thus, the subtracted sky value was smaller resulting in a reduced final image with the proper and slightly higher count level at these positions, which is visible in the image. Individual pixels noticeable in this representation are either statistical outliers (central region) or due to an increased noise caused by a detector ramp (right) or quadrant edge (left).

The left panel illustrates the difference of the median method and the minimum mode, where the average of the two smallest values was taken as sky value. The cuts are again

set to [0,20]. Dark regions in this representation are due to a smaller sky value and thus a higher reduced image level in minimum mode compared to the median reference frame. It can be seen that essentially the whole minimum frame is biased toward higher count levels which is equivalent to smaller determined sky values. This is an unwanted effect for sparse field observations, but can yield more appropriate sky values in the case of crowded fields and extended objects, as will be shown below.

Extended object reduction

As mentioned at the beginning of this chapter, the OMEGA2000 pipeline can also be used for the reduction of extended object observations, though it was not primarily designed for this purpose. A demonstration of the achieved reduction quality is given in Fig. 5.9, which shows the whirlpool galaxy M51 with its companion, as seen in the narrow-band filter centered around $1.71\,\mu$m. The raw input data were six 60 second object exposures and five intermediate sky observations. The pipeline was run in minimum mode, with $n_{ave} = 2$ and five frames on the sky stack. The displayed result is the pipeline produced sum image. The designated sky observations are automatically excluded from the summation process.
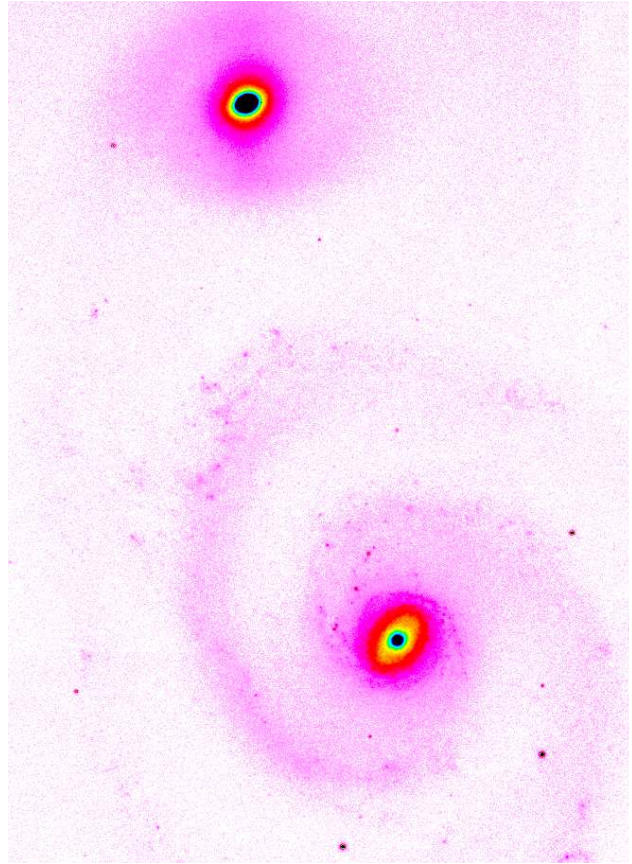
Reduction speed

One of the important goals for the development of the pipeline software was the minimization of required processing time in order to allow an efficient online reduction while observing. The aim was a full frame processing period that is no longer than a typical image integration time of 30 seconds.

Figure 5.9:   M51 with companion. This image was pipeline reduced in the minimum mode and is a superposition of six 60 sec frames.

Table 5.5 compares the average pipeline reduction speed for the OMEGA2000 instrument computer[8] (left) and a second widely used model (right). Since the sky modelling

---

[8]The original OMEGA2000 instrument computer failed a performance test and was replaced by the faster model now in use. The original model could not properly handle data acquisition, pipeline reduction, and a MIDAS session in parallel.

takes up to 50% of the total processing time, the required time is given according to the used sky mode. For better comparison, the sky was always modelled from seven frames. The listed full reduction time includes the calibration and the summation process, whereas the first row only states the time used for the sky modelling.

As can be seen in Tab. 5.5, the reduction speed of the OMEGA2000 instrument computer is well within the above specification for all sky modes. From the listed values, the total full frame processing times can be estimated for the standard reduction modes described in Tab. 5.3. With only five sky frames used for the standard online modes (1+2), the total reduction time will decrease by about 10% and can thus be finished in under 10 seconds. For the high quality reduction modes (3+4) with nine sky frames, the values listed in the bottom row of Tab. 5.5 will increase by about 10%. This implies that the standard online reduction modes (1+2) work about twice as fast as the high quality modes (3+4). As was shown above, the online data reduction pipeline will be capable of handling the incoming OMEGA2000 frame rate in real time for all practical observing applications.

	Sun Fire280r (1.1Ghz)			Sun Enterprise450 (400MHz)		
	Median	Minimum	Outlier	Median	Minimum	Outlier
Sky Modelling	3	7	8	7	16	18
Full Reduction	10	14	15	29	34	35

Table 5.5: Pipeline reduction speed. The columns contain the average required computing times in seconds per sky modelling process (with 7 images) and per full single image reduction for two different hardware setups. The OMEGA2000 instrument computer at the telescope is the *Sun Fire280r*-model on the left. The full reduction values for the model *Sun Enterprise450* on the right differ only slightly because the slower frame i/o-times are dominant.

5.4.3   Cosmics filtering

The goal of the cosmics filtering algorithm is the complete removal of cosmic ray events while preserving all other count levels, especially the object flux contributions.

The results of the filtering process are illustrated in Fig. 5.10. The left panel shows a sub image of the "dirty" sum of the 79 input images, *i.e.*, the direct real sum without cosmics cleaning. The frame on the right shows the difference of the image on the left and the cosmics cleaned sum, *i.e.*, the pixels that were classified as cosmic ray events and replaced. The count level in the sum image is about 560 000, the cuts in the right frame are set to [150,300]. Thus, all pixel values that were decreased by more than 0.05% by the cosmics filter are black. The filter cutoff parameter was set to $\kappa_{sum} = 10$, which implies that pure statistical outliers should be negligible.

The fact that only individual pixels are visible in the difference image with the above strict cuts demonstrates the general proper summation of the images. Moreover, no real objects can be seen in the difference image, which indicates that the full stellar flux is conserved and excluded from the clipping process. The actually clipped pixels in the left
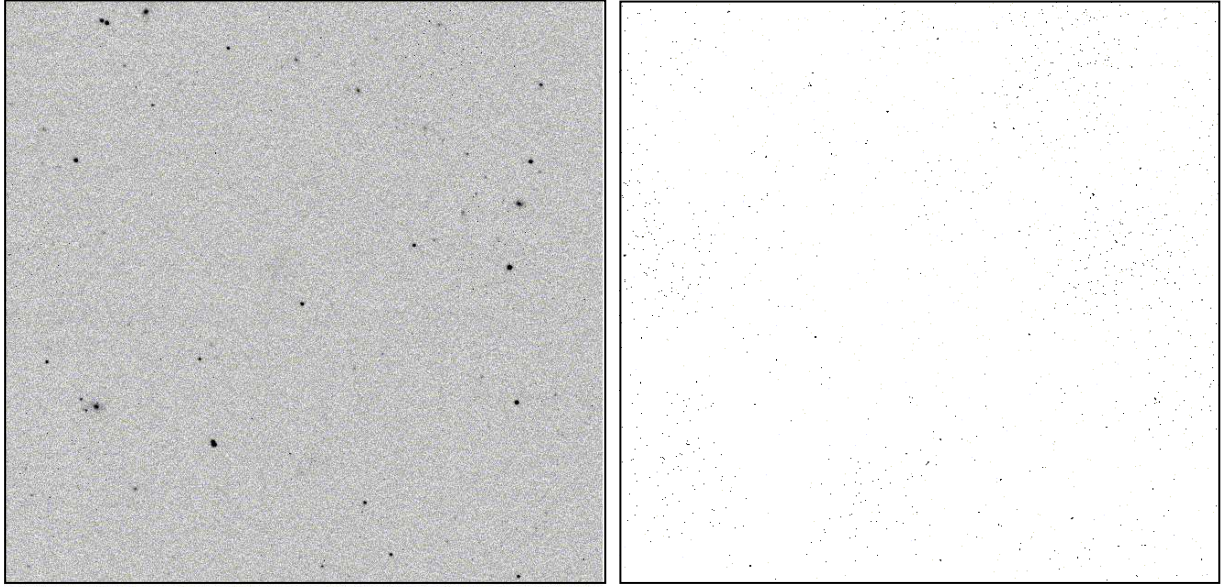
Figure 5.10: Cosmics filtering results. *Left panel:* Real, uncleaned sum of 79 images, including cosmics. The count level is about 560 000. *Right panel:* Difference of real sum image and cosmics cleaned sum image. The cuts are set to [150,300]. Classified and replaced cosmic ray events are black in this representation.

panel are either real cosmic ray events, accumulated over almost 40 minutes, or caused by uncorrected individual bad pixels, which accounts for the clustering in some areas. Due to the shifting of the frame, an uncorrected bad pixel will appear in different positions in the superimposed image. Thus, each bad pixel will produce a group of outliers according to the total number of images, *i.e.*, in the case of Fig. 5.5 a cluster of 79 outliers.

5.5   Discussion and Limitations

As was discussed in the last section, the developed OMEGA2000 data reduction pipeline has yielded promising results. Thus, this additional feature of the instrument package will serve as a useful and convenient tool for real-time data analysis as well as customized automatic reductions for all future OMEGA2000 observations.

The pipeline objectives listed in Sect. 5.1 have been fully met. By providing four pre-defined standard reduction modes, as described in Sect. 5.2.1, most pipeline applications can be started without any additional input specifications necessary. An optimized user defined reduction after the actual observations is also possible by fine tuning the set of input parameters.

However, the OMEGA2000 pipeline has some intrinsic performance limitations that could be improved in a further developed version of the software:

- The reduction of observations in the extended object mode is not yet optimized for the appropriate handling of the alternate designated sky observations. However, decent reduction results can already be obtained with the minimum sky modelling mode, as was demonstrated in Fig. 5.9.

- Objects with angular extensions larger than $25''$–$30''$ are not sufficiently shifted by the dither pattern and thus cause a bias towards higher values in the outlier-clipping sky modelling process. This implies that some of the object flux is subtracted which reduces the sensitivity in the local neighborhood. In order to avoid this overcorrection, an automated detection of extended objects would have to be implemented, which in turn switches from outlier-clipping mode to the minimum method for the vicinity of the object.

- The sky determination around faint objects and the intensity wings of brighter stars could be improved by an additional data smoothing before the sky modelling process. The full extensions of objects would be better detectable above the sky noise and could be accounted for. However, the additional prior data filtering takes a lot of computational effort and will at least double the processing time for the sky modelling.

Chapter 6

Applications

In this chapter, two pipeline-reduced data sets are used to address two important issues for future OMEGA2000 observations: First, the temporal and spatial sky background variations are investigated; second, the limiting magnitude for a deep exposure is determined.

The two data sets consist of the 79 30-second exposures in the narrow-band filter centered around $1.71\,\mu$m already presented in Chap. 5, and 179 30-second H-band exposures. The observations both cover the same field, centered on the previously mentioned quasar at $z = 1.5$. The images were taken on January 16th & 17th, 2003 under good observing conditions.

6.1   Temporal and Spatial Sky Background Variations

As was discussed in Sect. 2.3.1, the OH-airglow background imposes the biggest challenge for the data reduction process in the near-infrared wavelength region. The varying nature — temporally as well as spatially — of these sky emission lines requires the elaborate sky modelling techniques presented in the last chapter.

In order to optimize the pipeline and observation parameters, the typical scales on which the background varies significantly have to be accurately known. The sky modelling strongly depends on the temporal and spatial correlation of the background in all images used to remove the sky contribution. Thus, the airglow variation timescale limits the number of input images for the sky stack, whereas the spatial fluctuation scale defines the degree of correlation of designated sky observations.

The OH emission lines and their relative strengths in the H-band are displayed in the bottom panel of Fig. 2.5. This set of molecular transition lines is the main contributor to the observed airglow background. As can be seen in Fig. 2.5, the transmission window of the narrow-band filter at $1.71\,\mu$m includes two sharp and prominent OH-lines at $1.7078\,\mu$m and at $1.7123\,\mu$m (Rousselot *et al.*, 2000).
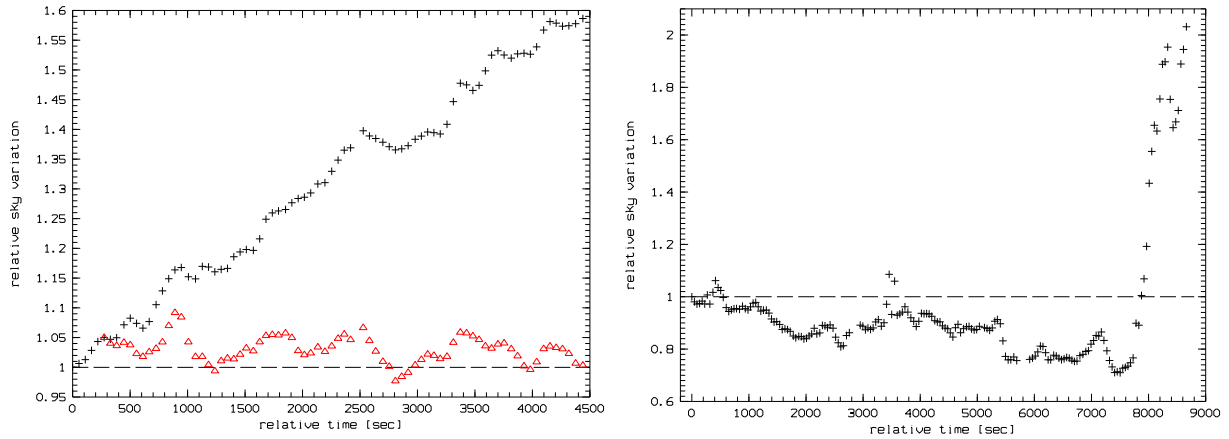
Figure 6.1: Temporal background variations. *Left panel:* Relative sky background variations versus relative time in the narrow-band filter NB1710. The images were taken between 4:20 UT and 5:36 UT. The black crosses represent absolute measurements with a starting count level of 180 counts/sec. The red triangles depict the variation relative to the background level 5 images back, *i.e.*, 4.5 minutes ago. *Right panel:* Relative sky variations in the H-band between 1:30 UT and 3:55 UT. The absolute sky level is 2000 counts at unity. The minimum was reached at around 3:35 UT.

6.1.1   Temporal variations

In order to obtain accurate sky levels at the actual moment of observation, the pipeline reduction was run in the outlier-clipping mode with 5 input frames for the sky modelling. This implies that the measurements are somewhat correlated to the two succeeding and preceding data points. The background levels were extracted from the modelled sky frames by determining the median value of the 200×200 pixel statistics window. Thus, the statistical errors are very small and are not plotted.

Figure 6.1 illustrates the changes in the background sky level over periods up to 2.5 hours. Twilight started at 5:50 universal time (UT) on the observation nights. The left panel of Fig. 6.1 displays the measured sky background in the narrow-band filter observations. The relative sky variation — normalized to the first measurement — is plotted versus the relative time in seconds, again starting with the first data point. The images were taken between 4:20 UT and 5:36 UT, *i.e.*, just prior to the start of twilight. The black crosses represent absolute measurements, where the start value 1 is equivalent to 180 counts/sec. The background value increases by about 50% within one hour with small dips in between. This sharp background rise is already observable 90 minutes prior to astronomical twilight. The red triangles in the same plot are the same measurements normalized to the background value 5 images back, which corresponds to an offset of 4.5 minutes. From this representation it can be seen that the background can increase by up to 10% within about 5 minutes. This growth rate exhibits quasi-periodic behavior with a time scale of 10-15 minutes.
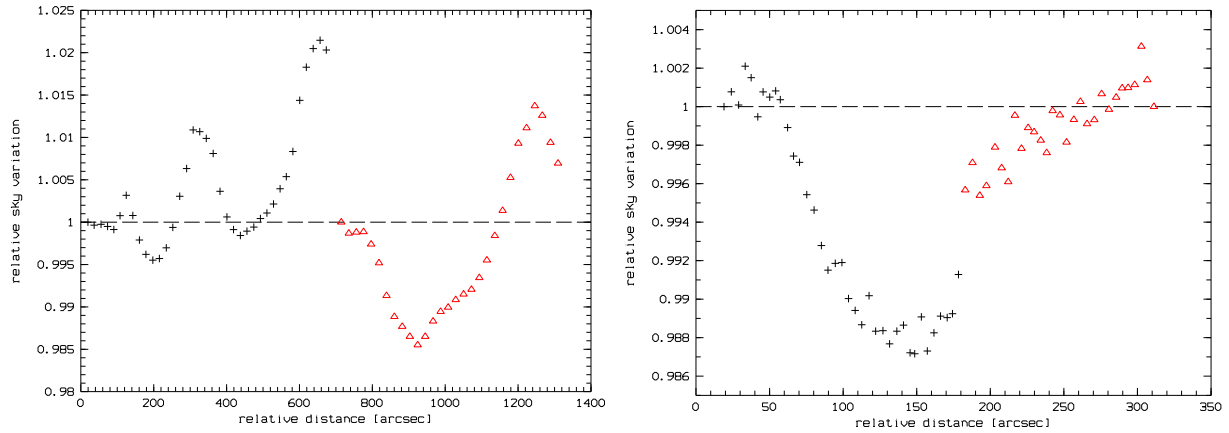
Figure 6.2: Spatial background variations. *Left panel:* Relative variations over 10 arcminutes measured in horizontal (black crosses) and vertical frame directions (red triangles). The data points are the median values of 40×40-pixel detector regions. *Right panel:* The same measurement with higher resolution. The median of 10×10-pixel regions was taken.

The right panel of Fig. 6.1 shows the change of the background level in the H-band measured over a period of 2.5 hours. The observations started at 1:30 UT and ended at 3:55 UT. The absolute background value at the unity level is 2000 counts/sec. The background level exhibits a gradual reduction, with some intermediate surges of 5–10 minutes. The minimum is reached around 3:35 UT, at approximately 30% below the initial level, directly followed by a very steep background rise that boosts the sky level by a factor of three within 20 minutes. The turning point occurs approximately 135 minutes before the beginning of the astronomical twilight.

6.1.2 Spatial variations

Figure 6.2 depicts the sky background spatial variation in the H-band within the OMEGA2000 field of view. The relative variation is plotted versus relative distance in the horizontal (black crosses) and vertical (red triangles) frame directions. The measurements were conducted on a modelled sky image.

In the left panel of Fig. 6.2, the variation of the background level over about 10 arcminutes is displayed. The data points are the median values of adjacent 40×40-pixel detector regions in horizontal (black) and vertical (red) directions. The right panel shows the same measurement at a higher resolution, using adjacent 10×10-pixel regions.

The maximum observed amplitude of the background variation is about 3% over a distance of 5 arcminutes (triangles in the left panel) and roughly 2.5% over a 3.5 arcminute separation (crosses in the left panel). The plot with increased resolution in the right panel reveals the fluctuations over the typical dither offset distances. The maximum observed background difference over a 40 arcsecond separation is 0.6% (crosses), with a typical value of about 0.2%.

6.1.3   Discussion

The sky background measurements have shown that the airglow caused by OH line emissions varies dramatically over the course of a night. From the data shown, it can be estimated that the minimum sky background is reached about 130–140 minutes prior to astronomical twilight, immediately followed by a strong rise in sky levels. Whether this surge is a systematic effect occurring every night or a non-reproducible incident cannot be answered with the available data. However, background variations by a factor of 3 within a period of 20 minutes have to be expected in the H-band.

The typical sky level rise of 5–10% every 5 minutes, as shown in Fig. 6.1, can most probably be accounted for by a combination of the zenith angle dependance of the sky brightness and a re-excitation of OH radicals in the upper atmosphere. The time scale for significant background changes of 10–20% at any time of the night can be confirmed to be $\mathcal{O}(10\,\mathrm{min})$, as was stated in Sect. 2.3.1.

Concerning the spatial variation of the sky emission, systematic changes of up to 3% within the OMEGA2000 field of view could be observed. These wavelike structures over 4–5 arcminutes on the detector correspond to atmospheric regions of about 100 m in size at an altitude of 90 km. The above spatial fluctuations limit the sky determination accuracy for extended object observations.

On the scale of typical dither offsets, spatial variations of up to 0.6% were observed. These small scale fluctuations limit the quality of the pipeline modelled sky that is extracted from shifted images. The measured noise in a reduced image, 0.58% (see Tab. 5.4), is in good agreement with the above value and is thus near the external limit imposed by small scale sky background fluctuations.

6.2   Limiting Magnitude

This section will deal with the analysis of a deep 90-minute exposure in the H-band. After the data presentation, the counts for zero magnitude are determined, which can in turn be used to calibrate the brightness of faint objects. Finally, the preliminary sensitivity is compared with the OMEGA-Prime instrument.

6.2.1   Deep Exposure

The deepest OMEGA2000 image currently available is an H-band observation of the previously presented quasar field with a total exposure time of 5370 seconds, or 89.5 minutes. The seeing at the time of observation was $1.3''$. The data was pipeline reduced using the high-quality standard reduction mode with 9 input frames for the sky modelling process.

Figure 6.3 shows the full field of view of the final summed image. The full detector resolution can be seen in Fig. 6.4, where sub images with a magnification of 3 (left panel) and 9 (right panel) are displayed. These closeup views confirm OMEGA2000's excellent image quality.
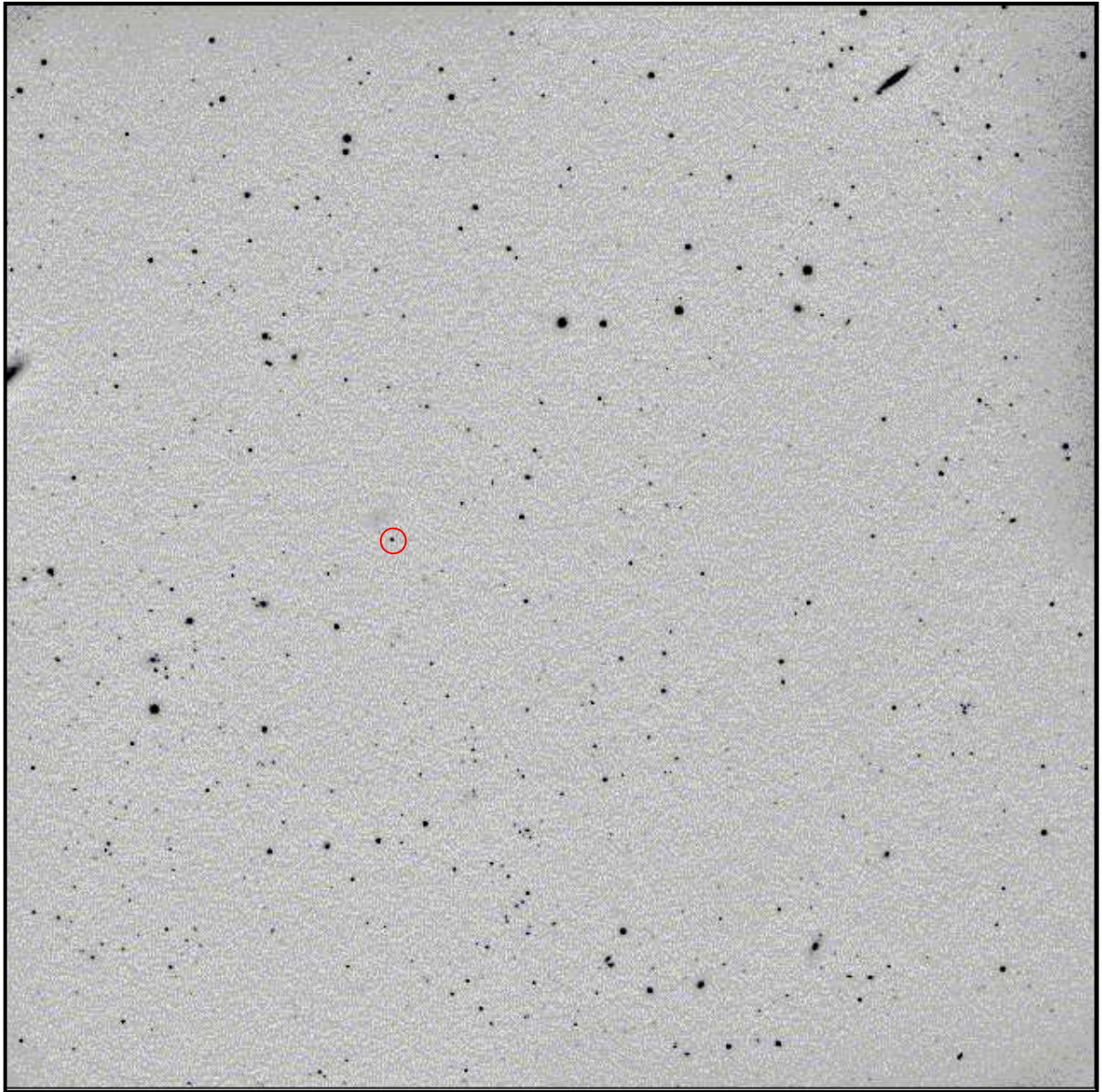
Figure 6.3: Deep 90-minute exposure in the H-band. The image is a superposition of 179 frames with the full field of view displayed. The background count level is 10^7. The quasar at $z = 1.5$ is marked by the red circle.
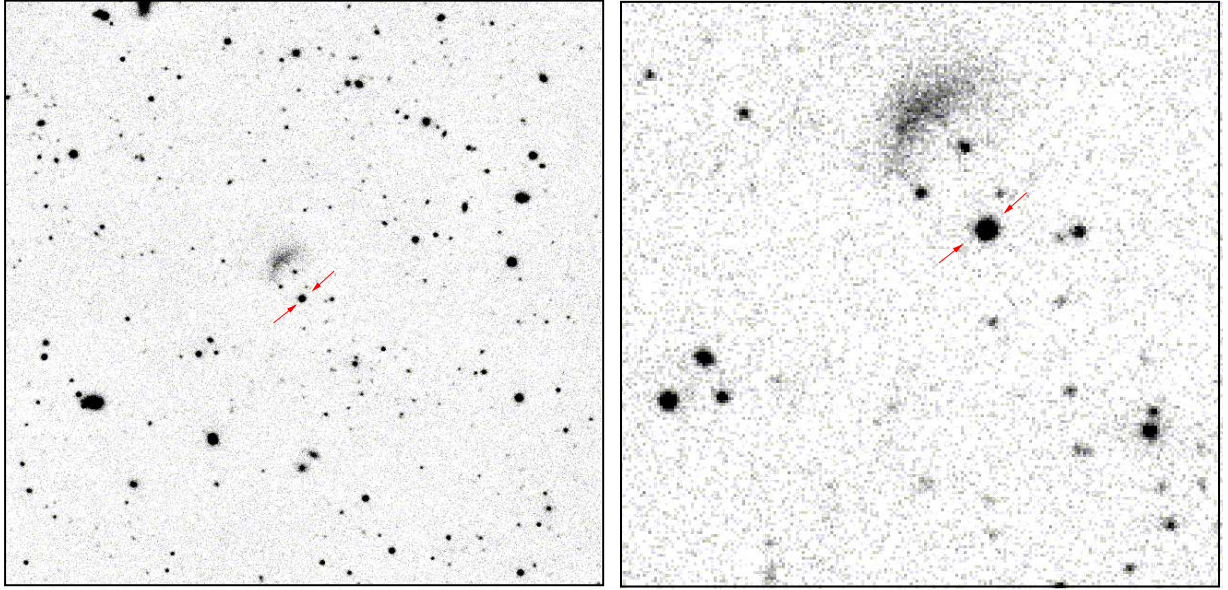
Figure 6.4:   Deep exposure closeup. The images show zoomed in sub frames of the 90-minute H-band exposure with the quasar at $z = 1.5$ at the center (red arrows). *Left panel:* $5' \times 5'$ sub-image with full detector resolution. The scale is magnified by a factor of 3 compared to Fig. 6.3. *Right panel:* Zoomed by another factor of 3. Individual pixels are now visible.

6.2.2   Counts for zero magnitude

Before the brightness of faint objects in the deep exposure can be calibrated, the counts corresponding to zero magnitude have to be determined from infrared standard stars.

The open cluster M67 contains three UKIRT faint infrared standard stars[1], with two located within the field of view of many OMEGA2000 images taken during the first commissioning run. The counts for zero magnitude were determined from a single flatfield-corrected 16-second exposure in the H-band.

All subsequent flux measurements were carried out using the MIDAS function STATISTICS/IMAGE. This routine returns the total integrated flux within a specified aperture. By taking the difference between the total flux at the location of a given object and the background contribution determined in the local neighborhood, accurate object flux measurements can be obtained.

The signal-to-noise ratio (SNR) in the background-limited case was previously shown in Equ. 4.1. When using count units instead of detected electrons for the background and stellar fluxes, the given expression has to be multiplied by $\sqrt{g}$, where g is the gain.

The apparent magnitude m_1 of an object is related to the magnitude m_0 of a reference star and the measured flux ratio F_1/F_0 in the following way:

---

[1]A full list of all standard stars can be found under: `http://www.mpia-hd.mpg.de/IRCAM/OPRIME/Manual/OP_manual.html`

Std. Star	H-Mag	SF [counts/sec]	SNR	CFZM [counts/sec]
FS 16	12.669 ± 0.01	$(1.95 \pm 0.06) \times 10^4$	206	$(2.27 \pm 0.07) \times 10^9$
FS 17	12.343 ± 0.008	$(2.53 \pm 0.04) \times 10^4$	269	$(2.19 \pm 0.04) \times 10^9$
Average				$(2.23 \pm 0.04) \times 10^9$

Table 6.1: Counts for zero magnitude determined from two UKIRT faint infrared standard stars. Listed are the identifier of the standard star, its H-band magnitude, the measured stellar flux (SF), the signal-to-noise ratio (SNR) of the object, and the counts for zero magnitude (CFZM). The last row states the best estimated value of the counts for zero magnitude. The given SNR is valid for a calibrated and sky subtracted image and does not reflect the actual background uncertainty.

$$m_1 = m_0 - 2.5 \cdot \log\left(\frac{F_1}{F_0}\right) . \tag{6.1}$$

By applying the equation above, the expected count rate for a reference star of zero magnitude can be calculated. Tab. 6.1 lists the results obtained from the analysis of the two standard stars. The available data yield a best value for the above reference count rate of $(2.23 \pm 0.04) \times 10^9$ counts/sec.

The relatively large error, almost 2%, is due to the short integration time of the image used and the limited reduction applied. With only a flatfield correction and no other images available, the uncertainty of the sky level is still high and increases the absolute errors. The signal-to-noise ratio stated in Tab. 6.1 is determined according to Equ. 4.1 and reflects the SNR of a fully reduced image.

6.2.3 Object analysis

The determined value for the photometric zero point can now be used to calibrate the apparent magnitudes of faint objects in the deep H-exposure. By measuring the total integrated object flux and scaling it down to the object count rate per second, the apparent magnitude can be determined using Equ. 6.1.

In Fig. 6.5, the selected point sources for the flux measurement are marked and labelled with reference numbers. The results for these objects are listed in Tab. 6.2. Object #1 is the quasar at redshift $z = 1.5$, with a magnitude of 16.2.

The limiting magnitude (LM) is commonly defined as the apparent magnitude of an object with a signal-to-noise ratio of 5. Object #7, with a measured SNR of 5.2, is close to the above definition and can thus be used as a reference point source. Due to a well defined sky level in the local neighborhood, the magnitude of 20.33 mag could be determined to within an error of 0.1 mag.

By scaling the flux rate of the reference object to the defining SNR of 5, an estimate for the true limiting magnitude can be obtained, as is shown in Tab. 6.2 in the row labelled LM. The limiting magnitude for a 90-minute exposure in the H-band with a seeing[2] of 1.3″ can be specified as (20.36 ± 0.15) mag.

---

[2]The actual photometric quality of night was not determined due to a lack of calibration data. The stated value for the seeing is an average of FWHM measurements in the data set.
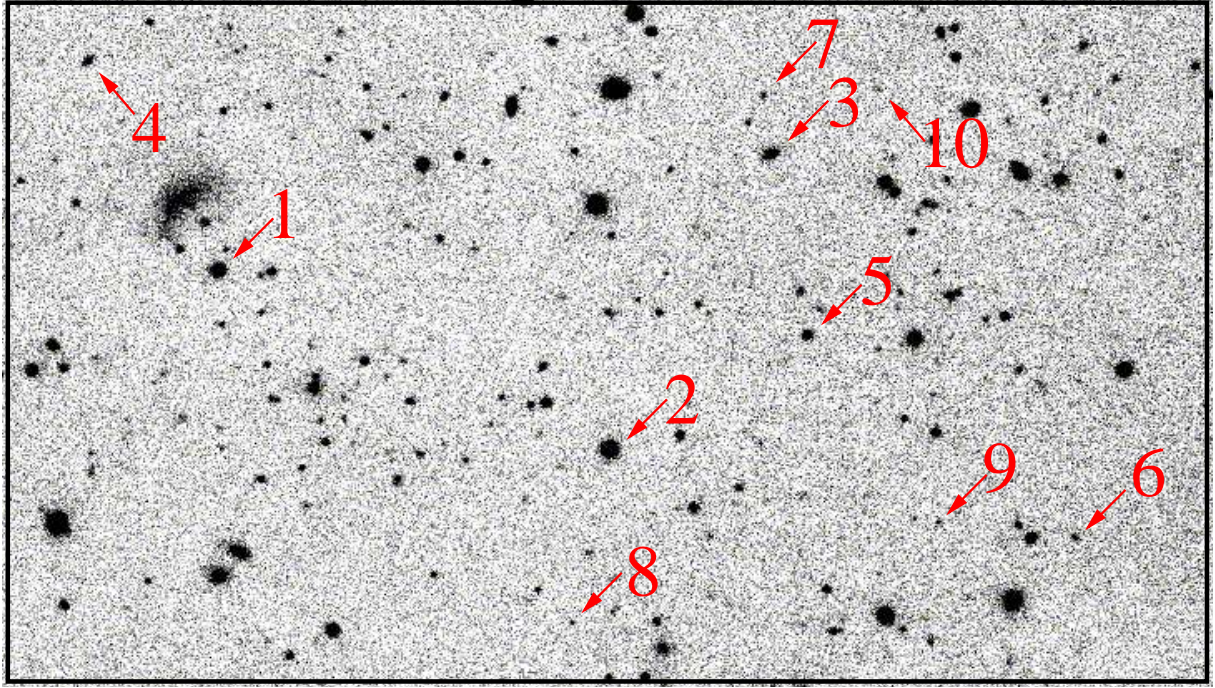
Figure 6.5: Faint object selection. The objects selected for magnitude determination are marked and labelled with the reference number used in Tab. 6.2.

The above value is a rather conservative estimate, since the aperture for the object analysis still included 121 pixels, *i.e.*, the background noise is fairly high. However, the measured SNR for object #7 is consistent with the signal-to-noise ratio in the central pixel. Since the OMEGA-Prime sensitivities are stated with reference to the central pixel SNR, the above estimated limiting magnitude for OMEGA2000 is suitable for a performance comparison of the two instruments.

6.2.4   Sensitivity

The sensitivity of an instrument is dependent on a number of issues. First of all, the quantum efficiency of the detector and the plate scale are critical. However, a loss of photons or additional stray light within the instrument will reduce the potential sensitivity. Moreover, the quality of the data reduction, *i.e.*, the performance of the pipeline, influences the limiting magnitude that is ultimately achieved.

The H-band sensitivity for the OMEGA-Prime instrument is stated[3] to be 18.1 mag for an integration time of 2 minutes and a seeing of 1″. In order to compare this value with the OMEGA2000 performance, the limiting magnitude of the deep H-exposure has to be scaled to the reference exposure time. Under the assumption that the signal-to-noise ratio of an object is proportional to $\sqrt{t}$ (see Equ. 4.1), where t is the exposure time, the

---

[3]See `http://www.mpia-hd.mpg.de/IRCAM/OPRIME/Manual/OP_manual.html` for further details.

Obj	Total Object Flux [counts]	Obj Counts/Time [counts/sec]	SNR	Magnitude [mag]	Error [mag]
1	3.825×10^6	712.3	149	16.24	0.05
2	8.367×10^6	1558	262	15.39	0.05
3	6.066×10^5	112.9	22.3	18.24	0.06
4	3.151×10^5	58.68	15.0	18.95	0.07
5	4.490×10^5	83.61	21.4	18.57	0.07
6	1.200×10^5	22.35	6.17	20.00	0.15
7	8.860×10^4	16.50	5.18	20.33	0.10
8	5.420×10^4	10.09	3.87	20.86	0.14
9	6.140×10^4	11.43	4.38	20.73	0.25
10	4.245×10^4	7.91	3.03	21.13	0.25
LM	8.560×10^4	15.94	5	20.36	0.15
Sky	4.964×10^7	9244		13.46	0.04

Table 6.2: H-band magnitudes of selected objects in the deep exposure. The analyzed objects are marked in Fig. 6.5. The columns list the object label (Obj), the total object flux in counts, the object flux per second, the signal-to-noise ratio (SNR), the derived apparent magnitude, and the error of the magnitude determination. The limiting magnitude (LM) was derived from object #7 using appropriate flux scaling. The last row states the H-band sky brightness per arcsec^2.

object fluxes at the limiting magnitude in two images with different exposure times t_0 and t_1 will differ by a factor of $\sqrt{t_0/t_1}$. Using this fact, the equivalent limiting magnitude for a 2-minute exposure can be estimated as (18.30 ± 0.15) mag.

The above result suggests that OMEGA2000 has a somewhat improved sensitivity compared to the OMEGA-Prime instrument. Taking into account that the OMEGA2000 images were taken under poorer observing conditions, 1.3″ versus 1.0″, a more significant sensitivity improvement can be expected in better seeing with the new instrument.

Chapter 7

Outlook

7.1 Open Tasks

Due to bad weather and technical problems, the OMEGA2000 commissioning phase could not be finished within the three scheduled runs. The instrument is currently back at the MPIA for a general overhaul and extensive testing. The final commissioning is planned for July 2003. If the instrument proves to be fully operational, OMEGA2000 will be available for general observations as soon as August 2003.

The list of open OMEGA2000 tasks for the upcoming months includes the following items:

Detector and Readout: The optimization of the detector and readout operation is the most critical item and thus has highest priority. The ramps and stripes that were shown in Sect. 5.1 need to be eliminated in order to allow accurate flatfield correction and reduce the total noise. In addition, the detector sensitivity has to be measured as a function of wavelength.

Filters: Most filters have either to be replaced or have their transmission properties checked. Tests suggested that a number of the current filters show a red leak, *i.e.*, they transmit some flux beyond their specified transmission window. Moreover, the focus offsets for the new filters have to be determined, as discussed in Sect. 4.3.1.

Calibration Frames: The global quantum efficiency variations across the detector have to be measured in all filters in order to provide accurate flatfields. In addition, the dark current frame and the bad pixel mask have to be optimized once detector operation has reached its final setup.

Baffles: The time required for positioning the movable baffle has to be decreased to allow rapid changes during the night. Furthermore, the influence of the undersized warm baffle has to be investigated under warm summertime conditions.

Reflections: The cause of the central bright spot observed in some filters has to be understood and eliminated.

Entrance Window: The entrance window of the dewar iced over several times during the test operation, which must be prevented in the future.

7.2   OMEGA2000 Projects

This concluding outlook on some selected future OMEGA2000 projects comes full circle to the opening remarks on scientific applications of near-infrared astronomy in Sect. 2.1. Since OMEGA2000 is a wide-field camera with a field of view of $15\rlap{.}'4 \times 15\rlap{.}'4$ and seeing-limited resolution, it will be mainly used for galactic and extragalactic surveys.

7.2.1   Galactic applications

One of the OMEGA2000 science projects will be a survey for low mass objects such as brown dwarfs and free-floating planets. These objects can be best detected in the near-infrared (see Tab. 2.1) by looking for candidates with extremely red colors.

Zapatero Osorio et al. (2000) showed that an extremely red, low luminosity population of isolated objects exists in a nearby star cluster around the star σ Orionis. In this study, three isolated giant planets with 5-15 Jupiter masses and effective temperatures of 1700-2200 K were found.

With OMEGA2000's large field of view, it will be possible to detect many of these low mass objects, which will lead to a better understanding of the formation processes of planets.

7.2.2   Extragalactic applications

Due to the cosmological redshift, galaxy surveys at optical wavelengths are restricted to redshifts of $z \lesssim 1$ (see Tab. 2.2). To extend surveys out to the redshift range of $1 < z < 2$, a NIR survey instrument is needed. It is currently believed that 30-50 % of all stars seen in the present universe formed in the latter redshift interval, which emphasizes the scientific importance of this cosmic epoch (Wolf *et al.*, 2003).

Two extragalactic survey projects for OMEGA2000 are the near infrared extension of the *COMBO-17* survey and the *HIROCS* search for distant clusters of galaxies.

COMBO-17 + 4NIR

The *COMBO-17* survey (**C**lassifying **O**bjects by **M**edium-**B**and **O**bservations in **17** filters) has classified about 36 000 galaxies out to redshifts of $z \simeq 1.15$, which is the best sample to date for the study of galaxy evolution. The upper redshift limit is defined by the shifted
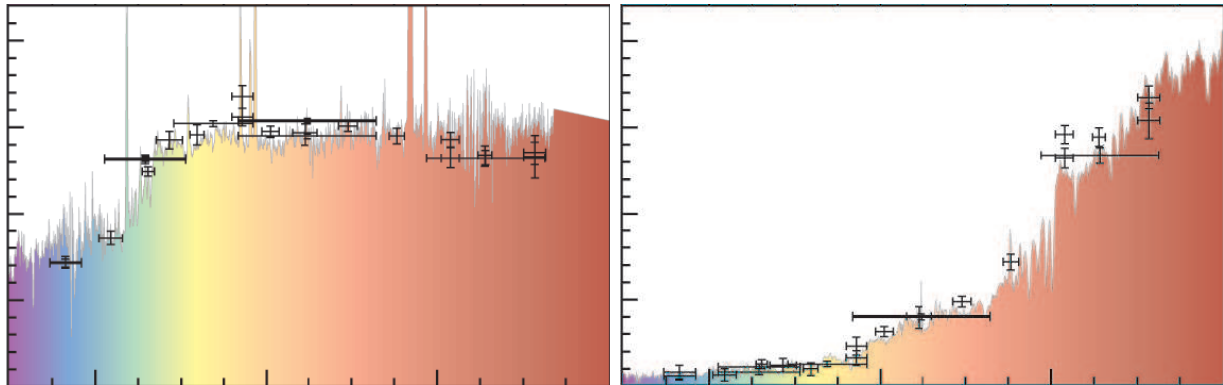
Figure 7.1: COMBO-17 redshift classification. The images show two detailed galaxy spectra in the optical wavelength range 300–1000 nm with the corresponding COMBO-17 low-resolution measurements. The horizontal bars represent the 17 filter transmission windows, the vertical bars the photometric error. Left panel: Spectrum of a spiral galaxy at redshift $z = 0.17$. The measured flux is well distributed over the whole optical region, which allows an accurate object classification. Right panel: Spectrum of a distant elliptical galaxy at redshift $z = 1.02$. Most of the flux has been shifted outside the optical region but some important spectral features are still visible. Accurate object classification in the optical region eventually fails if galaxy spectra are shifted even further toward the infrared. From Meisenheimer and Wolf (2002).

4000 Å break[1], which has to be within at least two optical filters to ensure an accurate photometric classification. For the classification, 16 colors are derived for each object by subtracting the magnitudes within a given filter from a reference filter. These object colors are combined to produce a 16-dimensional "color-vector", which can be compared and matched to a library of 100 000 color-vectors of known objects. This photometric method allows accurate redshift measurements of galaxies with $R \leq 22$ to within an error of ± 0.01 (Wolf *et al.*, 2003).

Figure 7.1 illustrates the filter sampling and classification technique of COMBO-17 for two galaxies at different redshifts. The right panel shows the spectrum of an elliptical galaxy at $z = 1.02$ with the visible 4000 Å break significantly shifted towards the red end of the optical region.

The OMEGA2000 survey extension *COMBO-17 + 4NIR* will make use of four additional near-infrared filters, out to the broad-band H-filter at $1.65\,\mu$m. With the additional color information in the near-infrared, the redshift limit of the survey can be extended out to $z \simeq 2.1$, thus including the important star-forming cosmic epoch mentioned above.

---

[1] The 4000 Å break is closely related to the Balmer-break but has additional contributions from various line blends such as Ca.

HIROCS

The second extragalactic survey to be carried out with OMEGA2000 is *HIROCS*, the **H**eidelberg **I**nfra**R**ed / **O**ptical **C**luster **S**urvey. The aim of this project is the acquisition of a statistically significant sample of distant clusters of galaxies up to redshifts of $z \lesssim 1.5$ (Röser *et al.*, 2003). The near-infrared observations with OMEGA2000 will be complemented by optical imaging with *LAICA*, the Large Area Imager for the Calar Alto. The scientific goal of the HIROCS survey is a better understanding of the evolution of the cluster population and their galaxies.

The survey will look for the prominent $4000\,\text{Å}$ break of elliptical galaxies that often populate rich clusters (Röser *et al.*, 2003). Overdensities of these objects in 3D-space (α, δ, z) indicate potential galaxy cluster candidates. As described above, the accurate detection of the $4000\,\text{Å}$ break spectral feature for redshifts $z \geq 1$ inevitably requires near-infrared observations with OMEGA2000.

Appendix A

List of Technical Terms and Acronyms

Baffle: Light shield placed in the optical path to block stray light and reduce the thermal background radiation.

Bias: An offset voltage applied to all pixels in an array detector.

CA: Calar Alto Observatory in Southern Spain

CCD: Charge-Coupled Device

CFHT: Canada-France-Hawaii-Telescope

COMBO-17: Classifying Objects by Medium-Band Observations with 17 filters

Command Line Parameter: Parameter that is passed to a MIDAS routine with a function call to allow a high degree of flexibility in the program

Cosmic: Cosmic ray event in an image. Signal in isolated pixels caused by a charged cosmic particle hit.

Descriptor: Data buffer with a name that contains information about an associated image.

Dithering: Common observation technique in infrared astronomy. Multiple images of an object are taken with slight telescope offsets in between the images. By overlaying several images and using a median process, the local sky for the data reduction can be extracted from the science images.

ESO: European Southern Observatory, with its headquarters in Garching, Germany.

FITS: Flexible Image Transport System. Standard format for astronomical images.

Flatfield: Image of a uniformly-illuminated area used for the correction of sensitivity variations across the detector.

FoV: field of view. Sky area that can be covered with one image of a particular instrument.

FPN: Fixed Pattern Noise. Pixel-to-pixel sensitivity variations that are corrected by dividing through a normalized flatfield.

FWHM: Full-Width Half-Maximum. In this thesis, always a measurement of the width of an object in an image. The FWHM is a well-defined number obtained by fitting a Gaussian curve of the form $f(x) = 1/(\sigma\sqrt{2\pi}) \times exp(-\frac{x^2}{2\sigma^2})$ to the intensity profile of an object. The standard deviation σ and the full width at half the peak intensity of the profile only differ by a constant factor $\sigma = 0.424 \cdot$FWHM (Stöcker, 1998).

Gain: Conversion factor from detected electrons to displayed counts.

GUI: Graphical User Interface

HgCdTe: Mercury-cadmium-telluride

HIROCS: Heidelberg InfraRed / Optical Cluster Survey

Image Catalog: List of image names that can be used within the MIDAS environment to apply a set of commands to all images in the list.

InSb: Indium antimonide

I/O: Input/Output

IR: Infrared

IRAS: InfraRed Astronomical Satellite

ISAAC: Infrared Spectrometer And Array Camera

ISO: Infrared Space Observatory

Keyword: Variable of a specified data type within the MIDAS environment.

LAICA: Large Area Imager for the Calar Alto

LM: Limiting Magnitude. Apparent magnitude of objects with a signal-to-noise ratio of 5.

M67: Open star cluster in the constellation Cancer at $\alpha = 8^h51^m$ and $\delta = 11.°82$.

M51: Spiral galaxy in the constellation Canes Venatici at $\alpha = 12^h17^m$ and $\delta = 47.°20$.

Median: Central value in an ordered sequence of numbers.

MIDAS: Munich Image Data Analysis System. Astronomical software package developed and maintained by the European Southern Observatory.

MPIA: Max-Planck-Institute for Astronomy

Multiplexer: Device that combines many signals into a small number of signals.

NGST: Next Generation Space Telescope. Now named the James Webb Space Telescope (JWST).

NIR: Near-infrared. In this thesis, usually used for the spectral region 1–2.5 μm, unless otherwise noted.

Pipeline: Automated data reduction software requiring only minimal user interaction.

Pixel Coordinates: Coordinate system based on the pixel row and column numbers on the detector.

Pointing: One principal telescope position. The sum of all images with a specific target in the field of view.

PSF: Point-Spread Function. Intensity distribution of a point-like light source in an astronomical image.

QE: Quantum Efficiency.

QSO: Quasi-Stellar Object

Seeing: "Blurring" of point-like astronomical objects caused by atmospheric turbulence. Without adaptive optics, the seeing limits the highest possible resolution in ground based observations. Typical seeing values for the Calar Alto observatory are somewhat better than 1 arcsec. The median seeing in the years 2001 and 2002 was 0.82 arcsec[1].

SNR: Signal-to-Noise-Ratio.

UKIRT: United Kingdom Infrared Telescope.

UT: Universal time.

Vignetting: Obscuration of parts of the primary mirror as seen by a detector pixel.

VISTA: Visible and Infrared Survey Telescope for Astronomy in Chile

VLT: Very Large Telescope in Chile

World Coordinates: Coordinate system that is based on absolute positions on the celestial sphere.

---

[1]See `http://www.caha.es/CAHA/MISC/seeing.html` for further details.

Bibliography

Bailer-Jones, C., Bizenberger, P., and Storz, C.: 2000, in M. Iye and A. F. Moorwood (eds.), *Optical and IR Telescope Instrumentation and Detectors*, Vol. 4008, SPIE - The International Society for Optical Engineering, Bellingham, Washington (USA)

Baumeister, H. *et al.*: 2003, in M. Iye and A. F. Moorwood (eds.), *Instrument Design and Performance for Optical/Infrared Ground-based Telescopes*, Vol. 4841, SPIE - The International Society for Optical Engineering, Bellingham, Washington (USA)

Beckwith, S. V. W.: 1994, in T. P. Ray and S. V. W. Beckwith (eds.), *Lectures Held at the Predoctoral Astrophysics School V Organized by the European Astrophysics Doctoral Network (EADN) in Berlin, Germany, 21 September - 2 October 1992*, Vol. 431, Springer-Verlag, Heidelberg

Bodenheimer, P. and Lin, D. N. C.: 2002, *Annual Review of Earth and Planetary Sciences* **30**, 113

Cox, A. N. (ed.): 2000, *Allen's Astrophysical Quantities*, New York: AIP Press; Springer

Fruchter, A. S. and Hook, R. N.: 2002, *Publ. Astron. Soc. Pac.* **114**, 144

Glass, I. S.: 1999, *Handbook of Infrared Astronomy*, Cambridge, Cambridge University Press

Haas, A.: 2002, *HAWAII-2: 2048x2048 Pixel Focal Plane Array*, Rockwell Scientific

Harris, W. E.: 1990, *Publ. Astron. Soc. Pac.* **102**, 949

Hodapp, K. W.: 2000, in M. Iye and A. F. Moorwood (eds.), *Proc. SPIE Vol. 4008*, pp 1228–1239

Joyce, R. R.: 1992, in *ASP Conf. Ser. 23: Astronomical CCD Observing and Reduction Techniques*, pp 258–283

Léna, P., Lebrun, F., and Mignard, F. (eds.): 1998, *Observational Astrophysics*, Berlin: Springer

Lindner, K.: 1989, *Astronomie*, Leipzig : Bibliographisches Institut

McLean, I. S. (ed.): 1997, *Electronic imaging in astronomy. Detectors and instrumentation*, Chichester, UK : Wiley

Meisenheimer, K. and Wolf, C.: 2002, *Sterne und Weltraum* **41**, 22

Murdin, P. . (ed.): 2001, *Encyclopedia of astronomy and astrophysics*, London, UK : Nature Publishing Group

Mutchler, M. and Fruchter, A.: 1997, *Bull. Am. Astron. Soc.* **29**, 1271

Press, W. H., Teukolsky, S. A., Vetterling, W. T., and Flannery, B. P.: 1992, *Numerical recipes in C. The art of scientific computing*, Cambridge: University Press, 2 edition

Rogalski, A. (ed.): 1995, *Infrared photon detectors*, Bellingham, WA : SPIE Optical Engineering Press

Röser, H.-J., Hippelein, H., and Wolf, C.: 2003, in J. S. Mulchaey, A. Dressler, and A. Oemler (eds.), *Clusters of Galaxies: Probes of Cosmological Structure and Galaxy Evolution*, Vol. 3 of *Carnegie Observatories Astrophysics Series*, Carnegie Observatories, Cambridge: Cambridge Univ. Press

Rousselot, P., Lidman, C., Cuby, J.-G., Moreels, G., and Monnet, G.: 2000, *Astron. Astrophys.* **354**, 1134

Stöcker, H.: 1998, *Taschenbuch der Physik*, Frankfurt am Main: Verlag Harri Deutsch

Unsöld, A., Baschek, B., and Brewer, W. D.: 1991, *The New Cosmos*, Springer-Verlag, Heidelberg

Vogel, H. and Gerthsen, C.: 1997, *Gerthsen Physik*, Springer-Verlag, Heidelberg

Wolf, C., Meisenheimer, K., Rix, H.-W., Borch, A., Dye, S., and Kleinheinrich, M.: 2003, *Astron. Astrophys.* **401**, 73

Zapatero Osorio, M. R., Béjar, V. J. S., Martín, E. L., Rebolo, R., Barrado y Navascués, D., Bailer-Jones, C. A. L., and Mundt, R.: 2000, *Science* **290**, 103

Acknowledgements

At this point, I would like to thank all the people who contributed to the work of this thesis and to the great atmosphere of the past year.

I would like to express my special gratitude to Dr. **Hermann-Josef Röser** for being a superb supervisor throughout the last year. He was always on the spot when I needed advice or had burning questions and guided me gently to a solution when my own ideas were failing.

I am indebted to the directors Prof. **Thomas Henning** and Prof. **Hans-Walter Rix** for given my the opportunity to work at the MPIA and supporting my trips to the Calar Alto Observatory.

I thank Prof. **Josef Fried** for providing his second opinion.

I would like to thank the whole OMEGA2000 team for the very pleasant working environment in Heidelberg and Spain. Special thanks go to:
Peter Bizenberger for his assistance in understanding NIR instrumentation.
Zoltan Kovacs for teaching my the secrets of C and being a good travel partner.
Clemens Storz for improving my relationship to computers.
Ulrich Mall, **Harald Baumeister**, and **Matthias Alter** for the good time on (and off) the mountain.

I am grateful to my roommates **Andreas Koch** and **Daniel Harbeck** for the fun and their advice.

Final thanks go to **Henry Lee**, **Daniel Zucker**, **David R. Anderson**, and **Sigfried Falter** for their language expertise and helpful remarks.

Erklärung:

Ich versichere, daß ich diese Arbeit selbständig verfaßt und keine anderen als die angegebenen Quellen und Hilfsmittel benutzt habe.

Heidelberg, den 10.05.2003 ....